1

Introduction and Overview

1.1 Introduction

In recent years, direct wide bandgap semiconductor materials have been extensively studied by many researchers, due to their excellent thermal, optical and electrical properties. They have found applications in the manufacture of blue – UV light emitting diodes (LEDs), laser diodes, solar blind UV detectors, solar cells, gas sensors, high electron mobility transistors (HEMTs) and heterojunction bipolar transistors (HJTs) [1,2,3]. To date, III – N compound semiconductor materials, in particular GaN, have been the most successful in the fabrication of blue – UV light emitting devices. GaN is hexagonal (wurtzite) in structure, possessing a band gap of ~ 3.43 eV and an excitonic binding energy of 23 meV [4].

Similar to III – V materials, II – VI materials, especially ZnO, have been subjected to tremendous research recently as potential materials to replace GaN. ZnO is also hexagonal (wurtzite) in structure, with a band gap of ~ 3.3 eV, and an excitonic binding energy of 60 meV [5]. It is usually deposited naturally as n-type semiconductor material.

This thesis focuses on the evaluation of a material called Copper I Chloride (CuCl) for the fabrication of blue – UV light emitting devices. CuCl belongs to the I – VII compound semiconductor material group with a band gap of ~ 3.4 eV [6]. It exhibits a zincblende structure (γ–phase) at low temperatures, up to ~ 680 K, where it transforms to the wurtzite structure (β–phase). Its excitonic binding energies are of the order of 190 meV [7].

1.2   Motivation of this Research

Since the commercialisation of GaN-based LEDs [8] and laser diodes [9] over ten years ago, Gallium Nitride has dominated the blue – UV optoelectronics industry. In spite of the interesting thermal, optical and electrical performance of this material, devices produced from GaN suffer from numerous threading dislocations, due to the lack of an appropriate substrate. It is usually deposited on sapphire (α–Al_2O_3), an insulator which has a lattice mismatch as high as 16% [10] to GaN. Figure 1 gives a schematic illustration of the lattice mismatch of a GaN(0001) film onto an Al_2O_3(0001) substrate. The introduction of epitaxial lateral overgrowth [ELOG] [11] and pendeoepitaxy techniques [12] for the deposition of GaN thin films has partially alleviated the problems of threading dislocations. As an alternative, the deposition of GaN on hexagonal silicon carbide (4H – SiC and 6H - SiC), with a lattice mismatch of ~ 3.4% [13] has paved the way for the fabrication of GaN/SiC films with lower threading dislocation densities. However, these techniques are not straightforward especially in the latter case where Ga has poor wetting on the SiC surface [14]. In addition, the high cost of growing good quality SiC substrates as well as the wide availability, the ease of handling and the easier pre-growth cleaning of Al_2O_3 has

allowed sapphire gain popularity as the substrate for depositing GaN films. The direct integration of GaN based optoelectronics with Si microeleclectronics has been very difficult due to a lattice mismatch of ~ 17%, thermal expansion coefficient incompatibility of ~ 56% and poor nucleation of GaN on Si [15].
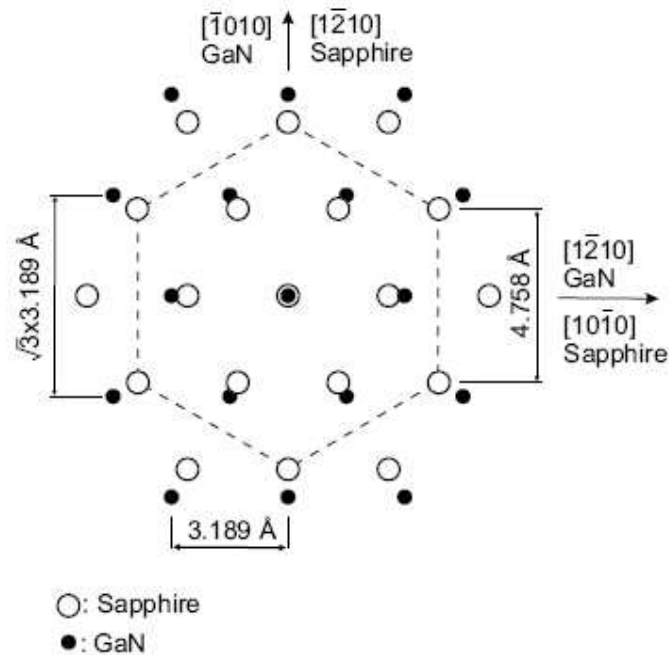
Figure 1.1: *Schematic illustration of the lattice mismatch for GaN(0001) grown onto an Al$_2$O$_3$(0001) surface [46].*

ZnO is another promising potential material for the fabrication of blue – UV light emitting devices, which has some advantages over GaN. These include an excitonic binding energy of 60 meV, and the availability of high quality bulk single crystals. However ZnO is usually deposited naturally as n-type semiconductor material due to non stoichiometry caused by zinc interstitials, oxygen vacancies or the incorporation of hydrogen in the crystal lattice [16,17,18]. The intrinsic defect levels that results in the formation of the n-type material are situated approximately 0.05 eV below the

conduction band. Owing to self-compensation of charges, it is very difficult to prepare high quality p-type ZnO material reproducibly. In fact the majority of the p-type ZnO films are usually characterized by relatively low hole concentrations, low hole mobility and instability [19,20,21,22,23], and the resulting p-type semiconductor may even appear to be n-type under the influence of ultraviolet photoelectron illumination [24]. As in the case for GaN, ZnO thin films face huge lattice mismatch problems with non-parental substrates and the difficulty of direct integration with the well-stabilized Si microelectronics based systems.

With a view to resolving these problems, we have investigated a new hybrid platform based on Copper I Chloride (cuprous chloride, CuCl) on Si. The large excitonic binding energy of the order of 190 meV, which is much superior to those of III – Nitride or ZnO compound semiconductor materials, guarantees the observation of excitonic recombination even up to room temperatures and beyond [25]. A lattice mismatch of < 0.4% when deposited on Si substrates ($a_{CuCl} = 0.541$ nm and $a_{Si} = 0.543$ nm) [26] indicates the possibility of fabricating blue – UV optoelectronic light emitting devices on Si with very low threading dislocation densities. In a similar fashion to ZnO but as opposed to GaN, high quality bulk single crystal CuCl can easily be grown. CuCl has been previously identified and recognised as a potential candidate material for the manufacture of electrooptic modulators and optical filters [27], as an electrolyte for solid-sate batteries [28], as a superconductor [29], as a photo catalyst [30], in photographic processing [31] and most recently as a sensor to detect CO in hydrogen environments [32]. In this study thin films of CuCl have been deposited and evaluated for their microstructural, electronic and optoelectronic properties and we have analysed the possibility of using a CuCl/Si hybrid platform for

next generation optoelectronic devices. As a wide band gap material emitting within the blue – UV region, CuCl will find applications across numerous industry fields, most notably in

Properties	CuCl	ZnO	GaN
ε_r	$10^{[33]}$	$8.65^{[18]}$	$8.9^{[35]}$
n at IR	$2.0^{[34]}$	$2.0^{[18]}$	$2.3^{[35]}$
E_x (meV)	$190^{[7]}$	$60^{[18]}$	$23^{[4]}$
E_g (eV)	$3.4^{[6]}$	$3.30^{[3]}$	$3.43^{[3]}$
Lattice Constant (nm)	$a = 0.541^{[26]}$	$a = 3.25^{[18]}$	$a = 0.3189^{[35]}$
		$c = 5.12^{[18]}$	$c = 0.5186^{[35]}$
Mismatch to Si (%)	<0.4	15	17
Structure	Zincblende	Hexagonal	Hexagonal

Table 1.1: *Some properties of CuCl, ZnO and GaN, where ε_r, n, E_x, and E_g are the static dielectric constant, refractive index in the infrared region, excitonic binding energy and optical band gap of the semiconductor material, respectively.*

the manufacture of the next generation DVD player-recorders and high-density optical data storage. A change from the currently available red or infrared (680 – 780 nm) laser diodes to CuCl based lasers emitting around ~ 387 nm, will significantly increase the optical storage density by up to six times the present capacity. Other possible applications include laser printing, projection displays, spectro–fluorometery,

photo-catalytic reactions, counterfeit detection, chemical detection, traffic signals and in medicine (e.g. the use of UV radiation in treating cancer and cerebral apoplexy).

Table 1.1 compares some important properties of CuCl with ZnO and GaN. It is interesting to see that values of the static dielectric constant ε_r, refractive index n, and optical band gap E_g of all the three materials are similar. However the excitonic binding energy E_x and lattice mismatch to Si of CuCl greatly surpass those of both ZnO and GaN. These two prime properties suggest that a near lattice matched exciton based light emitting devices could be fabricated a from CuCl/Si hybrid platform.

1.3   Report Organisation

This report describes the experimental work on the growth and characterisation of CuCl for possible optoelectronic applications. Apart from this laboratory, the research on copper chloride and related cuprous halides over the past decade or so has focused on three main sections:

- Spectroscopic and theoretical studies of band structures and excitonic-based luminescence in CuCl, and related copper halide mixed crystals [36,37,38].

- Fundamental photoluminescence and spectroscopic studies of CuCl quantum dots embedded in NaCl crystals [39,40] and glass matrices [41,42].

- Surface studies of the growth mechanisms involved in the heteroepitaxy of CuCl single crystals on a number of substrates such as MgO (001) and CaF$_2$ (111) [43] and reconstructed (0001) haematite (α- Fe$_2$O$_3$) [44]. Nishida and co workers [45] even extended the studies of the deposition CuCl films on matured semiconductor materials. They examined the surface growth

mechanisms in the heteroepitaxy of single crystalline films of CuCl on both Si and GaAs substrates by molecular beam epitaxy. However, this study focussed on the fundamental physics of the island growth process and the nature of the interfacial bonding.

We have proceeded from previous work from both this laboratory and elsewhere and attempted to analyse the possibility of using a CuCl/Si hybrid platform for optoelectronic applications. Most of the chapters begin with a brief theoretical and literature review of the subject concerned.

Chapter 2 provides the reader with specific information about materials used in this thesis, deposition of films, substrate preparation, experimental methods and the set-up used throughout.

Chapter 3 begins with a brief review of x-ray diffraction (XRD) and atomic force microscopy (AFM) and its applications to semiconductor materials. This is followed by detailed results of the structural and morphological properties of CuCl/Glass, CuCl/ITO, CuCl/Si and oxygen plasma immersed CuCl/Si films.

Chapter 4 provides the results of photoluminescence and optical absorption experiments on CuCl/Glass, CuCl/ITO and CuCl/Si oxygen plasma immersed CuCl/Si films. The literature review of the theory of luminescence and absorption processes in semiconductor materials are discussed as well.

Chapter 5 begins with a brief theoretical review of ionic and electronic conduction mechanisms in solids. This is followed by detailed electrical characterisation results of the as deposited CuCl and oxygen plasma immersed CuCl films confined between both reversible (Cu) and irreversible (Au) electrodes under the influence of steady

state DC (I–V) and small signal AC measurements using electro-impedance spectroscopy are also discussed.

Chapter 6 provides the results of encapsulation experiments on CuCl films using SiO_2 deposited by plasma-enhanced chemical vapour deposition (PECVD), organic polysilsesquioxane-based spin on glass material (PSSQ) and cyclo olefin copolymer (COC) thermoplastic-based material.

Finally, **chapter 7** summarises the subject matter of the thesis and suggests future research directions.

References

[1]   M.A. Khan, Q. Chen, J.W. Wang, M.S. Shur, B.T. Dermott and J.A. Higgins, *IEEE Electron Device Letters* **17** (1996) 325

[2]   S.T. Tan, B.J. Chen, X.W. Sun, X. Hu, X.H. Zhang and S.J. Chua, *Journal of Crystal Growth* **281** (2005) 571

[3]   H. Xing, L. McCarthy, S. Keller, S.P. DenBaars and U.K. Mishra, High current gain GaN bipolar junction transistors with regrown emitters, *Proceeding of IEEE Twenty-Seventh International Symposium on Compound Semiconductors* (2000) 365

[4]   I. Vurgaftman, J.R. Meyer and L. R. Ram-Mohan, *Journal of Applied Physics* **89** (2001) 5815

[5]   A. Tiwaii, C. Jin, A. Kuit, D. Kumar, J.F. Muth and J. Narayan, *Solid State Communications* **121** (2002) 371

[6]   K. Saito, M. Hasuo, T. Hatano and N. Nagasawa, *Solid State Communications* **94** (1995) 33

[7]   M. Ueta, H. Kanzaki, K. Kobayashi, Y. Toyosawa and E. Hanamura, *Excitonic Processes in Solids,* Berlin: Springer (1986)

[8]   S. Nakamura, M. Senoh, N. Iwasa, S. Nagahama, T. Yamada and T. Mukai, *Japanese Journal of Applied Physics* Part2 **34** (1995) 1332

[9]   S. Nakamura, M. Senoh, N. Iwasa, S. Nagahama, T. Yamada and T. Mutsushita, H. Kiyoku and Y. Sugimoto, *Japanese Journal of Applied Physics* Part2 (1996) **35** L74

[10]   J. Kyeong Jeong *et al.*, *Journal of Crystal Growth* **276** (2005) 407

[11]   S. Nakamura *et al.*, *Applied Physics Letters* **72** (1998) 211

[12]   R.F. Davis, T. Gehrke, K. J. Linthicum, T.S. Zheleva, E.A. Preble, P. Rajagopal, C. A. Zorman and M. Mehregany, *Journal of Crystal Growth* (2001) **225** 134

[13]   J.T. Torvik, C. Qiu, M. Leksono, and J.I. Pankove, *Applied Physics Letters* **72** (1998) 945

[14]   D.D. Koleske, R.L. Henry, M.E. Twigg, J.C. Culbertson, S.C. Binari, A.E. Wickenden and M. Fatemi, *Applied Physics Letters* **80** (2002) 4372

[15]   W. Uen, Z. Li, S. Lan and S. Liao, *Journal of Crystal Growth* **280** (2005) 335

[16]   D.C. Look, J.W. Hemsky and J.R. Sizelove, *Physical Review Letters* **82** (1999) 2552

[17]   Y. Jung, O. Kononenko and W. Choi, *Solid State Communications* **137** (2006) 474

[18]   S.J. Pearton, D.P. Norton, K. Ip, Y.W. Heo and T. Steiner, *Progress in Materials Science* **50** (2005) 293

[19]   K. Minegishi, Y. Koiwai, Y. Kikuchi, K. Yano, M. Kasuga and A. Shimizu, *Japanese Journal of Applied Physics* **36** (1997) L1453

[20]   X. Li, Y. Yan, T.A. Gessert, C. Dehart, C.L. Perkins, D. Young and T.J. Coutts, *Electrochemical and Solid-State letters* **6**:4 (2003) C56

[21]   X.L. Guo, H. Tabata and T. Kawai, *Journal of Crystal Growth* **223** (2001) 135

[22]   A.B.M.A. Ashrafi, I. Suemune, H. Kumano and S. Tanaka, *Japanese Journal of Applied Physics* **41** (2002) L1281

[23]   T.M. Barnes, K. Olson and C.A. Wolden, *Applied Physics Letters* **86** (2005) 112112

[24] C. L. Perkins, S-H Lee, X. Li, S.E. Asher and T. J. Coutts, *Journal of Applied Physic* **97** (2005) 034907

[25] K. Reimann and St. Rubenacke, *Journal of Applied Physics,* **76** (1994) 4897

[26] H.G. Grahn, *Introduction to Semiconductor Physics,* World Scientifics: Singapore (1999)

[27] F. Sterzer, D. Blattner and S. Miniter, *Journal of the Optical Society of America* **54** (1964) 62

[28] T. Matsui and J. B. Wagner Jr, *Solid Electrolytes,* Academic Press: N. York (1978)

[29] J. Bardeen, *Journal of Less Common Metals* **62** (1978) 447

[30] K. Tennakone, S. Punchihewa and R. Tanrigoda, *Solar Energy Materials* **18** (1989) 217

[31] G. Reboul, *Comptes Rendus 153* (1911) 1215

[32] P.K. Dutta, R.R. Rao, S.L. Swartz and C. T. Holt, *Sensors & Actuators B* **84** (2002) 189

[33] N.F. Mott and R.W. Gurney, *Electronic Processes in Ionic Crystals,* Oxford: Clarendon Press (1948)

[34] C. Schwab and A. Goltzene, *Progress in Crystal Growth Characterisation* **5** (1982) 233

[35] M.E. Levinshtein, S.L. Rumyantsev, and M.S. Shur, *Properties of Advanced Semiconductor Materials: GaN, AlN, InN, BN, SiC, and SiGe,* John Wiley and Sons New York (2001)

[36] M. Nakayama, H Ichida and H. Nishimura, *Journal of Physics: Condense Matter* **11** (1999) 7653

[37] B. Wyncke and F. Bréhat, *Journal of Physics: Condense Matter* **12** (2000) 3461

[38]   H. Heireche, B. Bouhafs, H. Aourag, M. Ferhat and M. Certier, *Journal of Physics and Chemistry of Solids* **59** (1998) 997

[39]   Y. Masumoto and S. Ogasawara, *Journal of Luminescence* **87-89** (2000) 360

[40]   M. Ikezawa and Y. Masumoto, *Journal of Luminescence* **87-89** (2000) 482

[41]   H. Kurisu, K. Nagoya, N. Nakayama, S. Yamamoto and M. Matsuura, *Journal of Luminescence* **87-89** (2000) 390

[42]   J. Sasai, K. Tanaka and K. Hirao, *Scripta Materialia* **44** (2000) 1225

[43]   A. Yanase and Y. Segewa, *Surface Science* **357-358** (1996) 885

[44]   Q. Guo, L. Gui and N. Wu, *Applied Surface Science* **99** (1996) 229

[45]   N. Nishida, K. Saiki and A. Koma, *Surface Science* **324** (1995) 149

[46]   S. Nakamura and G. Fasol, *The Blue Laser Diode: GaN based light emitters and lasers,* Springer-Verlag (1997)

2

Materials Preparation and Experimental Methods

2.1 Introduction

During the course of the evaluation of CuCl thin films as an optoelectronic material, a number of other materials were used in conjunction with CuCl. This chapter introduces briefly the laboratory procedures and experimental techniques used in this research work. This begins with substrate preparation, followed by materials, material deposition methods and the experimental techniques employed.

2.2 Substrate Preparation

The substrates used for in the research work were square-cut soda lime glass (VWR International), indium tin oxide coated glass slides (Sigma Aldrich $R_S = 20\Omega/$), Silicon substrates (University Wafer) and metal-coated soda lime glass slides. Prior to film deposition, the glass slides were placed in a beaker-containing Decon neutral (Decon Laboratory Ltd), a powerful degreasing detergent and subjected to an ultrasonic bath for about 10 minutes. The slides were then removed and physically washed with Decon neutral and cotton buds to further remove dirt and contaminants. Immediately after this, the slides were sequentially rinsed with cold,

hot and ultrapure deionised water (Millipore Q system). The slides were then placed in a beaker containing ultrapure water and subjected to an ultrasonic bath for about 20 minutes. Finally the slides were removed from the beaker and placed in a drying compartment where a stream of pure warm air or nitrogen gas was used to dry them. The indium tin oxide (ITO) coated glass slides were cleaned in a similar way and in addition to this, the slides were subjected to an ultrasonic bath in acetone and isopropanol/methanol respectively for about 5 minutes each to keep the surface of ITO hydrophobic. In addition to the conventional degreasing routine for ITO slides, the native oxide on the Si substrates was removed using hydrofluoric acid solution.

Aluminium, copper and gold were thermally evaporated on plain clean glass slides, thin films of CuCl and the dielectric materials used as encapsulants. Aluminium wire (Goodfellow, 99.95% purity) was evaporated using a Balzers TSH170 turbo pump vacuum evaporation system at a base pressure of the order of 10^{-6} mbar and it was used for the fabrication of metal–insulator–metal structures in characterising the dielectric constant of the encapsulants. Both gold and copper were deposited on CuCl films for the evaluation of the electrical properties. Gold wire (Alfa Aesar, 99.9% purity) and copper wire (Alfa Aesar, 99.999% purity) were deposited using an Edwards E306A thermal resistance evaporator with a base pressure of 1×10^{-6} mbar. A standard lithography masking technique was used for creating patterns on the films.

2.3 Materials

The main materials used in this research work are:

- SiO_2 deposited by plasma enhanced chemical vapour deposition (PECVD).

- Organic polysilsequioxane (PSSQ) spin-on glass-based dielectric.

- Cyclo olefin copolymer (COC)-based dielectric.

- Cuprous chloride (CuCl).

The PECVD SiO$_2$, PSSQ and COC were used as encapsulants for reducing the effects of oxidation of CuCl thin films.

2.4   SiO$_2$ Deposited by PECVD

2.4.1   General Description

The SiO$_2$ deposited by plasma enhanced chemical vapour deposition has similar properties to thermally grown SiO$_2$ but with the advantage of high growth rate, low deposition temperature, which favours low defect formation in the underlying substrate, low dopant diffusion and little degradation of metal layers [1,2]. The physical properties of the SiO$_2$ films deposited by this method may vary slightly depending on the precursor and the process parameters used. Some of the properties of a typical PECVD SiO$_2$ film includes band gap > 9 eV, refractive index $= 1.42$, density of 2.3 g/cm^3, dielectric constant ~ 3.5, dielectric strength > 8 MV/cm [1].

2.4.2   Deposition

Conventional chemical vapour deposition requires the formation of SiO$_2$ at elevated temperatures while PECVD permits the growth of SiO$_2$ at lower temperatures by the introduction of a plasma, which aids the efficient decomposition of the precursors at lower temperatures. Plasma enhanced chemical vapour deposited SiO$_2$ films are traditionally grown using either silane or tetraathoxysilane (TEOS) as a source of Si and nitrous oxide or oxygen as the oxidising agent. However the handling of silane is

very difficult as it is pyrophoric, flammable and toxic, therefore many researchers [3] use TEOS as the source of Si, which is safe and easy to handle as it is in liquid form and chemically stable. Other precursors as sources for Si and oxidizing agents are also available. The deposition of the SiO_2 films produced from this method was carried out in a PECVD chamber and precursors are allowed into the chamber via dedicated channels.

In this study, PECVD SiO_2 deposition was carried out using a oxygen/hexamethyldysiloxane (O_2/HMDSO) mixture in a parallel plate RF reactor at a frequency of 13.56 MHz. The O_2/HMDSO ratio was 10:1, while the RF power that determines the degree of excitation and fragmentation was kept constant at 350 W. The operating pressure was 10 Pa and the deposition time was 8 minutes, which resulted to ~ 400 nm of SiO_2. Detailed description for the deposition process of the SiO_2 films are fully reported in chapter 6.

2.4.3 Applications

SiO_2 films deposited by the PECVD technique are notably used as dielectrics in the semiconductor industry. It has found applications in film passivation, inter-metal dielectric layers, in memory devices, gate oxides and in metal oxide semiconductor field effect transistor devices (MOSFET) [1,4].

2.5   Polysilsesquioxane (PSSQ)

2.5.1   General Description

Polysisesquioxanes (PSSQ) are part of a new family of hybrid inorganic-organic composites designed with the good physical properties of ceramics and excellent choice of functional group chemical reactivity associated with organic chemistry. They possess the general empirical formulas $RSO_{1.5}$, R being an organic functional group [1]. Each Si atom is bonded to one and a half (sesqui) oxygen atoms and to one hydrocarbon group (ane). They have excellent dielectric properties with high breakdown strength comparable to that of SiO_2 but with a lower dielectric constant.
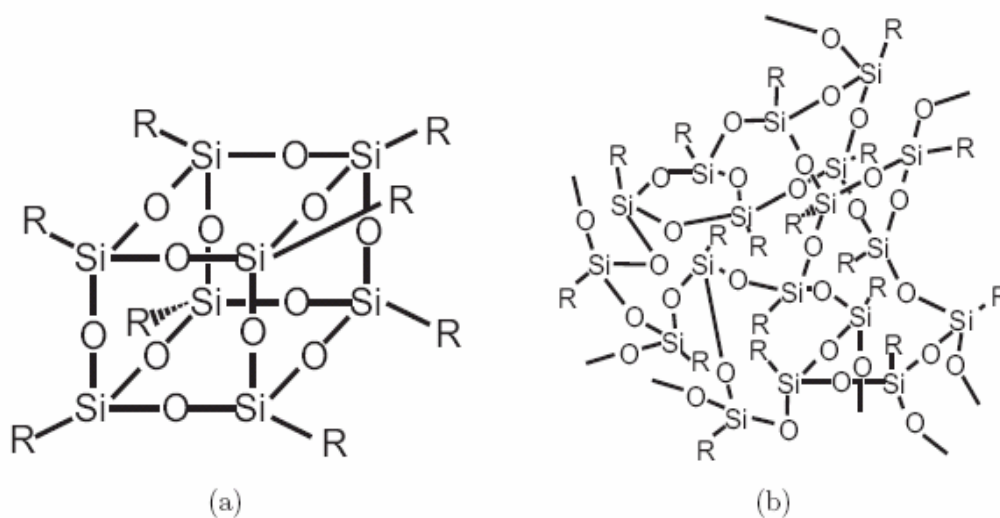
Figure 2.1: *Chemical structure of polysilsesquixane in (a) cage form and (b) network form [1].*

2.5.2   Chemical Preparation

Silsesquioxanes are generally prepared via the acid – catalysed hydrolytic condensation reactions of trifunctional organosilicon monomers such as alkyltrialkoxysilane, alkyltrihalosilane or trimethoxysilane [1]. The molecular structure of PSSQ consists of a mixed cage and network structures (see figure 2.1) before thermal curing, with part of the cage structure transforming into a network structure after curing [5]. The structural and dielectric properties of PSSQ film depends strongly on the conditions of thermal curing [6] and the change of structure with temperature differs among different polysilsequioxanes.

2.5.3   Deposition

PSSQ are commercially supplied usually in flaked form, which are soluble in a variety of common organic solvents including methanol, iso–propanol, ethanol, butanol, hexanol, and butanone but the quality of the films is highly dependent on the solvent and the substrates [7]. In this study, the PSSQ used was a commercially supplied PSSQ solution from Emulsitone Inc, USA. The PSSQ solutions were spun at 3000 rpm using a spin coater or isothermally dipped using a dip coater and cured under vacuum at 160°C for 1 hour cumulating to a thickness of ~ 300 nm. The encapsulated thin films of CuCl could only be cured at low temperatures, because, thin films of CuCl react with Si at a temperature greater than ~200°C [8].

2.5.4   Applications

Since the first synthesis of polysilsequioxanes in 1948 [9], they have found applications in numerous industries, such as in ceramics, low-k interlayer dielectric

layers, thermo-optical materials for photonic devices and most recently PSSQs have been successfully used as the dielectric layer in organic thin film transistors (OTFTs) [10] with good performance comparable to that of SiO_2.

2.6 Cyclo Olefin Copolymer (COC)

2.6.1   General Description

Cyclo olefin copolymer (COC) based dielectrics are new class of thermoplastic polymers. COCs are composed of small olefin monomers which are randomly or alternately attached to the polymer backbone, thus making the copolymer amorphous with low dielectric loss, low dielectric constant, high dielectric strength, low moisture absorption, good chemical resistance to polar solvents, low shrinkage, very large band gap, excellent transmittance in the visible and near-ultraviolet wavelengths and low birefringence [11]. It has a density of the order of ~1.03 g/cm^3, dielectric constant of the order of ~2.3 and refractive index of the order of ~ 1.53.

2.6.2   Chemical Preparation

There are several types of commercial cyclo olefin copolymers based on different monomers and polymerisation methods. COCs are produced by chain copolymerisation of cyclic monomers such as 8,9,10–trinorborn–2–ene (norbornene) or 1,2,3,4,4a,5,8,8a–octahydro–1,4:5,8-dimethanonaphthalene (tetracylododecene) with ethene, or by the ring-opening metathesis polymerisation of various cyclic monomers followed by hydrogenation [12]. A typical polymerisation scheme is illustrated in figure 2.2
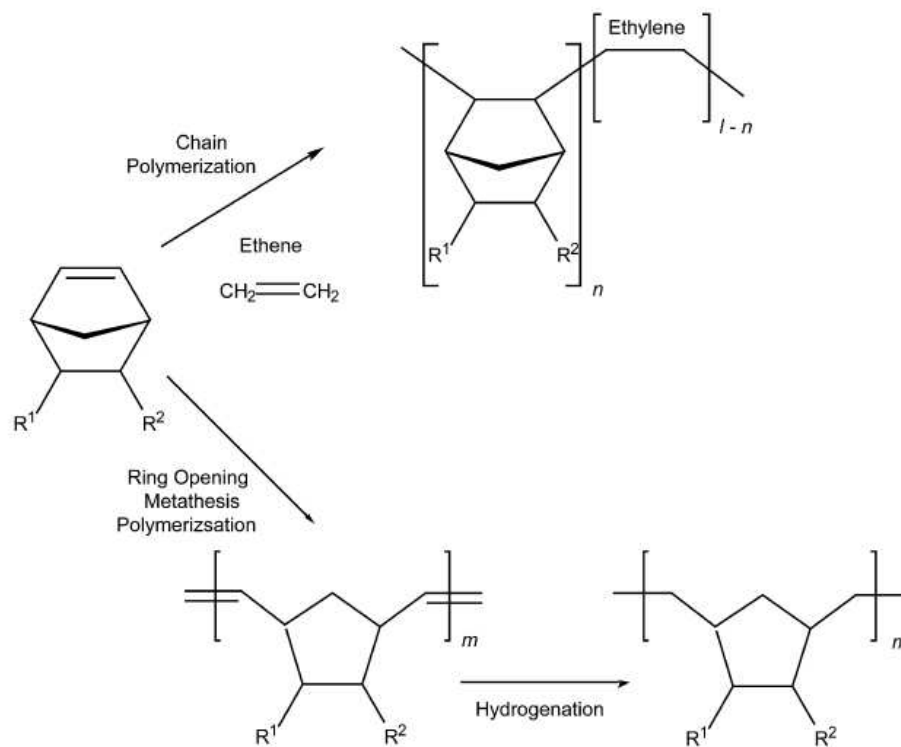
Figure 2.2: *Typical polymerisation scheme of cyclo olefin polymers [12].*

2.6.3   Deposition

Cyclo olefin copolymers are commercially supplied usually in flake form, which are soluble in very few organic solvents, including toluene and cyclohexane. Similar to PSSQ, the quality of the film is highly dependent on the solvent and the substrates. In this study, the COC used was a cyclo olefin copolymer based solution supplied by Brewer Sciences Inc. The COC solutions were spun at 5000 rpm using a spin coater or isothermally dipped using a dip coater and cured under vacuum at 175°C for 15 minutes.

2.6.4　　Applications

Since the first report of the synthesis of cyclo olefin copolymer in 1991 [13], it has found applications in various industries such as in optics, medical, electrical packaging, diagnostic containers and, due to its excellent dielectric properties, it will likely find applications as an efficient low-k dielectric material.

2.7　Copper (I) Chloride

2.7.1　　Physical Properties

Copper (I) chloride and related halides (CuCl, CuBr and CuI) are ionic I-VII compounds and crystallise naturally in the zincblende ($T_d, F\overline{4}3m$) structure [14]. Their ionicities on the Philips scale are 0.746, 0.735 and 0.692 for CuCl, CuBr and CuI respectively [15,16]. These values of the ionicities of cuprous halides especially that of CuCl approaches the critical value of 0.785 marking the boundary between compounds with six-fold coordination (rock salt) and four-fold coordination (zincblende, wurtzite). With increasing temperature, CuCl undergoes a solid-state phase transition from the zincblende structure (γ-phase) to the wurtzite (β-phase) at 680 K before melting at around ~ 695 K [17].

Figure 2.3 shows the zincblende structure of CuCl. This consists of two interpenetrating face-centred-cubic (f.c.c.) sublattices occupied by Cu^+ and Cl^- respectively. The unit cell is composed of four molecules, in which each Cu atom is surrounded by a regular tetrahedron built by four Cl atoms at a nearest neighbour

distance of $\dfrac{a\sqrt{3}}{4}$ [18,19], where a is the lattice constant. The second nearest

neighbours are twelve atoms of the same kind at a distance of $\dfrac{a\sqrt{3}}{4}$.

Copper chloride boils at ~ 1763 K, has a density of 4.140g/cm^3 and a lattice constant of 0.5416 nm for the zincblende structure [19]. It is almost insoluble in water but dissolves readily in concentrated hydrochloric acid. Copper (I) chloride is unstable in air due to the weak bonding that holds the molecules of monovalent cuprous halides. Thus it forms oxyhalides of Cu II upon exposure to air [19]. Table 2.1 summarises some important properties of cuprous chloride.
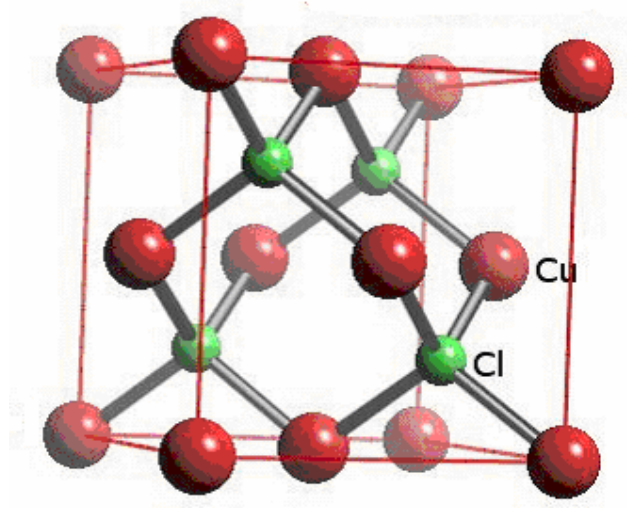
Figure 2.3: The zincblende structure of copper (I) chloride (CuCl) [20].

2.7.2   Optical and Band gap Properties

These are probably most investigated properties of cuprous halides due to their large excitonic binding energies (190 meV for CuCl and 108 for CuBr [21,22]). Copper (I) chloride is a wide band gap semiconductor material with a direct band gap of ~ 3.4 eV [23,29]. The electronic band structures of the cuprous halides have been studied by several authors from both a theoretical and experimental point of view.

Using theoretical techniques, Song [24] used a tight-binding scheme to calculate the band structure of CuCl. Calabrese and Fowler [25] used a mixed basis set (plane-tight binding) with Slater and valence-screening exchanges to calculate the band structure of CuCl. Overhof [26,29], used a relativistic Korringa-Kohn-Rostoker (KKR) method with Slater and Kohn-Sham exchange to calculate the band structure and densities of valence states (DOVS) for CuBr and Kleinman and Mednick [27] gave the first-consistent energy band calculation of CuCl with sufficient variational freedom to calculate the band structure and the effective masses accurately.

On the experimental side, Krolikowski examined the photoemission spectra for copper salts over a photon energy range of 6 – 11.8 eV. Kono *et al.* [28] studied the band structure of cuprous halides using x–ray photoemission measurements and Goldmann *et al*. [29] carried out comprehensive studies on the band structure and density of valence states (DOVS) of cuprous and silver halides (CuCl, CuBr, CuI and AgI) by using photoelectron spectroscopy over a wide range of excitation energies.

According to [27] and [29], the valence bands of cuprous halides originate from the combination of the parental copper metal ($d^{10}s^1$) and halogen (s^2p^5) outer electronic

configuration. On forming a compound (CuX; where X = Cl, Br or I), the loosely bound s electron of copper is transferred to the more electronegative halogen. This leaves the metal ion with a completely filled outer d shell and the halogen ion with a rare gas configuration. The energy band diagram of CuCl in the zincblende structure is depicted in figure 2.4

At low temperatures, copper (I) chloride exhibits a variety of fluorescent emission lines with energies near the band gap [30]. These emissions are attributed to the anihilation of free excitons and excitons bound to crystal imperfections. The top of the valence band of cuprous chloride is split into two bands by the spin-orbit interaction, yielding Z_{12} and Z_3 free excitons, which are ~ 60 meV apart from each other [31]. This valence band structure is in reverse order to that of most typical semiconductors

Other important optical properties of copper chloride include transparency between 0.4 μm and 20 μm, an electro-optic coefficient Γ_{14} of 6×10^{-10} cm/V and a refractive index of ~ 2 [32].
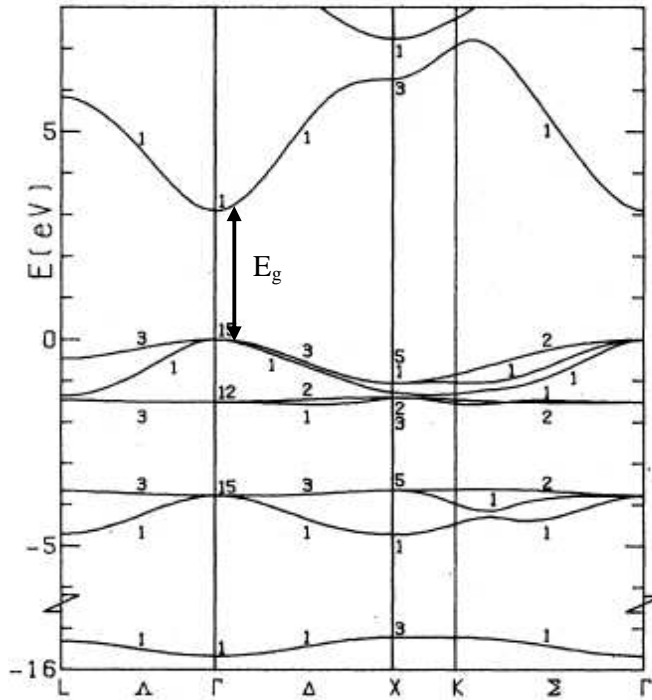
Figure 2.4: The energy band diagram of copper (I) chloride in zincblende structure [27].

2.7.3   Electrical Properties

The electrical properties of cuprous halides have also been studied by several authors [32 – 46] and have been found to greatly depend on small deviations from ideal stochiometry ratios. Electrical conductivity measurements of cuprous halides samples carefully freed of excess halogen revealed predominantly ionic conduction through copper ions [32,41 – 46]. Excess halogen corresponding to a deficit of copper causes hole conduction in addition to the ionic conduction. All three cuprous halides are mixed, ionic and electronic semiconductors at low temperatures [19]. Below room temperature, electronic conductivity is usually predominant; conversely, at high temperature, the ionic contribution accounts for most of the total conductivity value.

Within the high temperature range, all three compounds are superionic conductors, with conductivities in excess of 1 S/cm [19]. An electrical conductivity of the order of 10^{-8} S/cm was reported for bulk single crystal of CuCl samples at room temperature by Rivera *et al.* [32].

2.7.4 Chemical Preparation

The primary route by which most commercial copper (I) chloride powders are made today has been in known since as far back as 1950 [47]. This involves the passing of a mixture of hydrochloric acid solution and argon over 99.999% copper metal at 1223 K (950°C). The CuCl powder precipitated from the reaction will then be washed in organic solvents dried and stored in a sealed bottle under argon gas. The process reaction is governed by the chemical equation:

$$2Cu + 2HCl \rightarrow 2CuCl\downarrow + H_2\uparrow \qquad (2.1)$$
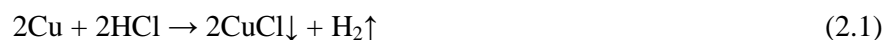
Other popular methods reported in the literature includes the carbonation of palladium in a solution containing cupric sulphate-chloride [48], thermal decomposition of organic copper compounds [49], reaction of copper metal with tetrachlorocabornate [50], exposure of copper single crystals to chlorine gas in an ultra high vacuum chamber [51], reaction of copper oxide with ammonium chloride at 673 K and ion implantation method combined with post heating at high temperatures [52]. Nearly all these techniques require complicated equipment, high reaction temperatures, utilize

28

toxic reactants and organic solvent or produce pollutive byproducts. However, very recently, Zhang and co-workers [53] demonstrated the hydrothermal reaction of copper (II) chloride ($CuCl_2$) and alpha-D-glucose ($C_6H_{12}O_6$), a mild renewable, inexpensive and non toxic reducing agent, in the presence of distilled water and at a temperature of 393 K to synthesise purified CuCl nanocrystals. They called the process *"A green hydrothermal route to nanocrystalline CuCl"* due to the combined use of safe and renewable reactants and a benign solvent medium involved in the synthesis. It was suggested that the formation of nanocrystalline CuCl powder from this method is by complexation-reduction-precipitation mechanism and summarised the equation for the process as:

$$2CuCl_2 + C_6H_{12}O_6 + H_2O \rightarrow 2CuCl\downarrow + C_6H_{12}O_7 + 2HCl \qquad (2.2)$$

2.7.5   Deposition Techniques

Cuprous chloride is usually deposited in either polycrystalline or single crystal form. Its is very difficult to grow unstrained and twin free single crystal CuCl from the melt due to the wurtzite – zincblende phase transition that takes place at 680 K [32]. The problem of the phase transition can be avoided by depositing at temperatures below the wurtzite – zincblende phase transition temperature. High quality single crystal CuCl has been successfully grown by vapour transport [54], flux growth [55,56,57], gel growth [58] and most recently by molecular beam epitaxy [59].

In this study thin films of polycrystalline copper (I) chloride were grown using a vacuum evaporation method, the starting material being commercially supplied copper (I) chloride powder by Alfa Aesar with a purity of 99.999%. A variety of

materials have been previously used as the substrates for the heteroepitaxy of CuCl films. This includes, MgO and CaF_2 [60], haematite [61], sapphire [62], GaAs [63] and Si [7,63,64] substrates. From a device point of view, silicon seems to be the most promising out of all these substrates, due to its near lattice match to

Lattice parameters	a = 5.1416 (Zincblende) a = 3.91 (Wurtzite) b = 6.42
Phase Temperature Range	< 680 K (Zincblende) 680 < T < 695 K (Wurtzite)
Melting Point	695 K
Density	4.140 g/cm^3
Boiling point	1763 K
Bandgap	3.4 eV
Z_{12} *Exciton*	3.27 eV
Z_3 *Exciton*	3.204 eV
M Free Biexciton	3.168 eV
I_1 *Bound Exciton*	3.181 eV
N_1 *Bound Exciton*	3. 149 eV
Refractive Index	~ 2 at infra-red wavelengths
Transparency	$0.4 \leq T_r \leq 20$ μm
Total Electrical Conductivity	~ 10^{-8}

Table 2.1: *Some important properties of cuprous chloride.*

copper (I) chloride ($<$ 4 %), its low cost, good thermal conductivity, availability of high crystalline quality and the possibility of integrating CuCl based optoelectronic devices with mature silicon microelectronics based devices.

Thin films of cuprous chloride of thickness between 100 – 500 nm were deposited on clean substrates (glass, ITO and Si) using an Edwards E306A thermal resistance evaporator with a base pressure of $\sim$ 1 x 10^{-6} mbar and evaporation pressure of $\sim$ 3 x 10^{-6} mbar. The cuprous chloride powder was evaporated from a small clean quartz crucible situated at about 13 cm from the substrate and at a growth rate of $\sim$ 0.5 nms^{-1} as indicated by the in built FTM6 thickness monitor in the evaporator chamber. It is necessary to deposit copper (I) chloride films at low pressure in order to avoid oxidation of CuCl powder and as well as ensuring that the evaporated atoms undergo a near collisionless transport from the source to the substrate. The mean free path of gas particle is given by [65]:

$$\lambda = \frac{5 \times 10^{-3}}{P_m} \quad \text{cm} \tag{2.3}$$
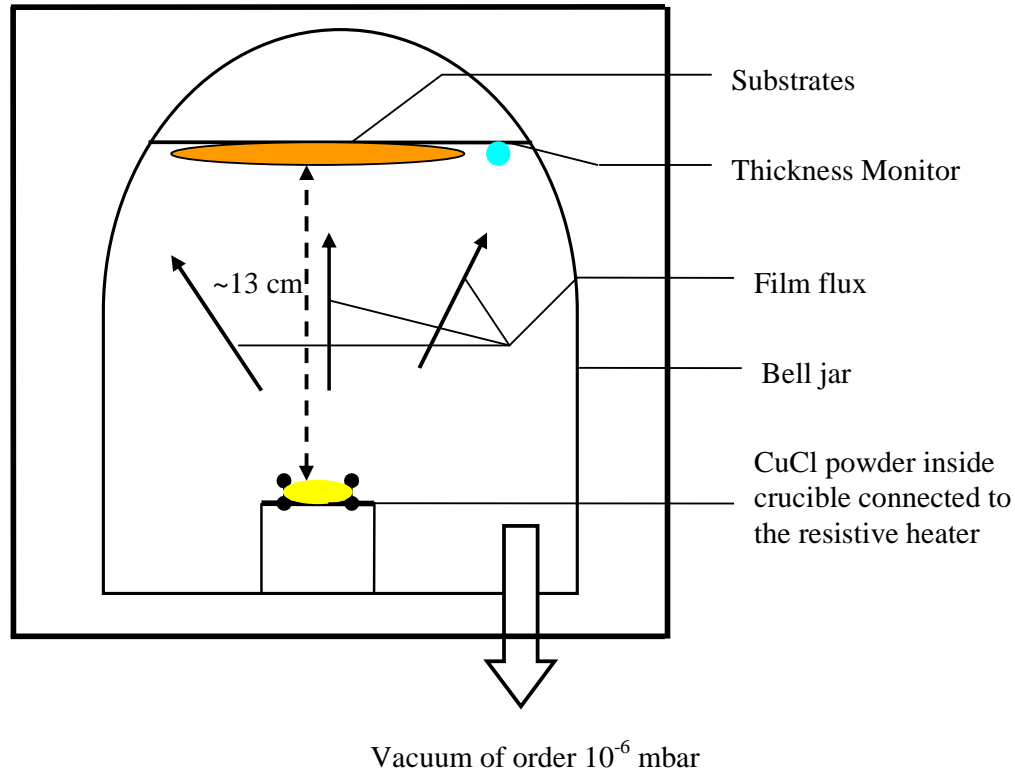
Figure 2.5: A schematic diagram illustrating the growth of cuprous chloride (CuCl) films using vacuum evaporation technique.

where P_m is the pressure in Torr. Thus at an evaporating pressure of ~ 3×10^{-6} mbar (2.25×10^{-6} Torr) corresponds to a mean free path of evaporated gas λ of about 2222.22 cm. Figure 2.5 shows a schematic diagram illustrating the growth of CuCl films using the vacuum evaporation method. Adjusting the current flowing through the crucible controls the rate of evaporation. The rate at which atoms pass into vacuum from a heated source is given by the well known Hertz-Knudsen rate equation [66]:

$$W = 3.5 \times 10^{22} \, \alpha P^* / (MT)^{-1/2} \quad \text{atoms/cm}^2\text{sec} \tag{2.4}$$

where P^* is the vapour pressure in Torr, T is the temperature in Kelvin and M is the molecular weight in grams. The parameter α is the evaporation coefficient. It is dependent on the cleanliness of the evaporation surface and can range from unity for clean surfaces to a value as low as 10^{-3} for dirty surfaces [67]. The emission of vapour from a clean source surface ($\alpha = 1$), and to the first order for other cases, follows a simple cosine rule [67]. Thus the evaporated flux from a small source, of area A and evaporation rate W, which is incident on an elemental substrate located at an angle φ from the perpendicular axis of the source as shown in Figure 2.6, yields a deposition flux per unit area on the substrate that is given by [65]:

$$W_d = \frac{WA}{\pi r^2} \cos \varphi \cos \theta \qquad (2.5)$$

where r is the distance from the source to the substrate. The $\cos \theta$ term accounts for the fact that the substrates may not be perpendicular to the line of the centre connecting the source and the substrates, thus leading to variation in thickness of films over large surface areas.

However, for a small source emitting from its surface, the cosine law implies that it will provide uniform deposition over the inside of a spherical surface if the source is placed on the circumference [68]. Under this condition:

$$\cos \varphi = \cos \theta \qquad (2.6)$$
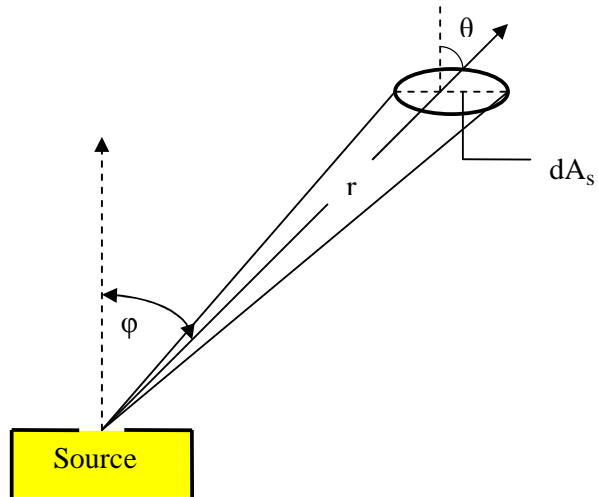
Figure 2.5: Emission flux passing from small area source to elementary substrate area [65].

and

$$r = 2R \cos \theta \qquad\qquad [2.7]$$

for all deposition points on the circumference of a sphere of radius R. In our own case the thickness was estimated from the measured crystal resonant frequency of the calibrated FTM6 thickness monitor. Immediately after deposition, the films were subjected to various characterisation techniques, plasma treated, stored in a light tight dynamic vacuum chamber or encapsulated.

2.7.6 Plasma Treatment of CuCl Films

Plasma was first identified by Sir William Crookes who called it radiant matter in 1879 [69], but in 1928 Irving Langmuir gave it present name [70], perhaps because it reminded him of a blood plasma [71]. Plasma may be defined as a partially ionized gas consisting of electrons, ions, free radicals, photons, and neutral particles. They are generated by supplying sufficient energy to a neutral gas causing the formation of charge carriers [72-74]. There are several ways of supplying energy for the generation of a plasma. According to [75], these include the use of thermal energy, adiabatic compression, high energetic beams and electric fields. The electric field method is the most commonly used method in generating and sustaining a low temperature plasma for technological and technical applications [75].

It is well known that any volume of neutral gas always contains a few electrons and ions that are formed, through the interaction of the gas with cosmic, radioactive radiation or other processes. When such a neutral gas is subjected to a sufficient electric field, the free carriers collide with the majority neutral molecules of the gas thereby causing electron impact excitation. This process occurs when the electrons in a neutral atom are excited to a higher level within the atom, due to electron collisions. However the excitation states are not stable and the electrons return to the ground state after a short while, leading to emission of photons. The latter process is known as relaxation. Also more electrons and ions are produced as a result of the free carriers with sufficient energy colliding with the neutral gas, this process being known as electron impact ionisation. The excitation energy V^* and ionisation energy V_i of a selection of atoms and molecules is shown in table 2.2 [76].

Gas	V^* (eV)	V_i (eV)	Ionisation process
H_2	7.0	15.37	$H_2 \rightarrow H_2^+ + e^-$
		18.0	$H_2 \rightarrow H^+ + H + e^-$
H		13.6	$H \rightarrow H^+$
N_2	6.3	15.57	$N_2 \rightarrow N_2^+ + e^-$
		24.5	$\rightarrow N^+ + N + e^-$
O_2	7.9	12.5	$O_2 \rightarrow O_2^+ + e^-$
		20	$\rightarrow O^+ + O + e^-$
Ar	11.7	15.7	$Ar \rightarrow Ar^+ + e^-$
He	21.2	24.5	$He \rightarrow He^+ + e^-$
CO	6.2	14.1	$CO \rightarrow CO^+ + e^-$
		22.0	$\rightarrow C^+ + O + e^-$
		24.0	$\rightarrow C + O^+ + e^-$
CO_2	3.0	14.0	$CO_2 \rightarrow CO_2^+ + e^-$
		19.6	$\rightarrow CO + O^+ + e^-$
		20.4	$\rightarrow CO^+ + O + e^-$
		28.3	$\rightarrow C^+ + O + O + e^-$

Table 2.2: *The excitation energy V^* and ionisation energy V_i of some atoms and molecules [76].*

Plasmas have been successfully applied to numerous sectors in the industry, notable areas including thin and thick film deposition (physical vapour deposition, sputtering and plasma deposition, enhanced chemical vapour deposition), etch (reactive ion etching and sputter etch), lithography (generation of light e.g. UV light sources), ion implantation (generation of ion sources), material treatments (modification of surface physics and surface chemistry, material cleaning, sterilisation, etc.), display, waste treatment and materials analysis.

In this study, the plasma treatment of CuCl films was carried out in an Oxford Instruments Plasma Lab Plus 80 reactive ion etcher (RIE). Figure 2.6 shows a schematic diagram of a typical RIE system. The main reason for the plasma treatment of CuCl films is to introduce oxygen as a dopant into the CuCl crystals in order to improve the electronic conductivity of cuprous chloride. Oxygen and argon were flowed in via dedicated channels at a flow rate of 80 sccm for oxygen and 20 sccm for argon, the RF power was 300 W, while the chamber pressure was held at 50 mTorr. The duration of the plasma treatment was for mainly 1, 2, and 3 minutes for the different samples. Argon was added to the gas in order to increase the depth of penetration of the oxygen. Immediately after plasma treatment, the films were subjected to various characterisation techniques, stored in a light tight dynamic vacuum chamber or encapsulated.
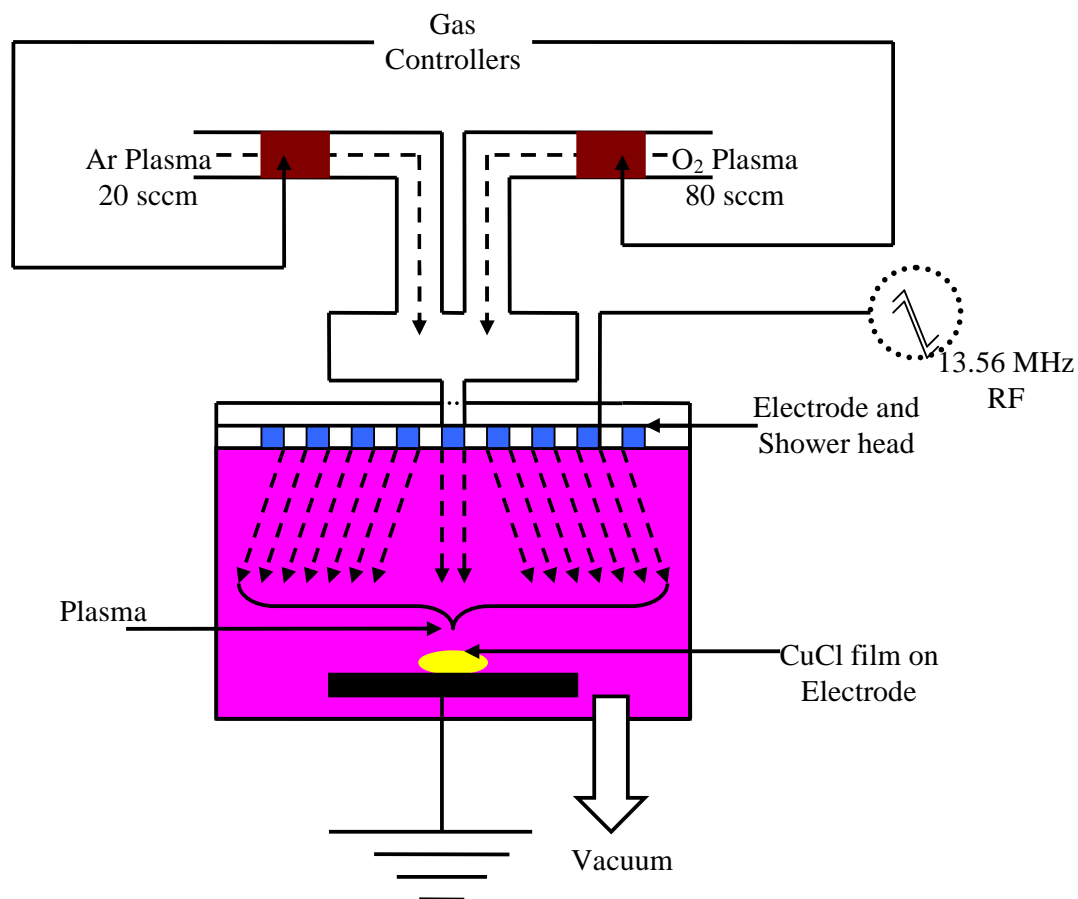
Figure 2.6: *A Schematic diagram of typical reactive ion etcher (RIE).*

2.7.7 Applications

Copper chloride and related halides have been studied for several decades due to their unusual properties. Owing to their electrical properties (fast ionic conductors at elevated temperatures) these materials have possible applications as electrolytic and solid state batteries [77]. Other possible applications noted in the literature include superconductivity [78], operation as a catalyst [79,80,81,82], an effective adsorbent for separating CO from gas mixtures [83] and as an air purifying agent [84], in optical nonlinear devices and optical memory devices [85,86], in vapour lasers [87,88] and

also in photography processing [89,90]. However, apart from this laboratory, there has never been any report of CuCl or a related halide as a potential material in the fabrication of a silicon compatible light-emitting device.

2.8   Characterization Techniques

Structure, Chemical Composition, and Morphology

Room temperature classical grazing angle x-ray diffraction was applied to check the crystallinity, structure, particle size and elastic strain of the films. Semi-quantitative chemical analysis and impurity detection was carried out at room temperature using Energy Dispersive X-ray analysis (EDX). The room temperature microstructure of the films was observed by optical microscopy and atomic force microscopy (AFM).

Optical

 Room temperature absorption and temperature dependent photoluminescence was used in investigating the optical properties of the films. Ultraviolet – visible (UV/vis) absorption measurements were used in conjunction with Fourier transform infrared spectroscopy measurements (FTIR) to monitor the degradation process.

Electrical

 Room temperature steady state DC and temperature dependent AC measurements were taken for different configurations: Cu/CuCl/Cu, Au/CuCl/Au, and ITO/encapsulant/Al. Secondary ion mass spectroscopy (SIMS) measurements were used in investigating the oxygen depth profile of the plasma treated CuCl films. The experimental set up for these will be fully explained in the relevant chapters.

References

[1]   S. Murarka, P. Eizenberg, M and A. Sinha, *Interlayer dielectrics for semiconductor technologies*, Academic Press (2003)

[2]   S.V. Nguyen, D. Doubuzinnsky, D. Dopp, R. Gleason, M. Gibson and S. Friedmann, *Thin Solid Films* **595** (1990) 193

[3]   A.M. Mahajan, L.S. Patil, J.P. Bange, D.K. Gautam, *Surface and Coating Technology* **183** (2004) 295

[4]   Y.B. Park and S.W. Rhee, *Surface and Coating Technology* **179** (2004) 229

[5]   W.C. Liu, C.C Yang, W.C. Chen, B.T. Dai and M.S. Tsai, *Journal of Non-Crystalline Solids* **311** (2002) 223

[6]   C.C. Yang, W.C. Chen, L.M. Chen, C.J. Wang, *Proc. Nat.l Sci. Counc. ROC (A),* **25** (2001) 339

[7]   Y. Abe, K. Kagayama, N. Takamura, T. Gunji, T. Yoshihara and N. Takahashi, *Journal of Non-Crystalline Solids,* **261** (2000) 39

[8]   L. O'Reilly, G. Natarajan, F.O. Lucas, P.J. McNally, D.C. Cameron, A. Reader, M. Martinez-Rosas, and A.L. Bradley, *Journal of Materials. Science: Electronic Materials* **16** (2005) 415

[9]   D.W. Scott, *Journal of American Chemical Society,* **68** (1946) 356

[10]   Z. Bao, V. Kuck, J.A. Rogers and M.A. Paczkowski, *Advanced Functional Materials* **12** (2002) 526

[11]   G. Khanarian, *Optical Engineering* **40** (2001) 1024

[12]   J.Y. Shin, J.Y. Park, C. Liu, J. He and S.C. Kim, *Pure Applied Chemistry,* **77** (2005) 801

[13] W. Kaminsky, A. Bark, and M. Arndt, *Macromolecular Symposia* 47 (1991) 83

[14] B. Wyncke and F. Bréhat, *Journal of Physics: Condensed Matter* **12** (2000) 3461

[15] J. C. Philips, *Physical Review Letters* **20** (1968) 550

[16] J. A. Van Vechten, *Physical Review* **187** (1969) 1007

[17] G. W. Herzog and H. Krischner, *7th International Symposium on the Reactivity of Solids,* Supplementary Preprints, Bristol, England, 17 – 21 July (1972)

[18] O. Edholm, P. I. Ohlsson, M. L. Smith and J. Paul, *Chemical Physics Letters* **291** (1998) 501

[19] C. Schwab and A. Goltzené, *Progress in Crystal Growth and Characterisation* **5** (1982), 223

[20] Web Elements Periodic Table, [online]. Available on www.webelements.com [accessed 17th of April 2007]

[21] M. Ueta, H. Kanzaki, K. Kobayashi, Y. Toyosawa and E. Hanamura, *Excitonic Processes in Solids* Berlin: Springer (1986)

[22] G. Hönerlage, R. Lévy, J Grun, C. Klingshirn and K. Bohnert, *Physics Report* **124** (1995) 161

[23] D. K. Shuh, R. S. Williams, Y. Segawa, Jun-ichi. Kusano, Y. Aoyagi and S. Namba, *Physical Review B* **44** (1991) 5827

[24] K. S. Song, *Journal of Physical Chemistry of Solids* **28** (1967) 2003

[25] E. Calabreese and W. B. Fowler, *Physica Status Solidi B* **56** (1973) 621

[26] H. Overhof, (Private communication)

[27] L. Kleinman and K. Mednick, *Physical Review B* **20** (1979) 2487

[28]   S. Kono, T. Ishii, T. Sagawa and T. Kobasi, *Physical Review Letters* **28** (1972) 1385

[29]   A. Goldmann, J. Tejeda, N. Shevchik and M. Cardona, *Physical Review B* **10** (1974) 4388

[30]   Y. Kaifu, Y. Kawate, S. Nakanishi, I. Niwa and K. Nakawa *Journal of the Physical Society of Japan* **22** (1967) 517

[31]   M. Nakayama, H. Ichida and H. Nishimura, *Journal of Physics: Condensed Matter* **11** (1999) 7653

[32]   J. Rivera, L. Murray and P. A. Hoss, *Journal of Crystal Growth* **1** (1967) 171

[33]   K. Bädecker, *Annalen der Physik* **22** (1907) 749

[34]   K. Bädecker, *Annalen der Physik Z.* **9** (1907) 431

[35]   G. Rudert, *Annalen der Physik* **31** (1910) 559

[36]   R. J. Maurer, *Journal of Chemical Physics* **13** (1945) 321

[37]   Okada, Kone and Uno, *Chemical Abstract* **44** (1950) 10421

[38]   B. H. Vine and R. J. Maurer, *Z. Physik. Chem.* **198** (1951) 147

[39]   E. Friederich and W. Meyer, *Z. Electrochem.* **32** (1926) 566

[40]   Tunbandt, Rindtorff and Jost, *Z. anorg. U. allegm. Chem.* **165** (1927) 195

[41]   J.B. Wagner and C. Wagner, *Journal of Chemical Physics.* **26** (1957)1597

[42]   A.V. Joshi and J.B. Wagner Jr, *Journal of the Electrochemical Society* **122** (1975) 1071

[43]   M. Bendahan, C. Jacolin, P. Lauque, J –L Seguin, and P. Knauth, *Journal of Physical Chemistry* B **105** (2001) 8327

[44]   A. Brune and J.B. Wagner Jr, *Materials Research Bulletin* **30** (1995) 573

[45]   T. Ida, H. Saeki, H. Hamada and K. Kimura K *Surface Review Letters* **3** (1996) 41

[46]   F.O. Lucas *et al.*, *Journal of Physics D: Applied Physics*, **40** (2007) 3461

[47]   L. Brewer and N.L. Lofgren, *Journal of the American Chemical Society* **72** (1950), 3038

[48]   I.V. Fedoseev, A.A. Ponomarev, E.N. Gilbert, L.N. Shabanova G.A. Kolosova, U.S.S.R. SU 1,696,543 (Cl. C22 B15/00) (1991)

[49]   I.L. Botto and O.R. Nascimento, *An. Asoc. Quim. Argent* **80** (1992) 321

[50]   J. P. Remeika, B. Batlogg, *Materials Research Bulletin* **15** (1980) 1179

[51]   W. Sesselmann, T. J. Chuang *Surface Science* **176** (1986) 32

[52]   K. Fukumi, A. Chayahara, H. Kageyama *Journal of non-Crystal Solids* **259** (1999) 93

[53]   Y. Zhang and J. Y. Tang, *Materials Letters* **61**:17 (2007) 3708

[54]   A. Neuhous and K. Recker, Crystal Growth, Pergamon Press, Oxford (1967).

[55]   M. Soga, R. Imaizumi, Y. Kondo and F. Okabe, *Journal of the Electrochem. Soc.: Solid State Science* **115**, (1967) 388.

[56]   M. Soga, R. Imaizumi, Y. Kondo and T. Okabe *Journal of the Electrochemical Society* **114** (1967) 388

[57]   S.G. Parker and J.E. Pinnell, *Electrochem. Soc.: Solid State Science* **117** (1970) 107.

[58]   A.F. Armington and J.J. O'Conner, *ibid.* **34**, (1969) 367

[59]   A. Kawamori, K. Edamatsu and T. Itoh, *Journal of Crystal Growth* **237 – 239** (2002) 1615

[60]   A. Yanase and Y. Segawa, *Surface Science* **357–358** (1996) 885

[61]   Q. Guo, L. Gui and N. Wu, *Applied Surface Science* **99** (1996) 229

[62]   M. Nakayama, A. Soumura, K. Hamasaki and H. Nishimura, *Physical Review B* **55** (1997) 10099

[63] N. Nishida, K. Saiki, and A. Koma, *Surface Science* **34** (1995) 149

[64] F.O. Lucas *et al., Journal of Crystal Growth* **287** (2006) 112

[65] G. E. McGuire, *Semiconductor Materials and Process Technology Handbook* Noyes Publications (1988)

[66] M. Ohring, *The materials Science of Thin Films* Academic Press (1992)

[67] R. Glang in *Handbook of Thin Film Technology,* L. I. Maissel and R. Glang ed., McGraw-Hill, New York (1970)

[68] L. Holland, *Vacuum Deposition of Thin Films* Chapman and Hall, London (1966)

[69] Sir William Crookes, *"On radiant matter"* a lecture delivered to the British Association for the Advancement of Science, at Sheffield, Friday, August 22, 1879. Available on http://en.wikipedia.org

[70] I. Langmuir, *Proceedings of the National Academy of Sciences of the United States of America* **14** (1928) 627

[71] G. L. Rogoff, *IEEE Transactions on Plasma Science* **19**,(1991) 989

[72] A. Grill, *Cold Plasma in Material Fabrication, From Fundamental to Applications* New York: IEEE Press (1994)

[73] S. M. Rossnagel, J.J. Cuomo and W.D. Westwood, *Handbook of Plasma Processing Technology,* Park Ridge: Noyes (1990)

[74] Rutscher A and Deutsch H, *Wissensspeicher Plasmatechnik* Leipzig: Fachbuchverlag (1983)

[75] H. Conrads and M. Schmidt, *Plasma Sources Science Technology* **9** (2000) 441

[76] N. St. J. Braithwaite, *Plasma Sources Science Technology* **9** (2000) 517

[77]   T. Matsui, J.B. Wagner, Jr., in: P. Hagenmuller, W. Van Gool (Eds.), *Solid Electrolytes*, Academic Press: New York (1978)

[78]   J. Bardeen, *Journal of* Less *Common Materials* **62** (1978) 447

[79]   K. Tennakone, S. Punchihewa and R. Tantrigoda, *Solar Energy Materials* **18** (1989) 217

[80]   G. Rousselet, P. Capdeviene and M. Maumy, *Tetrahedron Letters* **34** (1993) 6395

[81]   A.E. Harms, T.R. Stille and S.K. Toylor *Organometallics,* **13** (1994) 1456

[82]   R. Pinkos, European Patent, Appl. EP 632,027 (Cl. C07D215/14) (1995)

[83]   M. Shimomura, S. Tsurumaki, Jpn. Kokai. Tokkyo Koho JP 63,267,434 [88,267,434] (Cl. B01 J20/26) (1988)

[84]   T. Matsushita, Jpn. Kokai Tokkyo Koho, JP 61,203,969 [86,203,969] Cl A61 L9/01) (1986)

[85]   A. Nakamura, G. Asahi, J. Zaidan, Kenkyu Seika Hokoku 2 (1994) 291

[86]   S. Okamoto and Y. Masumoto, *Japanese Journal of Applied Physics Part 1* **34** (1995) 128

[87]   K. Oochi, Jpn. Kokai Tokkyo Koho JP 03,181,188 [91,181,188] (Cl. H01 S3/097) (1991)

[88]   Y.X. Zhao, X.L. Tang and B.Q. Liang, *Zhongguo Jiguang* **15** (1988), p. 211.

[89]   G. Reboul, *Comptes Rendus* **153** (1911), p. 1215

[90]   R.S. Caldwell, U.S. US 4,904,576 (Cl. 430,495 G02C1/72) (1990)

3

Structural and Morphological Properties

3.1   Introduction

The structural and morphological properties of thin films are of prime importance because they provide much information about the nature of the semiconductor material. In this chapter we present the detailed results of x-ray diffraction (XRD) and atomic force microscopy (AFM) measurements of thin films of CuCl. This begins with a very brief theoretical background of the subject, followed by the experimental results.

3.2   Literature Review

3.2.1   X-Rays

X-rays are electromagnetic waves of very short wavelength occupying the region between gamma and ultraviolet rays in the electromagnetic spectrum [1]. They were discovered by Roentgen in 1895 and found a first application in studying the internal structure of opaque objects (radiography). In 1912, Max von Laue discovered x-ray diffraction which was also the same year that W.H. Bragg and his son, W.L. Bragg, analysed Laue's experiment and gave necessary conditions for diffraction in a simpler

mathematical form than that of Laue. They proceeded by applying x-ray diffraction to crystal structures and in the following year deduced the structures of sodium chloride (NaCl), potassium chloride (KCl), potassium bromide (KBr), and potassium iodide (KI) for the first time ever, which were all hexagonal in structure [2]. In this section we only intend to give a brief review of x-rays and x-ray diffraction techniques as tools in the characterisation of thin films; a comprehensive review of these techniques can be found in many excellent books and reviews including [3,4,5,6].

Following from Cullity [6] and Brown and Forsyth [7], x-rays are produced when electrically charged particles of sufficient kinetic energy are rapidly decelerated. Traditionally electrons are used for this purpose and the process takes place in an x-ray tube, which contains the source of electrons and two metal electrodes. The two commonest targets used in today's laboratory x-ray tubes are copper and molybdenum targets, with characteristic wavelengths of 0.1540590 and 0.0709317 nm, respectively. A high voltage of the order of tens of kilovolts is maintained across the electrodes and drives the electrons to the anode, which they eventually strike with a very high velocity. X-rays are thus produced. If e, m, v and V are the charge of the electron (1.60 X 10^{-19}C), mass of the electron (9.11 X 10^{-31}kg), electron velocity in m/sec just before collision and the voltage across the electrodes, respectively, then the kinetic energy (K.E) of the electron on collision may be expressed as:

$$K.E. = eV = \frac{1}{2}mv^2$$
(3.1)

The majority of the kinetic energy of the electrons is converted into heat; this necessitates that the anode should be cooled during operation.

48

X-rays are usually detected using fluorescent screens, photographic plates and counters. Most recently Bowen and Tanner [8] reviewed the detectors for x-ray metrology in semiconductor manufacturing, in particular single-point, linear and aread detectors.

Single-point detectors include scintillation counters, proportional counters, ion chambers and silicon-based sensors (PIN diodes). Silicon sensors have very good resolution, very high dynamic range and extremely low noise, thus they are used for efficient measurement of weak signals. Scintillation counters offer a dynamic range from 0.2 to 10^8 cps, thus they are also frequently used, while on the other hand proportional counters saturate at about 10^5 cps and ion chambers are not photon counting. Linear and aread detectors are based on Si sensor arrays or on wire proportional counters. Sometimes fibre optic coupled phosphors are used to gain enough signal. The two dimensional detectors have the advantage of high-speed data acquisition and the ability to post-process data.

3.2.2 X-ray Diffraction

Bragg's Law

The study of x-ray diffraction is usually approached either using the kinematical or the dynamical theory. In kinematical theory, one can ignore rediffraction effects since this theory assumes that a negligible amount of energy is transferred to the diffracted beam. This theory is fairly accurate for the geometry of diffraction in all cases, and also satisfactorily accurate for intensities when scattering is very weak (thin crystals, surface scattering and diffuse scattering). However, in situations where the scattering is strong (thick perfect crystals), the kinematical theory fails and the diffraction patterns are governed by the dynamica theory due to the non negligible x-ray

absorption. The mathematical formalism of the dynamic diffraction theory is found by solving Maxwell's equation in a periodic medium. A comprehensive treatment of these theories has been reviewed by many researchers including [9,10,11,12,13,14].

If we adopt the kinematical theory, x-ray diffraction is associated with rays consisting of a large number of scattered rays propagating in a constructive manner (constructive interference). Figure 3.1 shows a section of crystal whose atoms are arranged in a set of parallel planes, A, B and C, with inter-planar distance of d. A monochromatic x-ray of wavelength λ is incident on the crystal at an angle of θ in such a way that the incident beam and the normal are all in coplanar. For the particular condition described by figure 3.1, the only diffracted beam formed is the one for which the angle of incidence θ is equal to the reflected angle. We consider rays 1 and 2, which are scattered by atoms K and L, thus leading to constructive interference. The path difference Γ for the rays *1K1′* and *2L2′* can be deduced from elementary plane geometry as:

$$\Gamma = ML + LN = \text{d}′\sin\theta + \text{d}′\sin\theta \qquad\qquad (3.2)$$

This is also the path difference for overlapping rays scattered by *S* and *P* as shown in figure 3.1.
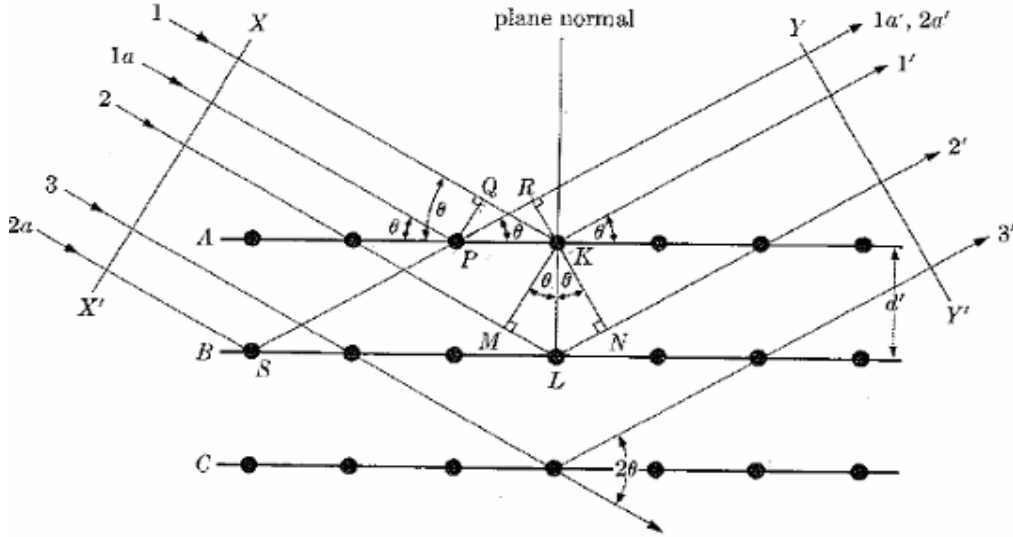
Figure 3.1: *Diffraction of x-rays by a perfect crystal [6].*

The scattered rays 1′ and 2′ will be totally in phase and cumulating to a maximum constructive interference when Γ is an integral multiple n of λ or Γ = nλ, where n is the order of interference. This gives rise to the well known Bragg equation:

$$n\lambda = 2d' \sin \theta \qquad (3.3)$$

We can rewrite equation (3.3) as follows:

$$\frac{n\lambda}{2d'} = \sin \theta \qquad (3.4)$$

and for the diffraction to occur, equation (3.4) must be less than 1, yielding:

$$\lambda < 2d' \qquad (3.5)$$

Scherrer Formula

The mechanism described so far assumes ideal conditions: a perfect crystal and an incident beam that is composed of perfectly parallel and strictly monochromatic radiation. In actual fact these conditions never exit and this gives rise to two limiting angles where diffraction occurs. In the region between $2\theta_1$ and $2\theta_2$, the scatter results in a constructive interference whose maximum is at Bragg angle $2\theta_B$ while in other regions destructive interference takes place resulting in no diffraction. If there are (m + 1) planes in the crystal and L being the particle size, when the diffracted intensity is plotted as a function of 2θ, the width of the diffracted curve increases as the thickness of the crystal decreases, since the angular range $(2\theta_1 - 2\theta_2)$ increases as m decreases [6]. The value of B given below, is usually measured in radians where the intensity equals the full width at half maximum (FWHM) of the peak broadening intensity:

$$B = \frac{1}{2}(2\theta_1 - 2\theta_2) = \theta_1 - \theta_2 \qquad (3.6)$$

We may proceed by writing the path difference equation for these two angles in a similar fashion to equation (3.2) as:

$$2L \sin \theta_1 = (m + 1)\lambda \qquad (3.7)$$

and

$$2L \sin \theta_2 = (m - 1)\lambda \qquad (3.8)$$

respectively. Subtracting these two equations lead to:

$$L(\sin \theta_1 - \sin \theta_2) = \lambda \qquad (3.9)$$

and by applying a trigonometric identity, the resulting equation becomes:

$$2L \cos\left(\frac{\theta_1 + \theta_2}{2}\right) \sin\left(\frac{\theta_1 - \theta_2}{2}\right) = \lambda \qquad (3.10)$$

If both θ_1 and θ_2 are in radians and are nearly equal to $2\theta_B$, so that the sum of θ_1 and θ_2 gives $2\theta_B$ approximately, which is usually the case in most experimental runs and:

$$\sin\left(\frac{\theta_1 - \theta_2}{2}\right) = \left(\frac{\theta_1 - \theta_2}{2}\right) \qquad (3.11)$$

Therefore by substituting equation (3.6) into equation (3.10) and making L the subject of the formula yields the Scherrer formula:

$$L = \frac{\lambda}{B \cos \theta_B}, \qquad [\because \theta_1 + \theta_2 = 2\theta_B] \qquad (3.12)$$

A more exact treatment of this equation gives:

$$L = \frac{0.9\lambda}{B \cos \theta_B} \qquad (3.13)$$

The factor of 0.9 arises from the assumed line shape of the diffraction peak and the assumed crystallite shape, which is only approximate [8]. The Scherrer equation, was extensively used in estimating the average crystallite sizes of the CuCl films.

Internal Elastic Strain

The elastic strain in films can either be on the macro or on a microscale. According to [9], macroscale refers to the situation where the whole material is subjected to some directional residual tensional or compressional force. The resultant strains will be manifested in terms of an increase (tensional) or decrease (compressional) in the lattice spacing parameters (d_{hkl}). This type of strain is associated with a shift in the diffracted peaks. On the other hand, microscale refers to a situation in which the directions and magnitudes of the internal strains vary from crystal to crystal. This gives rise to the broadening of diffracted peaks as opposed to a shift of the diffracted peaks. The relevant equation governing the relationship between the diffracted peaks and the elastic strain is given by differentiating the first order (n = 1) Bragg equation of equation (3.3) with respect to d and θ:

$$0 = 2d \cos \theta \, \delta\theta + 2 \sin \theta \, \delta\theta \tag{3.14}$$

hence

$$\frac{\delta d}{d} = \varepsilon = - \, \delta\theta \cdot \cot \theta \tag{3.15}$$

Since the broadening, B, expressed as a half height peak, with $2\delta\theta$ is given by

$$\varepsilon = -\frac{B}{2\tan\theta}, \qquad [\because \cot\theta = \frac{1}{\tan\theta}] \qquad\qquad (3.16)$$

This equation is similar to the Scherrer equation but the important difference is that B varies as tan θ while in Scherrer equation B varies as 1/cos θ.

3.2.3   Atomic Force Microscopy (AFM)

Atomic force microscope (AFM) creates a highly magnified, three dimensional image of a surface. The image is generated by monitoring the motion of an atomically sharp probe as it scans across a surface. It has the advantage of extremely high magnification (order of 1,000, 000x), and produces presentation of images in three dimensions, which optical and electron microscopy cannot do. Also it is capable of imaging both conductive and non-conductive materials as opposed to scanning tunnelling microscopy (STM), which can only be used on conductive surfaces [15]. Since the invention of AFM [16], it has found several applications in surface science based technology including the semiconductor, telecommunications, biological, chemical automotive, aerospace and energy industries.

According to [15,17] a typical AFM consists of a cantilever attached to a sharp probe (tip) at its end. When a sample surface is brought into close proximity to the tip, there exists a Coulombic repulsion force between the atoms at the sample surface and the atoms of the tip. The precise mechanical motion in an AFM tip is usually carried out using an electrochemical transducer commonly known as piezoelectric ceramic. If the mass and stiffness of the cantilever with the tip are sufficiently small, the force F

between the tip and the sample leads to a deflection of the cantilever according to the well known Hook's law:

$$F = kx \qquad\qquad (3.17)$$

where x is the deflection of the cantilever out of equilibrium position.

By examining equation (3.17), one could conclude that the deflection of the cantilever is directly proportional to the Coulomb forces between the tip and the surface sample. Since these forces are within a small range, measuring them on the surface gives a pictorial representation of the atom on the surface and thus the surface topography. The deflection of the cantilever is typically measured with a laser spot reflected from the top of the cantilever as shown in figure 3.2. The position of the reflected spot is determined by a photodiode and compared to the equilibrium value.

Photodiode
(Detector)

Laser

Detector and feedback control system

Cantilever and tip

Sample surface

Piezoelectric ceramic
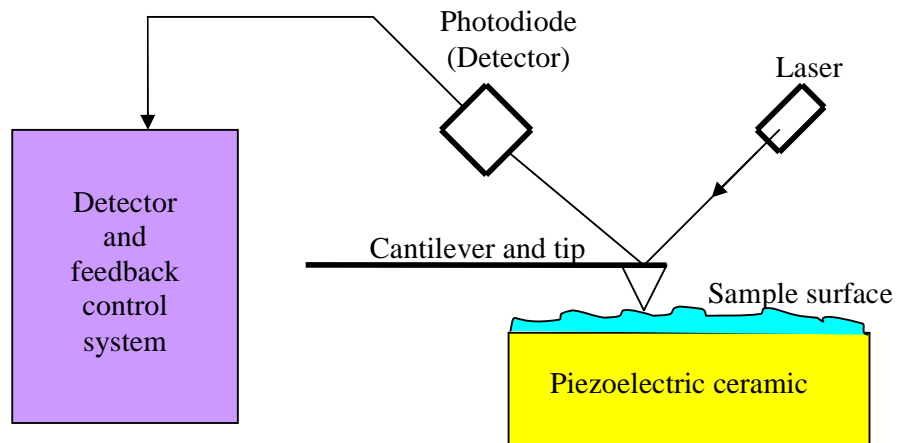
Fig 3.2: Schematic representation of a typical modern AFM [7].

Under appropriate calibration the deflection of the spot gives the deflection of the cantilever and thus the change in height of the surface. An electronic feedback control system is used to adjust the tip–to–sample distance in order to keep the force between the tip and the sample constant.

There are several different imaging modes that can be used while characterising the surface of a material using the AFM. The commonest modes of operation are contact and tapping modes [18]. In contact mode operation, the force between the tip and the surface is kept constant during scanning by maintaining a constant deflection [19]. In tapping mode, the tip is vertically oscillated at its resonance frequency [20]. When the sample approaches the vibrating tip, they come into intermittent contact (tapping) thereby lowering the vibrational amplitude. The amplitude drop is used for the feedback. In comparison, imaging in contact mode and tapping mode shows that soft surfaces are less modified in the tapping mode [21], thus they are very useful in imaging biological and soft samples. In this study, the contact mode was used in obtaining surface topographs and roughness analysis of all the samples

3.3   Experimental

3.3.1   Film Deposition

The detailed procedure for the substrate preparation and CuCl film deposition has been given extensively in sections 2.2 and 2.7.5, so only a brief description of the process is given here. Thin films of CuCl were deposited on cleaned square cut soda lime glass, indium tin oxide (ITO) and silicon substrates using an Edwards's auto 306

vacuum evaporation system at a base pressure of the order of 1×10^{-6} mbar. The thickness of films was between $100 - 500$ nm at a constant growth rate of ~ 0.5 nms^{-1} as indicated by the thickness monitor.

Some of the deposited CuCl films were plasma treated using an Oxford Instruments Plasma Lab plus 80 reactive ion etcher (RIE) in order to introduce oxygen atoms in the CuCl for the improvement of the electronic conductivity. Oxygen and argon were let in via dedicated channels at a ratio of 4:1 (O_2/Ar), the RF power was 300 W, while the chamber pressure was held at 50 mTorr. The duration of the plasma treatment was mainly 1, 2, and 3 minutes for the different samples.

3.3.2 Characterisation Techniques

The phase purity and preferred orientation of the deposited cuprous chloride films at room temperature were examined on a Bruker AXS D8 Advance X-ray diffractometer, using monochromatic Cu k_α radiation ($\lambda = 0.154$ nm). The standard setting for the x-rays generator was 40 kV at an electron current of 40 mA. The scans were measured in the Bragg–Brentano geometry (θ–2θ) in a range of 25º to 80º.

The room temperature surface morphology of the films was examined on a Digital Instruments Nanoscope III atomic force microscopy (AFM). The micrographs were taken in contact mode with a Si_3N_4 tip manufactured by Digital Instruments. In all cases, more than one image was taken from neighbouring areas to confirm the true representation of the film. Typical data taken from AFM height measurements included root mean square surface (RMS roughness), average roughness (RA) and all 3D images were analysed using the Digital Instruments (DI) software.

3.4   Results

3.4.1   Structural Properties of the As Deposited CuCl thin Film

Figures 3.3 – 3.5 show typical x-ray diffraction spectra for the CuCl/Glass, CuCl/ITO and CuCl/Si structures, respectively. The spectra were analysed using the Diffrac Plus evaluation software. The quantification of the peak full width at half maximum (FWHM) of the three structures was carried out by deconvolving the instrument broadening from the measured FWHM [8]:

$$B^2 = B^2_{measured} - B^2_{instrument} \qquad\qquad (3.18)$$

where $B_{measured}$ is the measured full width at half maximum and $B_{instrument}$ is the instrument broadening. A standard strain free single crystal Si (100) was used for the calibration and estimation of $B_{instrument}$.

Table 3.1 presents some selected Miller indices for the crystal planes of pure zincblende γ–CuCl, their 2θ values, d–spacing and relative intensities, all from the Diffrac Plus PDFmaint XRD reference data.

Plane (hkl)	2θ (º)	d–Spacing (Å)	Relative Intensity
(111)	28.522	3.1270	100
(200)	33.027	2.7100	8
(220)	47.437	1.9150	55
(311)	56.290	1.6330	30
(400)	69.348	1.3540	6
(331)	76.590	1.2430	10
(422)	88.350	1.1054	8

Table 3.1: *Diffrac Plus PDFmaint XRD reference data for zincblende CuCl.*
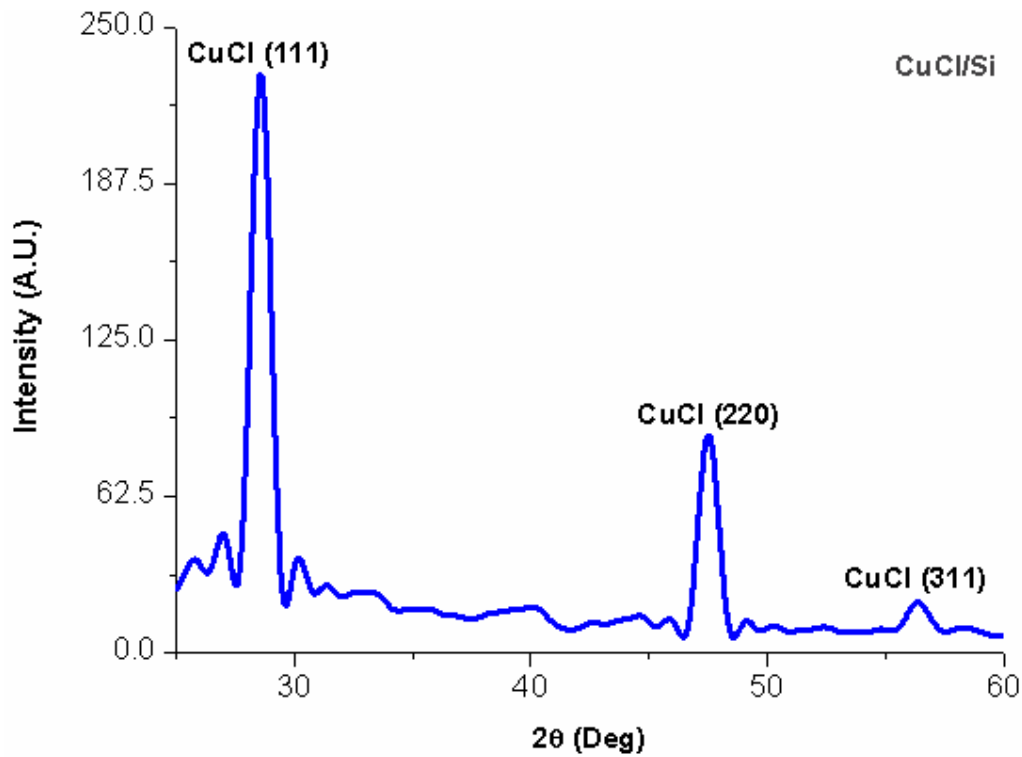
Figure 3.3: *X-ray diffraction spectrum of the as deposited CuCl/Si structure.*
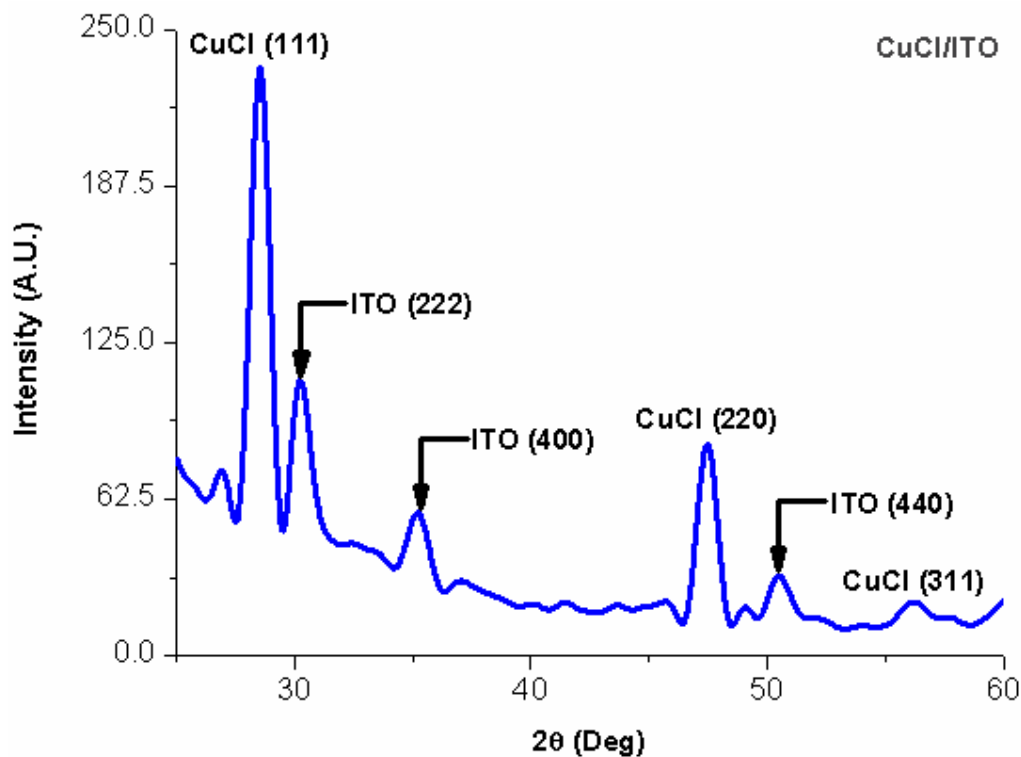
Figure 3.4: X-ray diffraction spectrum of the as deposited CuCl/ITO structure.

The presence of well defined Bragg peaks as seen in figures 3.3 – 3.5 reveals the polycrystalline nature of the deposited cuprous chloride films and the 2θ values of these peaks are in excellent agreement with those of the ICDD powder diffraction database as seen in table 3.1. There are three main peaks common to all the spectra. The peaks centred around ~ 28.5º, ~ 47.5º and ~ 56.4º correspond to the (111), (220) and (311) reflections, respectively. These are characteristic of γ-CuCl in the zincblende configuration. The x-ray diffraction pattern of these figures also indicates that the (111) plane is the preferred orientation, which is also in excellent agreement with previous measurements of CuCl on (0001) Al_2O_3 [22], CuCl on glass and CuCl on Si substrates [23]. The other 2θ peaks occurring at ~ 30.55º, ~ 35.22º and ~ 50.47º on the CuCl/ITO structure corresponds to the ITO (222), ITO (400) and ITO (440), respectively [24].
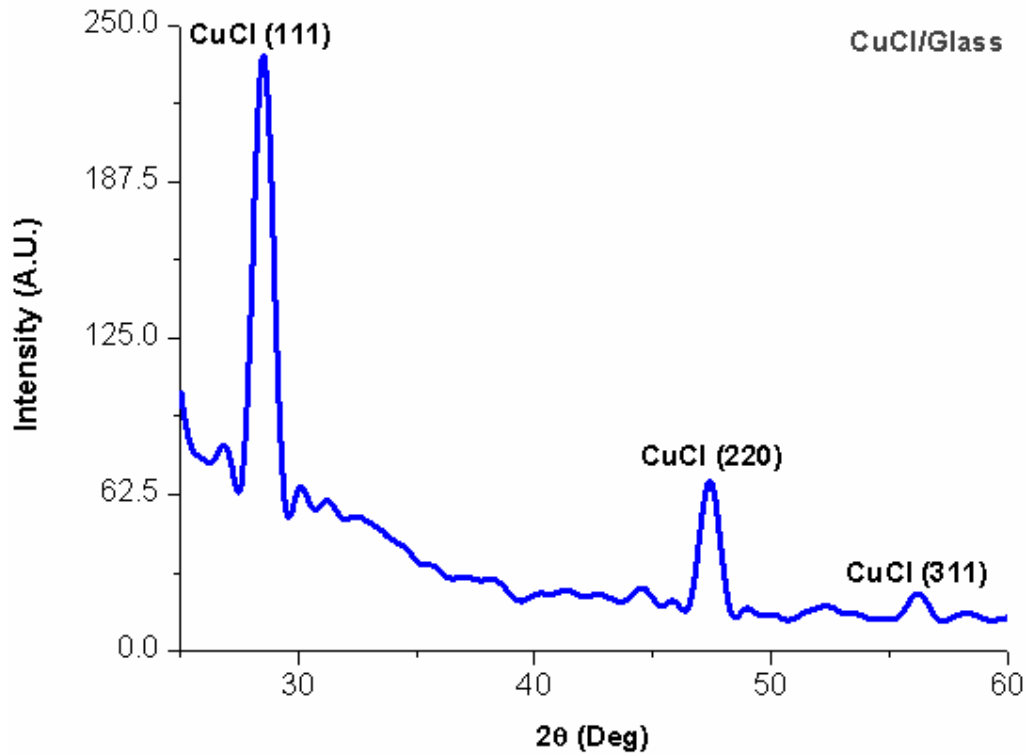
Figure 3.5: *X-ray diffraction spectrum of the as deposited CuCl/Glass structure.*

Figures 3.6 shows a closer view of the dominant γ–CuCl (111) peak for the three structures, which occurs at $2\theta \sim 28.500º$, $\sim 28.535º$ and ~ 28.571 for CuCl/Glass, CuCl/ITO and CuCl/Si structures, respectively. The very slight difference between the values of these peaks may be due to a very small macro strain in the films as explained by Hammond [25].

The microstructural properties (particle size, L and micro-elastic strain, ε) of the three structures were deduced from an analysis of the x–ray diffraction spectra using the equations (3.13) {Scherrer equation} and (3.16).
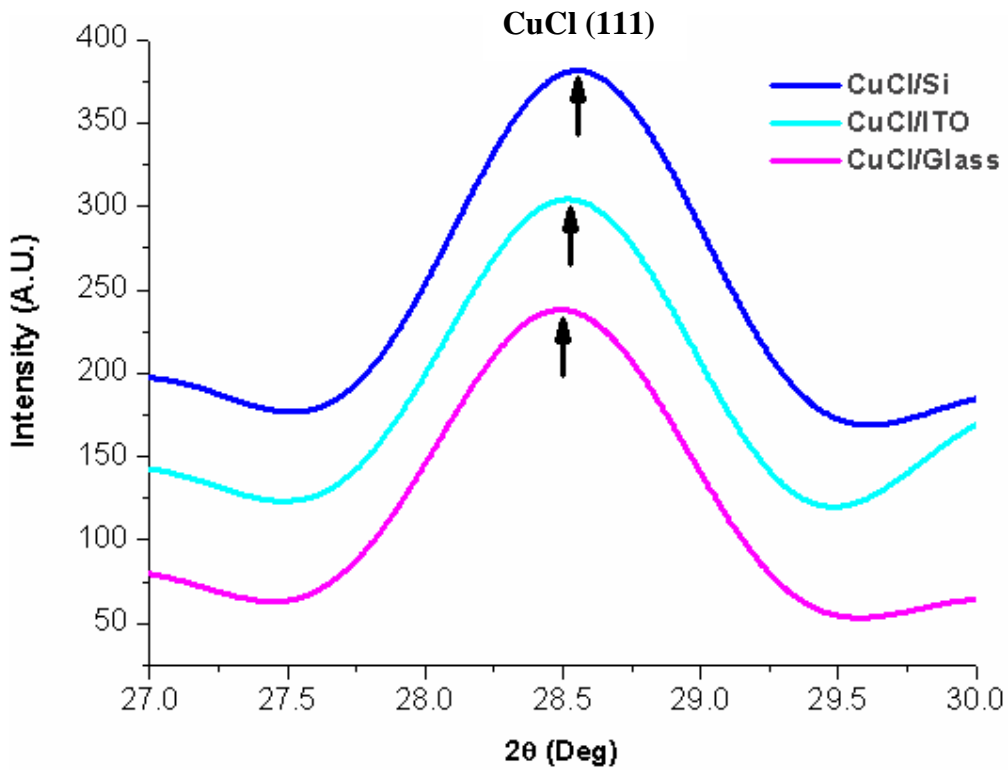
Figure 3.6: *X-ray diffraction spectra of the as deposited CuCl films.*

Structure	B_{inst} (Radians)	B (Radians)	L (nm)
CuCl/Glass	0.003	0.01651	9.55
CuCl/ITO	0.003	0.01623	9.71
CuCl/Si	0.003	0.01640	9.61

Table 3.2: *The instrument broadening $B_{instrument}$, experimental values of the FWHM of the (111) peak broadening B and the particle size L for as deposited CuCl/Glass, CuCl/ITO and CuCl/Si films.*

The corresponding values of the room temperature normalized FWHM of the dominant (111) peak broadening B and particle size L for the three structures are presented in table 3.2.

According to table 3.2, the values of the average crystallite size for the three structures are almost the same irrespective of the underlying substrates: 9.55 nm, 9.71 nm and 9.61nm for the CuCl/Glass, CuCl/ITO and CuCl/Si structures, respectively. The slight differences for the values of the particle size of the three structures may be due to the difference in the underlying substrate roughness of the films. For instance the glass substrate is less polished and slightly rougher than those of ITO and Si substrates, thus it reasonable to expect a slightly less smooth film on glass substrates.

3.4.2   Structural Properties of the O_2 Plasma Treated CuCl Films

In order to understand the effect of oxygen plasma treatment on the CuCl films, the x-ray diffraction measurements were taken before and after each plasma treatment for all the samples. The structural characteristics of the plasma immersed films are presented in figures 3.7 – 3.10. Similar to the as deposited films of figures 3.3 – 3.5, the plasma treated films are polycrystalline in nature. These spectra comprise of 2θ peaks centred around ~ 28.5º, ~ 47.5º and ~ 56.4º corresponding to the cuprous chloride (111), (220) and (311) reflections, respectively. For an O_2 plasma immersion of up to 3 minutes, there was no difference between the peak intensities before and after the plasma immersion, although there was a slight change in the value of the FWHM of the diffracted peaks. This indicates that for up to 3 minutes, plasma immersion did not lead to etching or significant crystal damage of CuCl films.

However for durations greater than three minutes, we have observed a reduction in the intensity of the diffraction peaks in addition to a diffraction peak broadening when compared to the initial untreated films and films treated for a duration up to 3 minutes. Figure 3.10 illustrates the effect of 7 minutes O_2 plasma immersion on CuCl films.
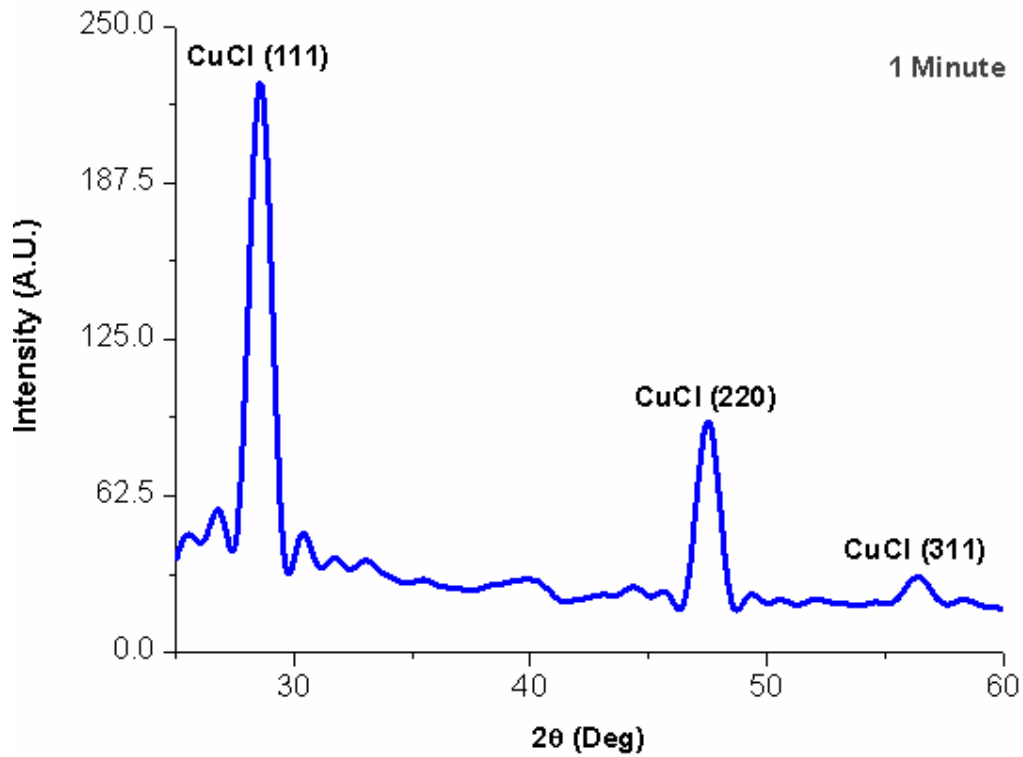
Figure 3.7: X-ray diffraction spectrum of CuCl film plasma immersed for 1 minute.

The x-ray deduced microstructural properties (particle size L) of the structures were again deduced from the analysis of the x–ray diffraction spectra using equation 3.13 (Scherrer equation).
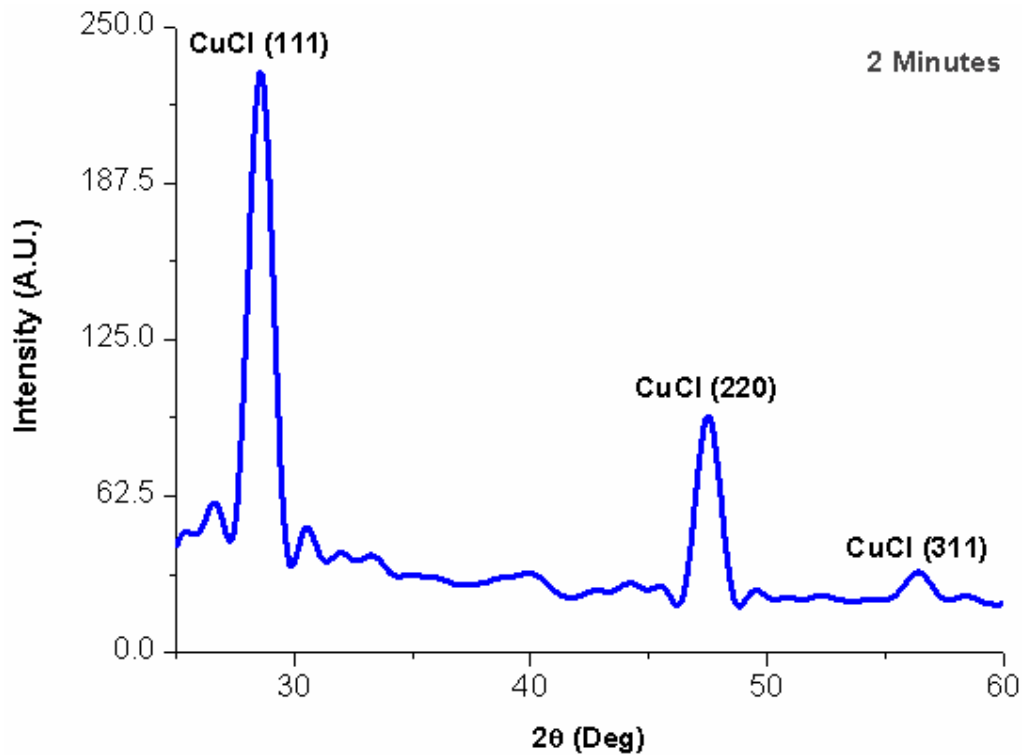
Figure 3.8: X-ray diffraction spectrum of CuCl film plasma treated for 2 minute.

According to table 3.3, the values of the average particle size for the plasma immersed films, calculated from the analysis of the FWHM of the (111) peak of figures 3.7 – 3.10 varies as a function of the plasma treatment duration. An average crystallite size of the order of 8.53 nm, 8.0 nm, 7.59 nm and 5.74 nm was calculated for the plasma treated films for 1, 2, 3 and 7 minutes, respectively. Clearly one could conclude that the oxygen plasma treatment reduces the average particle size of the cuprous chloride polycrystals.

Film Type	B (Radians)	B (Radians)	L (nm)
CuCl/Si Untreated	0.00300	0.01640	9.61
CuCl/Si 1 Minute	0.00300	0.01840	8.53
CuCl/Si 2 Minutes	0.00300	0.01990	8.00
CuCl/Si 3 Minutes	0.00300	0.02097	7.53
CuCl/Si 7 Minutes	0.00300	0.02722	5.74

Table 3.3: *The instrument broadening $B_{instrument}$, experimental values for the FWHM of the (111) peak broadening, and average particle size L for plasma immersed CuCl films.*
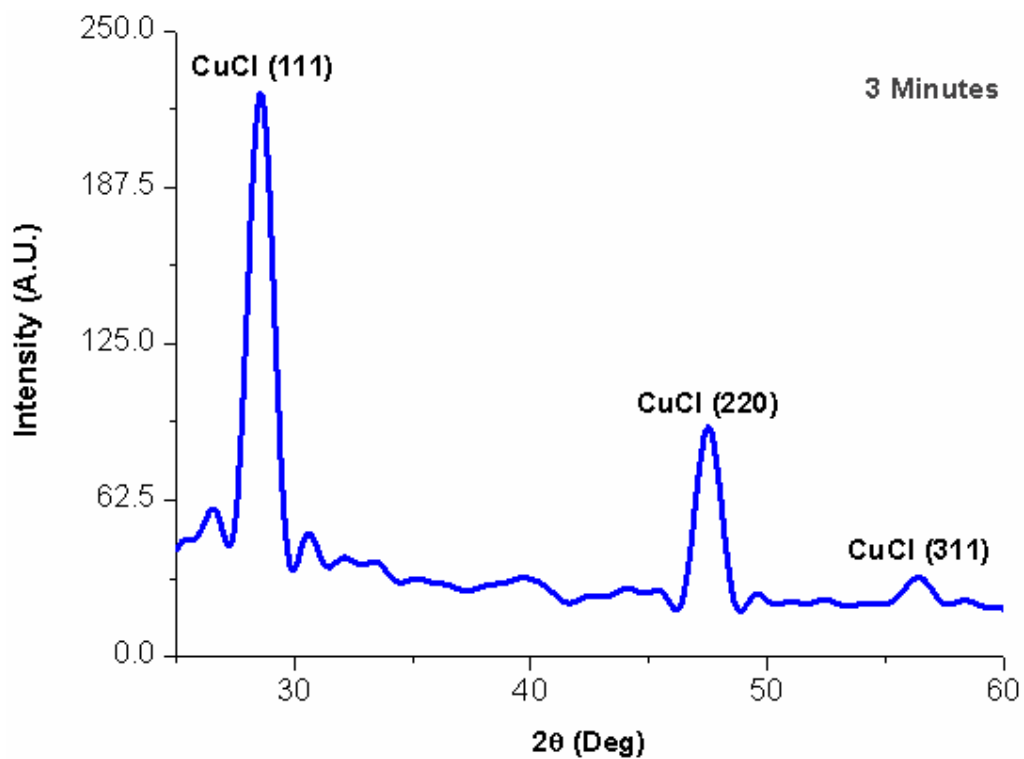
Figure 3.9: *X-ray diffraction spectrum of CuCl film plasma immersed for 3 minutes.*
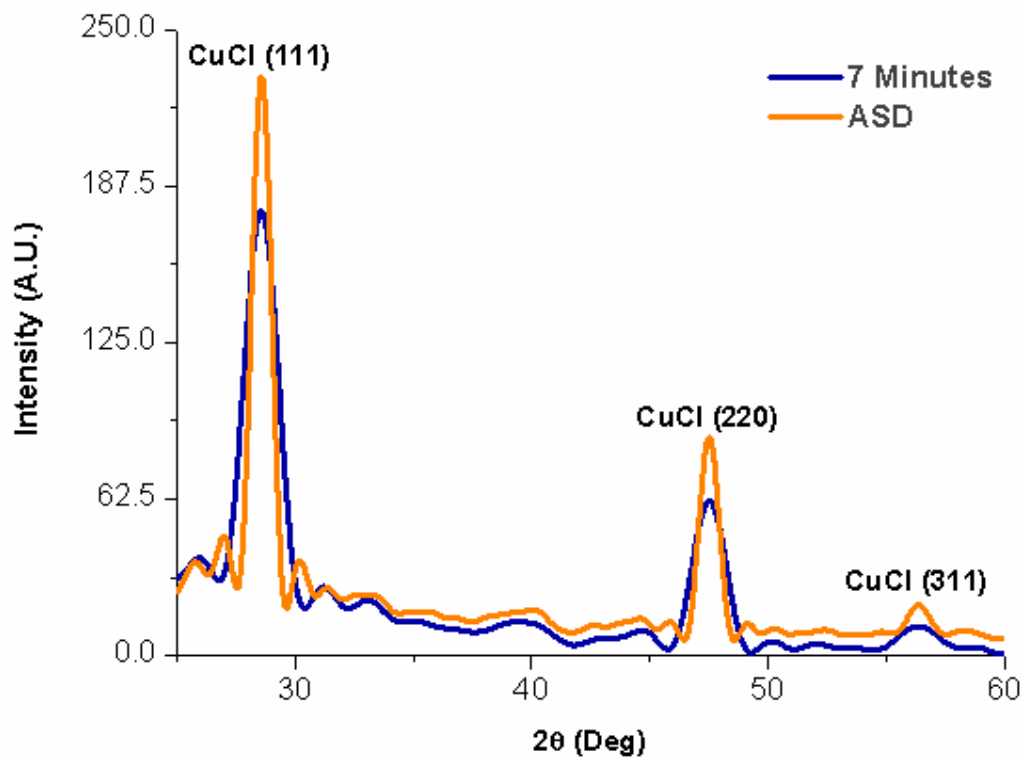
Figure 3.10: *X-ray diffraction spectra of the as deposited and 7 minutes plasma immersed CuCl films.*

3.4.3 Morphological Properties of the As Deposited CuCl Films

Contact mode atomic force microscopy (AFM) was used to characterize the surface morphology of the three structures. A typical 3–D image for the CuCl/Glass, CuCl/ITO and CuCl/Si structures is shown in figures 3.11, 3.12 and 3.13, respectively.

Structure	RMS (nm)	RA (nm)
CuCl/Glass	9.4	7.54
CuCl/ITO	8.8	6.93
CuCl/Si	9.0	7.15

Table 3.4: The root mean square (RMS) and average roughness (RA) values of CuCl films.
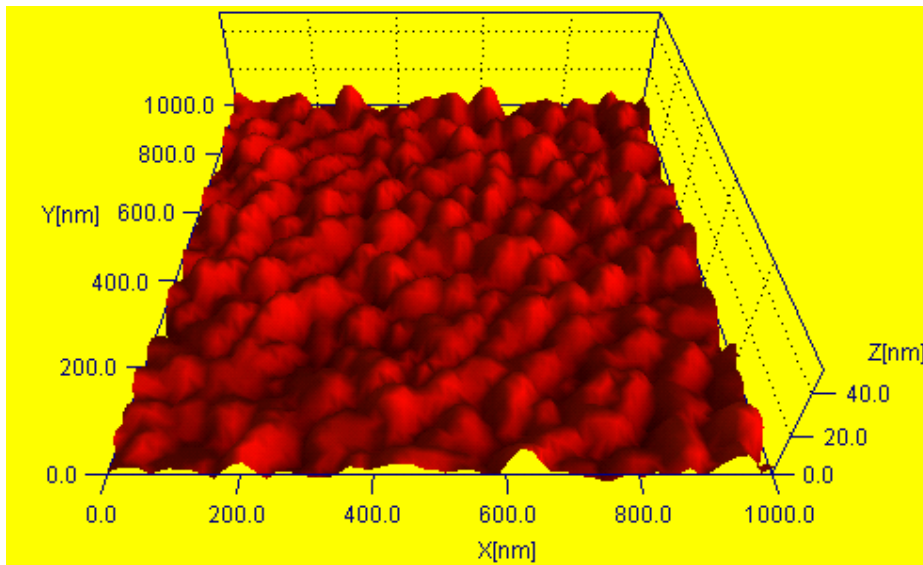
Figure 3.11: Typical 3–D AFM image of the as deposited CuCl/Glass structure.

The detailed root mean square (RMS) and average roughness (RA) analysis evaluated using the Digital Instruments software is presented in table 3.4.
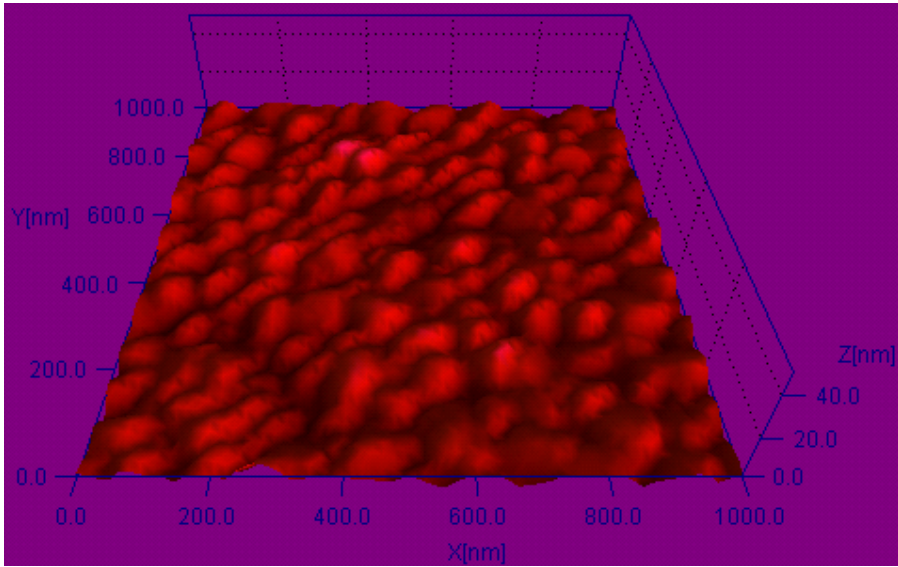
Figure 3.12: *Typical 3–D AFM image of the as deposited CuCl/ITO structure.*
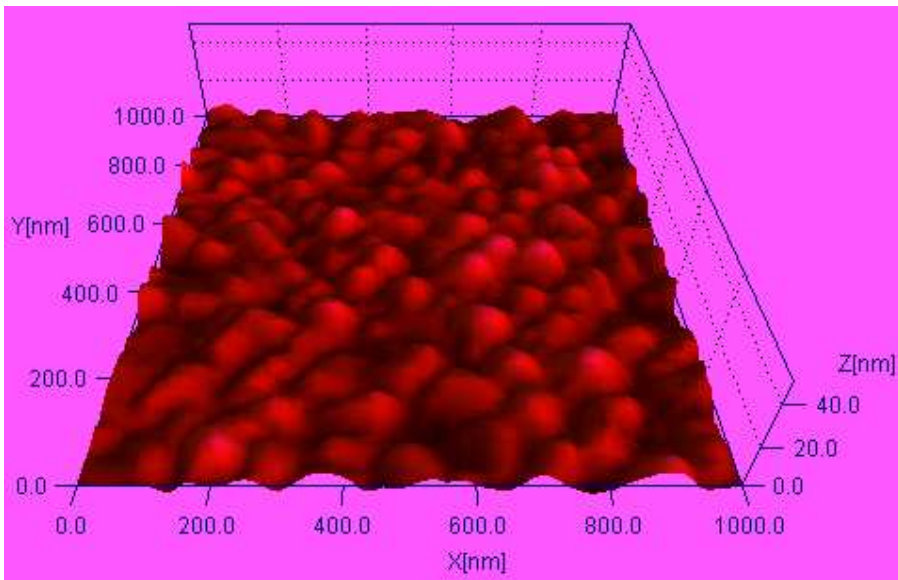
Figure 3.13: *Typical 3–D AFM image of the as deposited CuCl/Si structure.*

Similar to the x-diffraction measurements of the untreated films, table 3.4 indicates that the roughness of the CuCl films are almost the same irrespective of the underlying substrate. An RMS roughness value of 9.4 nm, 8.8 nm and 9.0 nm was

calculated for the cuprous chloride films deposited on glass, ITO and Si substrates, respectively. The slight difference among the values of the RMS and RA of the three structures as illustrated in table 3.4 may again be ascribed to the difference in the underlying substrate roughness of the films as previously explained for the x-ray deduced microstructural properties.

3.4.4 Morphological Properties of the O_2 Plasma Treated CuCl Films

Typical contact mode atomic force microscopy (AFM) images of the plasma immersed CuCl/Si films are depicted in figures 3.14 – 3.17 and the results of the root mean square (RMS) and average roughness (RA) analysis evaluated using the Digital Instruments software is presented in table 3.5.
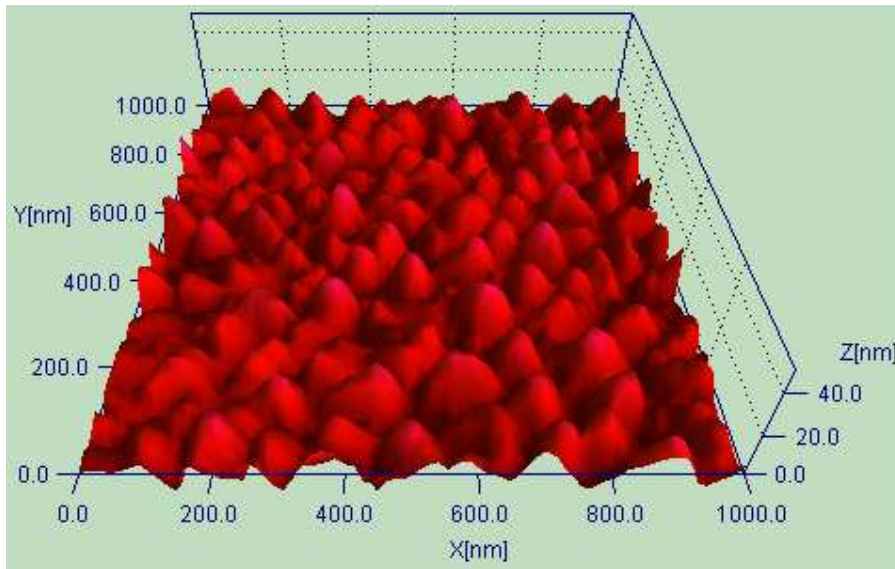
Figure 3.14: *Typical 3–D AFM image of CuCl/Si film plasma immersed for 1 minute.*
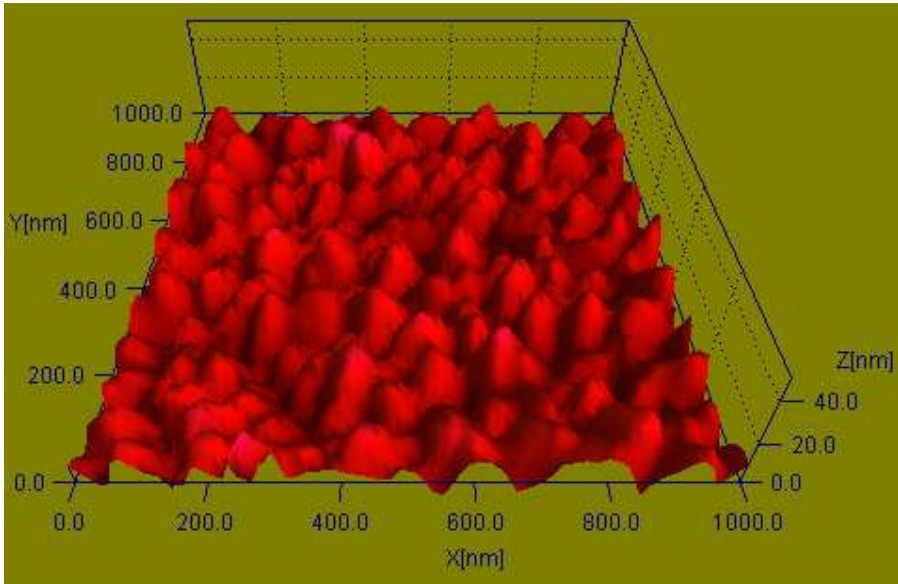
Figure 3.15: *Typical 3–D AFM image of CuCl/Si film plasma immersed for 2minutes.*
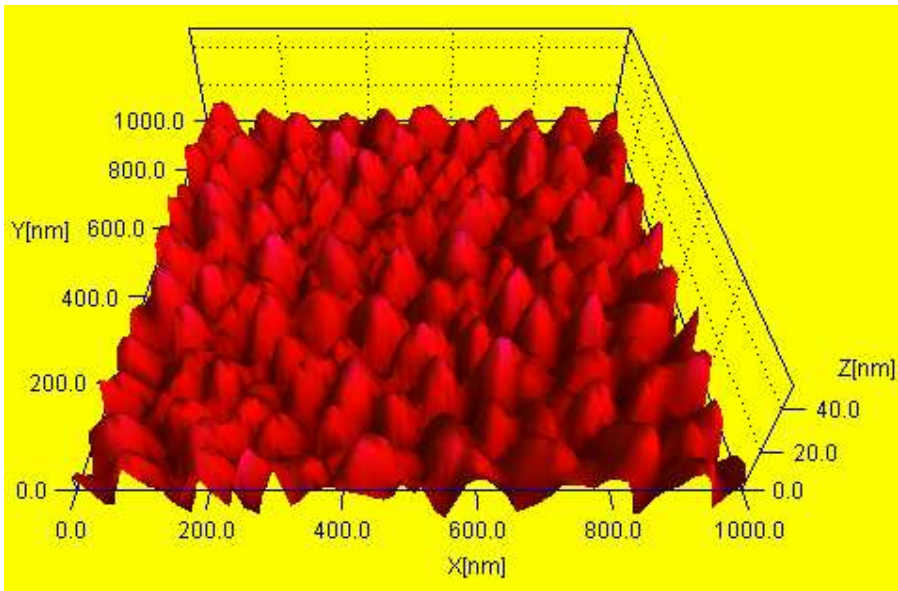
Figure 3.16: *Typical 3–D AFM image CuCl/Si film plasma immersed for 3 minutes.*

Structure	Plasma Duration (Mins)	RMS (nm)	RA (nm)
CuCl/Si	0	9.0	7.15
CuCl/Si	1	15.3	12.24
CuCl/Si	2	17.7	14.15
CuCl/Si	3	21.0	16.50
CuCl/Si	7	33.2	26.39

Table 3.5: The root mean square (RMS) and average roughness (RA) values of the plasma immersed CuCl/Si films.
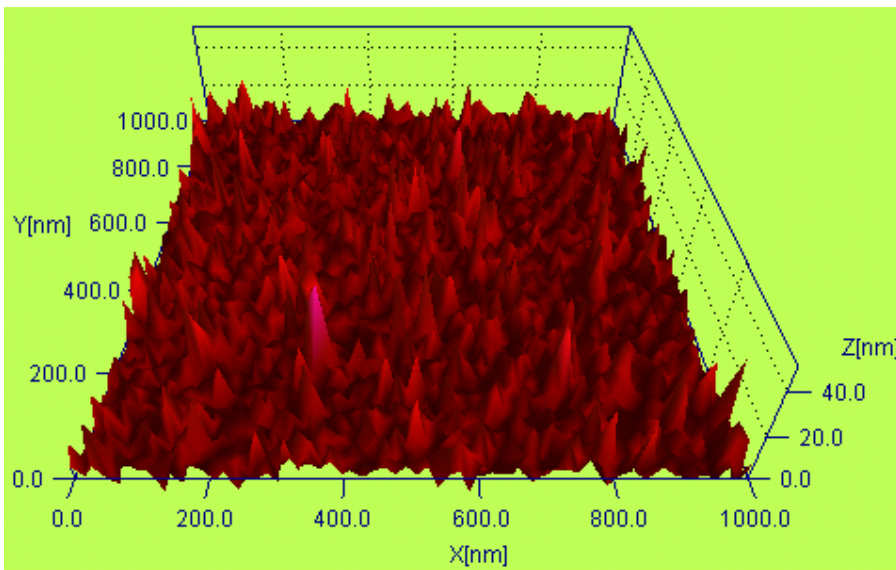
Figure 3.17: Typical 3–D AFM image of CuCl/Si film plasma immersed for 7minutes.

According to table 3.4, the roughness of the plasma treated CuCl films increases as the plasma duration increases. A value of 15.3 nm, 17.7 nm, 21.0 nm and 33.2 nm was deduced to be the root mean square (RMS) roughness value of the plasma immersed cuprous chloride films for durations of 1, 2, 3, and 7 minutes respectively.

3.5 Conclusion

In summary, the structural and morphological properties of γ-cuprous chloride films deposited on glass, ITO coated on glass and silicon substrates have been investigated. Some of the samples deposited on silicon were plasma immersed in oxygen and also examined:

- X-ray diffraction (XRD) measurements confirmed that the as deposited films were zincblende in structure and preferentially oriented in the (111) plane irrespective of the underlying substrates. An average particle size of the order of 9.6 nm ± 1 was deduced from the analysis of the FWHM of the CuCl (111) peak irrespective of the substrates.

- Similar to the x-ray diffraction experiments, contact mode atomic force microscopy (AFM) results showed a similar surface morphology and a root mean square roughness (RMS) of 9.1 ± 0.3 nm, irrespective of the substrate.

- On the other hand the microstructural properties of the O_2 plasma immersed films vary as a function of plasma immersion duration. The average particle size of the plasma treated sample varies from 8.53 to 7.43 nm for plasma immersion durations of 1 to 3 minutes. The application of plasma treatment for more than 3 minutes significantly degrades the crystal quality of the CuCl films. Atomic force microscopy measurements indicated that the plasma

74

treated CuCl films become rougher as the O_2 plasma immersed duration increases.

References

[1]   H.A. Enge, M.R. Wehr and J.A. Richards, *Introduction to Atomic Physics* Addison – Wesley Publishing Company: Reading (1972)

[2]   P.P Ewald, *Fifty years of X–Ray Diffraction,* International Union of Crystallography (1962)

[3]   B.E Warren, *X–Ray Crystallography,* Addison–Wesley Publishing Company: Reading (1969)

[4]   A. Authier, *Dynamic Theory of X–Ray Diffraction,* Oxford University Press: Oxford (2001)

[5]   U. Pietsch, V. HolΔ and T. Baumbach, *High–Resolution X–Ray Scattering,* 2nd ed., Springer: New York (2004)

[6]   B.D. Cullity, *Elements of X–Ray Diffraction,* 2nd ed., Addison–Wesley Publishing (1978)

[7]   P J Brown and J B Forsyth, *The Crystal Structure of Solids* Edwards Arnold (1979, c1973)

[8]   D. Keith Bowen and Brian K. Tanner, *X–Ray Metrology in Semiconductor Manufacturing,* CRC Press (2006)

[9]   M. Laue, *Naturwissen* **10** (1931) 133

[10]   W. Zachariasen, *Theory of X-ray diffraction in crystals,* Dover (1945)

[11]   L. Azároff, R Kaplow, N. Kato, R. Weiss, A. Wilson and R. Young, *X-ray Diffraction,* McGraw-Hill (1974)

[12]   B. Batterman and H. Cole, *Review of Modern Physics* **36** (1964) 681

[13]   A. Authier, S. Lagomarsino and B. Tanner, *X-ray and Neutron Dynamic Diffraction: Theory and Applications,* vol **367** of *NATO ASI Series* Plenum (1996)

[14]   J. Sutter, *Applications of special X-ray diffraction cases in silicon crystals,* PhD thesis, Department of Physics, Purdue University, West Lafayette, Indiana, USA (2000)

[15]   S. N. Magonov and M. Whangbo, *Surface Analysis with STM and AFM: Experimental and Theoretical Aspects of Image Analysis,* Wiley-VCH (1996)

[16]   G. Binnig, C. Quate, Ch. Gerber, *Physical Review Letters* **56** (1986) 930

[17]   G. Doyen and D. Drakova, *The Physical Principles of STM and AFM Operation,* Wiley-VCH (2004)

[18]   T. Ando, N. Kodera, E. Takai, D. Maruyama, K. Saito and A. Toda, *Proceedings of the National Academy of Science of the United States of America* **23** (2001) 12468

[19]   D. Sarid, *Scanning Force Microscopy,* Oxford University Press: New York (1991)

[20]   Q. Zhong, D. Innis, K. Kjoller and V. B. Elings, *Surface Science Letters* **290** (1993) L688

[21]   A. Wawkushewski, K. Crämer, H-J Cantow and S. N. Magonow, *Ultramicroscopy* **58** (1995) 185

[22]   M. Nakayama, A. Soumura, K. Hamasaki, H. Takeuchi and H. Nishimura, *Physical Review* B **55** (1997) 10099

[23]   L. O'Reilly, Lucas F O, G. Natarajan , P.J. McNally, D.C. Cameron, A. Reader, M. Martinez-Rosas, and A.L. Bradley, *Journal of Materials Science: Electronic Materials* **16** (2005) 415

[24]   W. J. Dausher, K. J. Nordquist, D. P. Mancini, D. J. Resnick and J. H. Baker,
       Journal of Vacuum Science Technology B **20**:6 (2002) 2857

[25]   H. Hammond, *The basics of Crystallography and diffraction* Oxford
       University Press: New York (2001)

4

Optical Properties

4.1 Introduction

Optical characterization methods are very important tools for the evaluation of the electronic structure, luminescence and photochemical properties of semiconductor materials. In this chapter we briefly review absorption and photoluminescence spectroscopy as powerful non-destructive optical characterisation techniques. We also we report on the results of the optical characterizations of γ-CuCl films.

4.2 Literature Review

4.2.1 Absorption

Absorption spectroscopy is one of the simplest and most direct methods for probing the band structure of a semiconductor material. Absorption takes place when a photon of a known energy excites an electron from a lower energy level to a higher energy level. Consequently it is possible to discover the possible transitions being made by the electron in a semiconductor by placing the semiconductor material at the output of

a monochromator. In this section we only concentrate on the fundamental absorption (band-to-band and excitons) and transition between impurities and bands.

Following from [1], absorption is defined in terms of the absorption coefficient $\alpha(h\upsilon)$ as the relative rate of decrease in light intensity $L(h\upsilon)$ along its propagation path:

$$\alpha = -\frac{1}{L(h\upsilon)} \frac{d[L(h\upsilon)]}{dx} \tag{4.1}$$

The momentum of a photon, is considered to be very small when compared to the crystal momentum, thus the photon-absorption process should conserve the momentum of the electron. The absorption coefficient of $\alpha(h\upsilon)$ for a given photon energy $h\upsilon$ is proportional to the probability P_{if} for the transition from the initial state to the final state and to the density of electrons in the initial state n_i, and also to the density of the available final states n_f. This process must be summed up for all possible transitions between the states separated by an energy difference equal to $h\upsilon$ [1]:

$$\alpha h(\upsilon) = A \sum P_{if} n_i n_f \tag{4.2}$$

For simplicity we may assume that all the states in the valence band are filled and that all the states in the conduction band are empty, which is true for ideal intrinsic semiconductors and insulators.

Allowed Direct Transitions
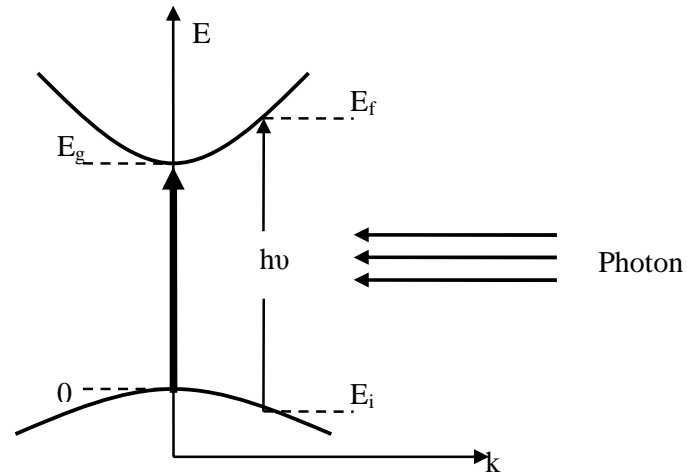
Figure 4.1: Energy-wave vector diagram for a direct band gap semiconductor material [2].

Let us consider the absorption process for a direct band gap semiconductor material through the allowed direct transitions in which all momentum conserving transitions are allowed as shown in figure 4.1. Each initial state at E_i is associated with a final state E_f such that:

$$E_f = h\upsilon - |E_i| \tag{4.3}$$

But in parabolic bands,

$$E_f - E_g = \frac{\hbar^2 k^2}{2m_e^*} \quad [\text{Kinetic energy of the electron with mass}\, m_e^*] \tag{4.4}$$

By substituting equation (4.3) into (4.4) and noting that $E_i = \dfrac{\hbar^2 k^2}{2m_e^*}$ (the kinetic energy

of the hole left behind), equation (4.4) becomes:

$$h\upsilon - E_g = \frac{\hbar^2 k^2}{2}\left(\frac{1}{m_e^*} + \frac{1}{m_h^*}\right) \tag{4.5}$$

The density of directly associated states is given by [1] as:

$$N(h\upsilon)d(h\upsilon) = \frac{8\pi k^2 dk}{(2\pi)^3} = \frac{(2m_r)^{3/2}}{2\pi^2 \hbar^3}(h\upsilon - E_g)^{1/2} d(h\upsilon) \tag{4.6}$$

where m_e^*, m_h^* are the effective mass of electron and hole respectively while m_r is

the reduced mass given by $1/m_r = 1/m_e^* + 1/m_h^*$ and $\hbar = h/2\pi$, the Dirac constant.

Thus the absorption coefficient for the allowed direct transitions is given by the result

of the integration of the joint density of states and the probability for the transition

from the initial state to the final state as:

$$\alpha(h\upsilon) = A^*(h\upsilon - E_g)^{1/2} \tag{4.7}$$

where A^* is a constant given by [3]:

$$A^* \approx \frac{q^2\left(2\dfrac{m_h^* m_e^*}{m_h^* + m_e^*}\right)^{3/2}}{nch^2 m_e^*} \tag{4.8}$$

In this situation, c is the velocity of light in vacuum and n is the refractive index of the semiconductor material.

Forbidden Direct Transitions

In some materials, quantum selection rules forbid direct transitions at position where k equals to zero but allows transitions at positions where k is not equal to zero. In this situation, the transition probability increases with k^2 and if we recall that the density of states linked in the direct transition is proportional to $(h\upsilon - E_g)^{1/2}$, equation 4.6, thus the absorption coefficient of the forbidden direct transition is given by [2]:

$$\alpha(h\upsilon) = A^{**}(h\upsilon - E_g)^{3/2} \tag{4.9}$$

where A^{**} is given by [3] as:

$$A^{**} = \frac{4}{3} \frac{q^2 \left(\dfrac{m_h^* m_e^*}{m_h^* + m_e^*} \right)^{5/2}}{nch^2 m_h^* m_e^* h\upsilon} \tag{4.10}$$

Indirect Transitions Between Indirect Valleys

For indirect band gap semiconductor materials, a transition requires a change in both the energy and momentum of the electron and as a result momentum is conserved through a phonon interaction as illustrated in figure 4.2. A phonon may be defined as a quantized mode of vibration occurring in a rigid crystal lattice [4]. A broad spectrum of phonons is available, however only the longitudinal and transverse

acoustic phonons are utilised during the transition process. Since these phonons are quantized, they posses a characteristic energy E_p which is either emitted or absorbed in order to complete the transition from E_i to E_f. The equations governing the phonons emission and absorption for an indirect transition are given by:
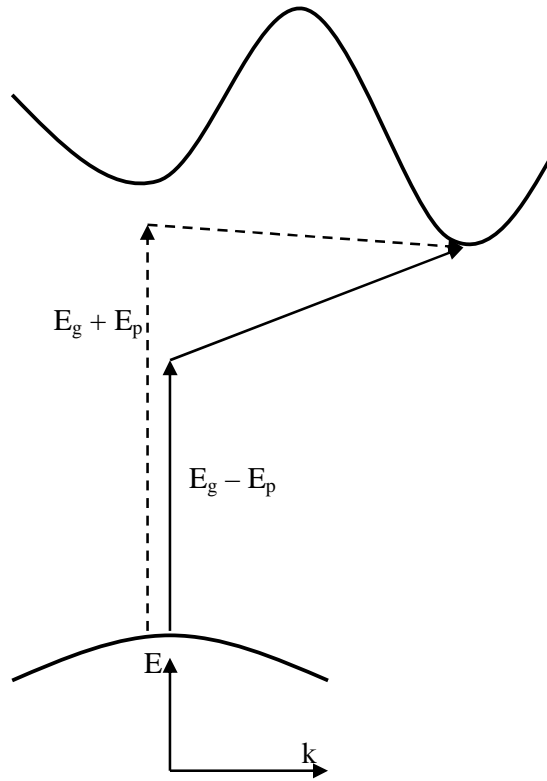
Figure 4.2: *Energy-wave vector diagram for an indirect band gap semiconductor material [2].*

$$h\upsilon_e = E_f - E_i + E_p \tag{4.11}$$

and

$$h\upsilon_a = E_f - E_i + E_p, \tag{4.12}$$

respectively. For indirect transitions, it is possible for all the occupied states of the valence band to connect to all the empty states in the conduction band. The density of the initial states E_i is given by [1]:

$$N(E_i) = \frac{1}{2\pi^2 \hbar^3} (2m_h^*)^{3/2} |E_i|^{1/2} \qquad (4.13)$$

and similarly the density of the final states E_f:

$$N(E_f) = \frac{1}{2\pi^2 \hbar^3} (2m_e^*)^{3/2} (E_f - E_g)^{1/2} \qquad (4.14)$$

By substituting the phonon equations of (4.11) and (4.12) into (4.14) results into:

$$N(E_f) = \frac{1}{2\pi^2 \hbar^3} (2m_e^*)^{3/2} (h\upsilon - E_g \pm E_p + E_i)^{1/2} \qquad (4.15)$$

The absorption coefficient is proportional to the product of the densities of the initial states given in equation (4.13) and final states given by (4.14) integrated over all possible combinations of states separated by $h\upsilon \pm E_p$ and also proportional to the probability of interacting with the phonons. The probability of finding a phonon is a function $f(N_p)$ of the phonon energy E_p, which is given by Bose-Einstein statistics [5]:

$$N_p = \frac{1}{\exp \dfrac{E_p}{\kappa T} - 1} \qquad (4.16)$$

where κ is Boltzmann's constant. Thus the absorption coefficient is given by:

$$\alpha(\text{h}\upsilon) = \text{Af}\left(\text{N}_p\right)\int_0^{-(\text{h}\upsilon - \text{Eg} \pm \text{Ep})}\left|\text{E}_i\right|^{1/2}\left(\text{h}\upsilon - \text{E}_g \pm \text{E}_p + \text{E}_i\right)^{1/2}d\text{E}_i \qquad (4.17)$$

By substituting equation (4.16) into the result of the integration of equation (4.17) yields the absorption coefficient for a transition with phonon absorption:

$$\alpha_a(\text{h}\upsilon) = \text{A}\frac{(\text{h}\upsilon - \text{E}_g + \text{E}_p)^2}{\exp\dfrac{\text{E}_p}{\kappa\text{T}} - 1} \qquad [\text{For h}\upsilon > \text{E}_g - \text{E}_p] \qquad (4.18)$$

On the other hand the probability of phonon emission is proportional to $\text{N}_p + 1$, thus the absorption coefficient for a transition with phonon emission is given by:

$$\alpha_e(\text{h}\upsilon) = \text{A}\frac{(\text{h}\upsilon - \text{E}_g + \text{E}_p)^2}{1 - \exp\left(-\dfrac{\text{E}_p}{\kappa\text{T}}\right)} \qquad [\text{For h}\upsilon > \text{E}_g + \text{E}_p] \qquad (4.19)$$

In the situation where $\text{h}\upsilon > \text{E}_g + \text{E}_p$, both phonon emission and absorption processes are possible, therefore the total absorption coefficient is given by the summation of the two processes:

$$\alpha_t(\text{h}\upsilon) = \alpha_a(\text{h}\upsilon) + \alpha_e(\text{h}\upsilon) \qquad (4.20)$$

Transitions Between Band and Impurity level

Figure 4.3 depicts some possible mechanisms involving transitions between a band and an impurity level. This includes a transition between a donor to the conduction band, and a transition between the acceptor level and the valence band or vice versa. In all these absorption processes, the energy of the photon must be equal to or greater than the ionization energy of the impurity.
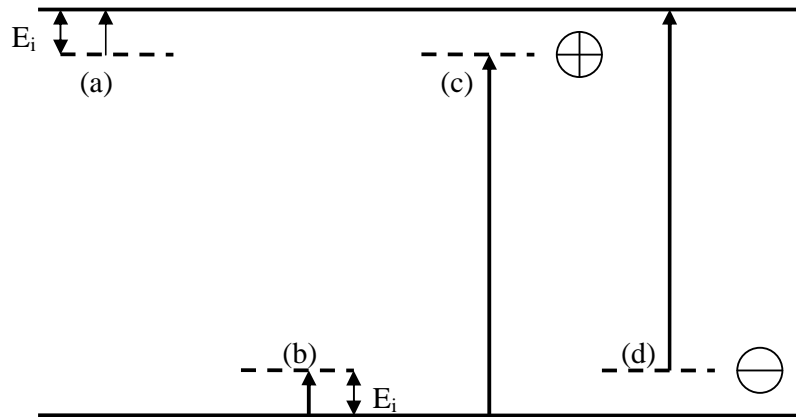
Figure 4.3: Absorption transitions between impurities and bands; (a): donor to conduction band, (b): valence band to acceptor, (c): valence band to donor and (d): acceptor to conduction band [1].

Exciton Absorption

Excitonic absorption can occur in both direct and indirect band gap materials (direct and indirect excitons) of sufficient high purity. In direct band gap materials, excitonic absorption usually appears as narrow peaks in the absorption spectrum while it appears as steps in indirect band gap material absorption spectra. The theory of excitonic absorption has been comprehensively dealt with by Elliot *et al.* [6]. This will be more examined in the luminescence section of this thesis.

4.2.2　　Photoluminescence

Luminescence may be defined as the emission of light by a material, after being subjected to a sufficient excitation. There are several ways of exciting materials. When the excitation of the material is performed by the application of an electric field, the process is called electroluminescence. On the other hand when electrons are
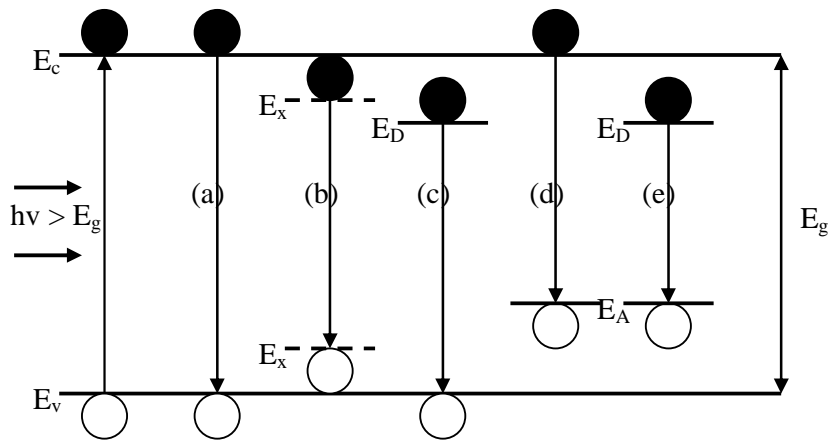
Figure 4.4: Radiative transitions in a semiconductor material; (a): Conduction to valence band, (b): excitonic recombination, (c): donor and valence band, (d): conduction band and (e): donor to acceptor.

used for the excitation, the process is known as cathodoluminescence. If the excitation is applied optically, then the process is called photoluminescence. During the photoluminescence process, photoexcitation causes electrons in the semiconductor material to move into permissible excited states. After a short while, the electrons return to their equilibrium states thereby recombining with holes, or by relaxation to a lower energy state, and liberating energy which may include light (radiative emission) or heat (non-radiative emission). The energy of the emitted light is related to the

difference in the energy levels between the excited state and the equilibrium state while the intensity of the emitted light is related to the relative contribution of the radiative process. In photoluminescence, the photo-excitation is usually implemented using a laser with a fixed wavelength and the emitted light is measured over a wavelength region. Figure 4.4 illustrates some of the common radiative recombination process that can occur in a semiconductor material.

According to the van Roosbroeck–Shockley equation [7] at equilibrium, the rate of optical generation of electron-hole pair is equal to the rate of radiative recombination. By making a detailed balance of these processes at various photon frequencies, we can write that the rate of emission, $R(\upsilon)$ at frequency υ in interval $d\upsilon$ is given by:

$$R(\upsilon)\ d\upsilon = P(\upsilon)\ \rho(\upsilon)\ d\upsilon \qquad\qquad (4.21)$$

where $P(\upsilon)$ is probability per unit time of absorbing a photon of energy $h\upsilon$, $\rho(\upsilon)$ is the density of photons of frequency υ in interval $d\upsilon$. The probability per unit time of absorbing a photon of energy $h\upsilon$ can be derived from Planck's radiation law [1]. For simplicity, if we assume that the refractive index n is independent of frequency υ, then:

$$\rho(\upsilon) = \frac{8\pi\upsilon^2 n^3}{c^3}\frac{1}{\exp\dfrac{h\upsilon}{\kappa T}-1}d\upsilon \qquad\qquad (4.22)$$

The relationship between the absorption probability $P(\upsilon)$ per unit time and the mean lifetime $\tau(\upsilon)$ for a semiconductor material is given by:

90

$$P(\upsilon) = \frac{1}{\tau(\upsilon)} \tag{4.23}$$

where the mean lifetime $\tau(\upsilon)$ can be deduced from the mean free path $1/\alpha(\upsilon)$ of a photon travelling at velocity u as:

$$\tau(\upsilon) = \frac{1}{\alpha(\upsilon)u} \qquad \text{[Assuming the refractive index is constant]} \quad (4.24)$$

Following from the above equations the absorption probability $P(\upsilon)$ can be written as:

$$P(\upsilon) = \alpha(\upsilon)u = \alpha(\upsilon)\frac{c}{n} \qquad \left[\because u = c/n\right] \tag{4.25}$$

By substituting equations (4.22) and (4.25) into (4.21) we get the fundamental relationship between the expected emission spectrum and the observed absorption spectrum:

$$R(\upsilon)d\upsilon = \frac{\alpha(\upsilon)8\pi\upsilon^2 n^2}{c^2\left[\exp(h\upsilon/\kappa T)\right]-1}d\upsilon \tag{4.26}$$

Band-to-Band Radiative Emission

Band-to-band radiative recombination can occur in both direct and indirect band gap materials. In direct band gap materials, momentum is conserved (see figure 4.1) and the corresponding emission spectrum is given by:

$$L(h\upsilon) = B(h\upsilon - E_g)^{1/2} \tag{4.27}$$

91

where B is a constant and could deduced from the analysis of Bardeen et al.[3] as:

$$B = \frac{2q^2 (m_r^*)^{3/2}}{n c h^2 m_e^*}$$

(4.28)

In indirect band gap materials, the transition requires a change in both the energy and momentum of the electron. As a result momentum is conserved through a phonon interaction as illustrated for the absorption process in figure 4.2. For this reason, the radiative efficiency of indirect band gap materials is inferior to that of direct band gap materials. The spectrum of the indirect band recombination material could be deduced in a similar fashion to that of the absorption process as:

$$L(h\upsilon) = B^* (h\upsilon - E_g + E_p)^2$$

(4.29)

where B^* is the transition probability of the indirect band gap material and it is believed to be much smaller than that of direct band gap materials [1].

Exciton Recombination

In photoluminescence experiments on high purity and quality semiconductor materials at low temperatures, it is expected that the photoexcited electrons and holes to be attracted by Coulombic interaction to form what is known as a free exciton. In direct band gap materials like GaN and CuCl, the free exciton states can adequately be described by the Wannier-Mott approximation [8,9]. In this situation, the electron and hole are separated by several inter-atomic spacings and the Coulombic interaction

results in a correlated motion of the electron-hole pair with a reduction of the total energy of the bound state relative to that of the free carrier states by an amount corresponding to the excitonic binding energy. In the effective mass approximation, the total energy of the two-particle system is given by [9]:

$$E_k = E_n + \frac{\hbar^2 k^2}{2\left(m_e^* + m_h^*\right)}$$

(4.30)

where E_n is given by

$$E_n = \frac{q^4 m_r}{2\left(4\pi\hbar\varepsilon_o\varepsilon_r\right)^2 n^2}$$

(4.31)

In this case, n is an integer and $\varepsilon_o\varepsilon_r$ is the permittivity. Equation (4.31) is a solution of the hydrogenic Schrödinger wave equation. This indicates that the free excitons can exist in a series of excited states similar to the excited states of hydrogen-like atomic systems. Due to the existence of excitons, optical transitions such as absorption or emission occur from discrete states slightly below the band gap E_g at the exciton energy [6,9,10]:

$$h\upsilon = E_g - \frac{E_x^b}{n^2}$$

(4.32)

where the energy required to ionize an exciton (binding energy), E_x^b is:

$$E_x^b = \frac{q^4 m_r}{2(4\pi\hbar\varepsilon_o\varepsilon_r)^2} \qquad (4.33)$$

Unlike most inorganic semiconductor materials, CuCl has a relatively large excitonic binding energy and the excitonic absorption/emission features are observable at room temperature and beyond since its excitonic binding energy is greater than κT at room temperature ($E_x^b \sim$ 190 meV $> \kappa T \sim$ 26meV). The valence band of CuCl is split into two bands by the spin orbit interaction, yielding Z_{12} and Z_3 free excitons.

A biexciton is made up of two free excitons, i.e. the combination of two free holes and two free electrons coupled by Coulombic interaction. Bound excitons may be formed in the presence of impurities (neutral or ionized) which can be associated with donors or acceptors in a semiconductor material. The recombination of the bound exciton is characterised by narrow band emission spectra at a lower photon energy than that of a free exciton, and thus the bound exciton can be easily distinguished from the free exciton. The bound excitons are usually prominent features in the luminescence of semiconductor materials and they collapse at higher temperatures due to their lower binding energy.

Bound exciton luminescence has been reported in several semiconductors including GaN [11], GaAs[12], InP[13], CdS [14], and CuCl [15]. Biexcitons has been reported in numerous semiconductor materials including ZnSe, CdS and ZnO [17,18]. In CuCl, a Cu vacancy has been suggested to be responsible for the excitonic bound luminescence in low temperature CuCl luminescence spectra [16].

4.3   Experimental

4.3.1   Film Deposition

The detailed procedure for substrates preparation and CuCl film deposition has be given in sections 2.2 and 2.7.5, so a brief recap of the process is given here. Thin films of CuCl were deposited on cleaned square cut soda lime glass, indium tin oxide (ITO) and silicon substrates using an Edwards's Auto 306 vacuum evaporator at a base pressure of the order of 1×10^{-6} mbar. The thickness of films was between $100 - 500$ nm at a constant growth rate of ~ 0.5 nms^{-1} as indicated by the thickness monitor.

Some of the deposited CuCl films were plasma treated using an Oxford Instruments Plasma Lab Plus 80 reactive ion etcher (RIE) in order to introduce oxygen atoms in the CuCl for the improvement of the electronic conductivity. Oxygen and argon mixtures were entered via dedicated channels at a ratio of 4:1 (O_2/Ar), the RF power was 300 W, while the chamber pressure was held at 50 mTorr. The duration of the plasma immersion was mainly for 1, 2, and 3 minutes for the different samples.

4.3.2   Characterisation Techniques

Room temperature absorption measurements were recorded on a Perkin Elmer Lamda 40 UV/VIS spectrometer for untreated CuCl/Glass, untreated CuCl/ITO plasma immersed samples. The measurements were calibrated by initially taking the spectra of the parental substrates (glass and ITO) and subtracting from the measured experimental spectra (CuCl/Glass and CuCl/ITO structures).

Temperature dependent photoluminescence measurements were carried out on untreated and plasma immersed CuCl/Si samples, from room temperature down to 10 K by employing a UV Ar ion Innova laser with a second harmonic generation BBO crystal producing a 244 nm photoexcitation. The photoluminescence spectra were collected on a Jobin Yvon-Horiba Triax 190 spectrometer with a spectral resolution of 0.3 nm, coupled with a liquid nitrogen cooled CCD detector. In order to investigate the photoluminescence properties of CuCl films deposited on glass and ITO and in order to compare to films that are deposited on silicon substrates, photoluminescence (PL) measurements were recorded over the temperature range 20 – 150 K, using the 325 nm line of a continuous wave HeCd laser with an intensity of $\sim$ 0.65 W/cm^2 for the untreated CuCl/Glass, CuCl/ITO and CuCl/Si structures. The emission from the samples in this case were analysed using a Bomem DA8 Fourier-Transform spectrometer fitted with a Hamamatsu R1913 photomultiplier tube.

4.4   Results

4.4.1   Absorption Spectroscopy of the As Deposited CuCl Films

Figure 4.5 shows the typical room temperature absorption spectrum of the polycrystalline cuprous chloride film deposited on glass. There was no difference between the spectrum of the film deposited on glass and that deposited on indium tin oxide (ITO) substrates. The room temperature absorption spectrum of figure 4.5 is dominated by the Z_{12} and the Z_3 free excitonic absorption features. These are as a result of the valence band being split into two bands by the spin orbit interactions of the $\Gamma_7(\Gamma_8)$ holes and Γ_6 electrons [19]. The room temperature values of 3.34 eV ($\lambda \sim$
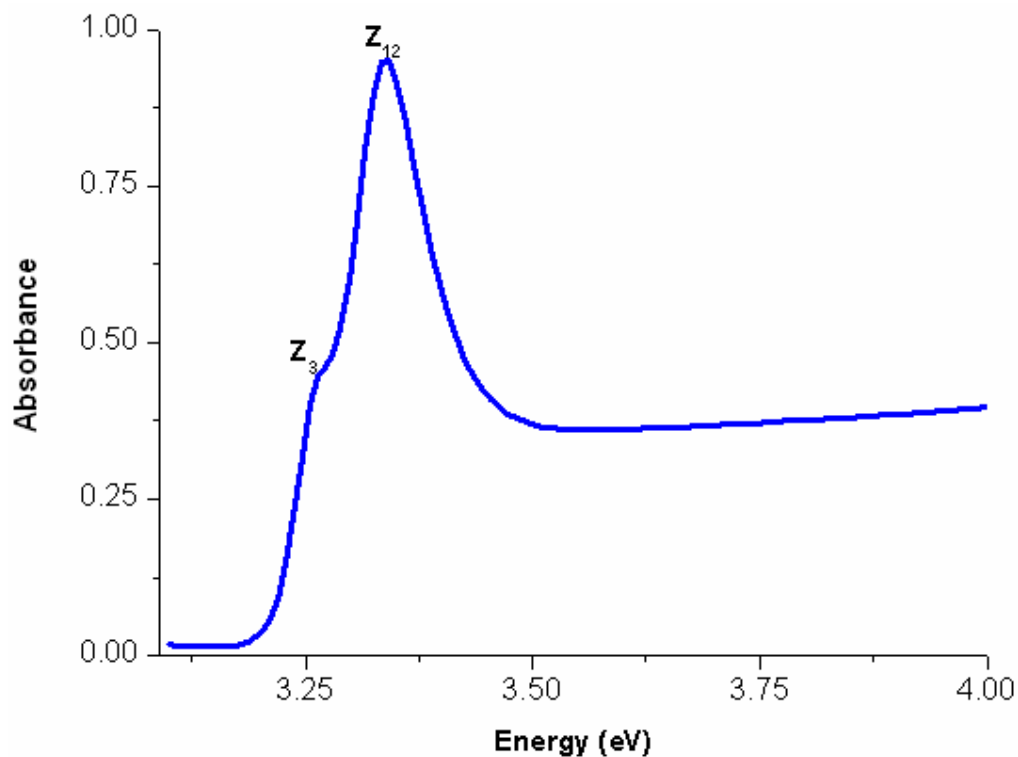
Figure 4.5: *A typical room temperature absorption spectrum of a 500 nm thick CuCl film.*

372 nm) for Z_{12} and 3.27 eV ($\lambda \sim 380$ nm) for Z_3 excitons are in agreement with the values previously reported in the literature [19,20].

4.4.2 Absorption Spectroscopy of the O$_2$ Plasma treated CuCl Films

In order to understand the effect of oxygen plasma immersion on the CuCl films, the absorption measurements were taken before and after each plasma treatment in a similar way to the XRD experiments described in section 3.4.2. The absorption spectra of cuprous chloride films were all identical to the untreated films for plasma immersions up to duration of 3 minutes.

For durations greater than 3 minutes, we have observed a reduction in the intensity of the excitonic peaks, indicating some sort of deterioration in the optical properties of cuprous chloride films. Figure 4.6 depicts the absorption spectra of CuCl films immersed plasma for durations of 3 minutes and 7 minutes. One can easily identify the Z_{12} and Z_3 excitonic absorption features in both films; however there is a reduction in the intensities of the excitonic peaks after a 7 minute plasma immersion.
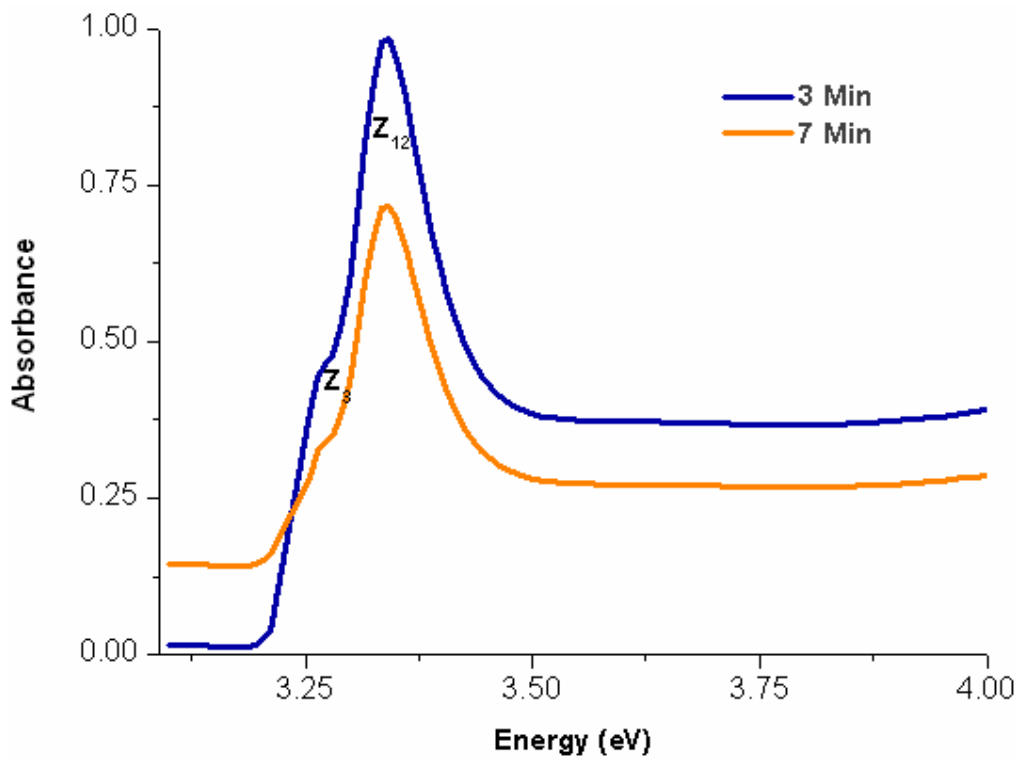
Figure 4.6: *Room temperature absorption spectra of CuCl films plasma immersed for 3 and 7 minutes.*

4.4.3 Photoluminescence Spectroscopy of the As Deposited CuCl Films

A typical low temperature photoluminescence spectrum at 10 K for the as deposited CuCl film on Si reveals four main peaks according to figure 4.7. The peak occurring

at ~ 3.203 ± 0.003 eV is the familiar Z_3 free exciton. The peak located at ~ 3.181±

0.003 eV is the I_1 impurity bound exciton, a Cu vacancy having been suggested to be

the impurity responsible for this emission [16]. The energy values of the Z_3 free

exciton and I_1 impurity bound exciton in this study are in excellent agreement with

previous bulk CuCl crystal measurements [21] and polycrystalline CuCl films

deposited on Al_2O_3 [22]. The peak occurring at ~ 3.160 ± 0.003 eV is ascribed to the

well known free biexciton M [23], which originates from exciton-exciton collisions.
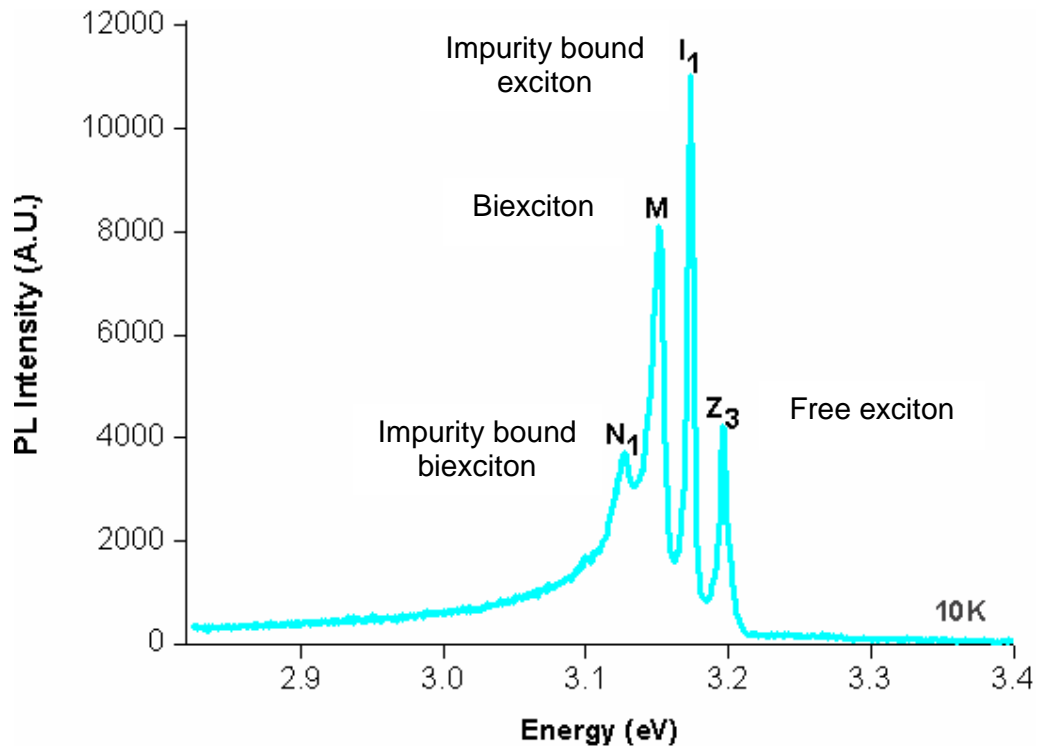
Figure 4.7: *PL spectrum of a 500 nm thick CuCl film deposited on Si substrate taken*
at 10 K.

Finally, the fourth peak centred at ~ 3.135 ± 0.003 eV is attributed to the N_1 impurity

bound biexciton. This emission originates from a biexciton bound to an impurity and

a neutral acceptor is believed to be the most probable impurity involved in the

emission process [22]. The value of ~ 3.135 ± 0.003 eV is close to previous measurements on bulk crystals [24].

The binding energies of the bound exciton (E_{bX}^b), the free bi-exciton (E_{XX}^b) and the bound bi-exciton (E_{bXX}^b) of the cuprous chloride films deposited on silicon substrates were calculated based on the experimental values of the four excitonic peaks obtained at 10 K using the following equations [22,25,26]:

$$E_{bX}^b = E_X - E_{bX} \tag{4.34}$$

$$E_{XX}^b = E_X - E_{XX} \tag{4.35}$$

$$E_{bXX}^b = 2E_X - E_{bXX} - E_{bX} - E_{XX}^b \tag{4.36}$$

where E_X (3.203 eV), E_{XX} (3.160 eV), E_{bX} (3.181 eV) and E_{bXX} (3.135 eV) are the values of the free exciton, bi-exciton, bound exciton and bound bi-exciton energies, respectively, taken from the PL spectrum at 10 K, as shown in figure 4.7. The binding energy of the bound bi-exciton was calculated using the corrected energy calculation scheme developed by Nakayama *et al.* [22]. Values of the order of 22 meV, 43 meV and 47 meV were deduced to be the binding energies of the bound exciton, free bi-exciton and the bound bi-exciton, respectively. The reported values of the bound exciton and bound bi-exciton in this work are in excellent agreement with earlier work on polycrystalline cuprous chloride films deposited on Al_2O_3 [22]. However the value of the binding energy of the free biexciton for the CuCl films deposited on Si

substrates was found to be about ~ 10 meV higher than those deposited on Al_2O_3. The calculated binding energies in the present work also agree well with the values reported for single crystal CuCl [27].

The temperature dependency of the PL spectra of CuCl/Si films is depicted in figure 4.8. The peak intensities of the impurity bound exciton I_1 and the impurity bound to biexciton N_1 decrease more rapidly in comparison to the free exciton Z_3 intensity as the temperature increases. At temperatures above 80 K up to room temperature, the
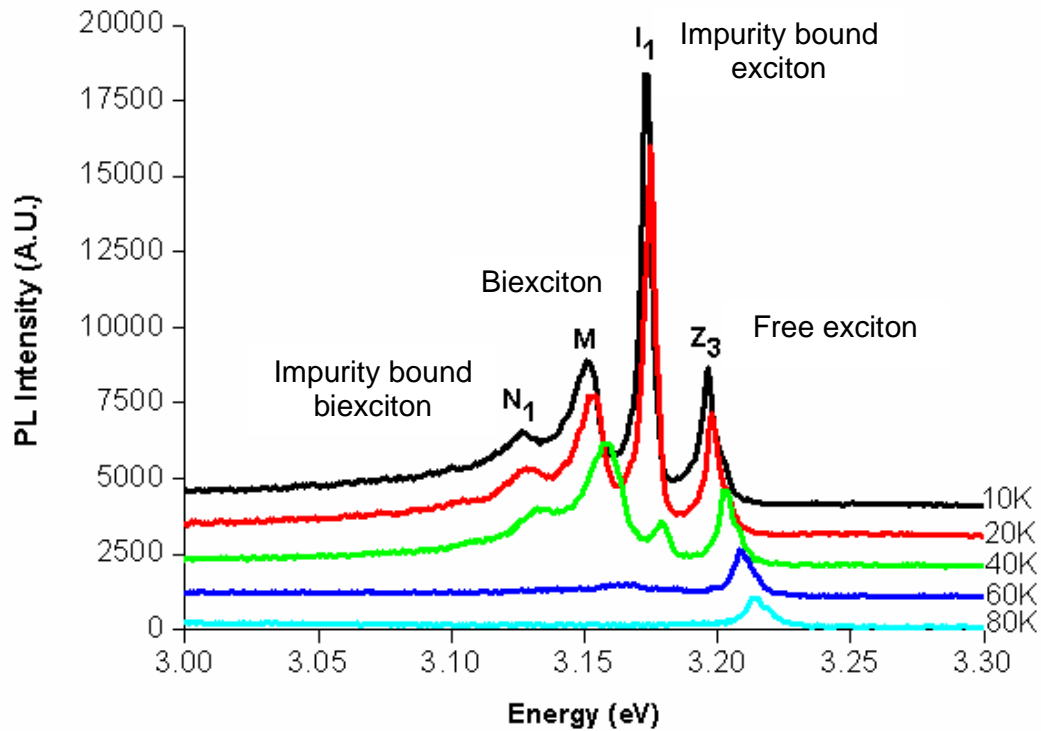
Figure 4.8: *Temperature dependence of the PL spectrum for the CuCl film shown in figure 4.7.*
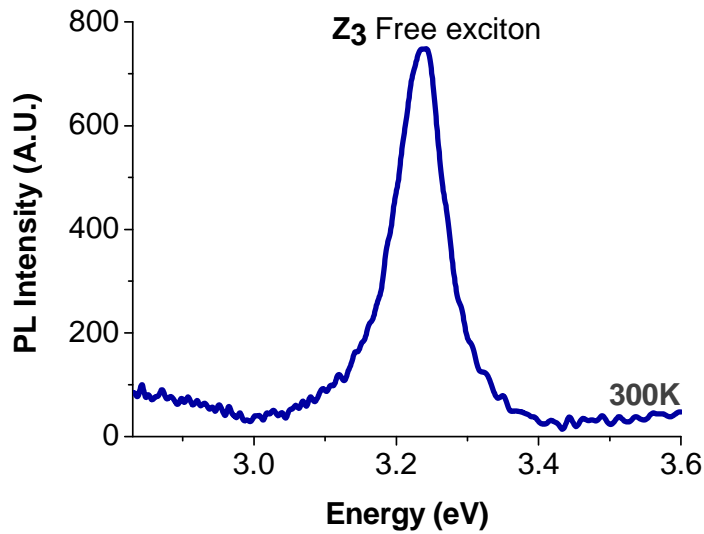
Figure 4.9: *Room temperature PL spectrum of the CuCl film shown in figure 4.7.*

spectra are dominated by the Z_3 free exciton peak. The dominance and the stability of the Z_3 excitonic peak even up to room temperature is due to its large excitonic binding energy of the order of 190 meV.

In our experiments, we did not observe broadband emission occurring at ~ 3 eV, ~ 2.75 eV, ~ 2.5 eV, ~ 2.3 eV, ~ 1.9 eV, ~ 1.77 eV and ~ 1.5 eV as previously reported by some authors for CuCl films and powders [28,29]. This indicates the optical quality of our as deposited CuCl films is most likely of considerably higher quality.

The temperature dependence of the Z_3 free exciton peak is seen in figures 4.8 and 4.9 as the peak energy increases from 3.203 eV at 10 K to 3.240 eV at room temperature, which in turn indicates an increase in the band gap as the CuCl film warms up. The increase of the band gap energy as a function of temperature, which is in contrast to most semiconductors that normally follow the Varshni or Einstein model [30,31], was

recently explained by Garro and co workers [32]. This anomalous effect is believed to be related to electron-phonon renormalization or coupling of the electronic structure of CuCl. They based their analysis on the fact that the Cu^+ ions vibrating predominantly at low frequencies lead to an increase in the band gap, whereas the Cl^- ions, vibrating at high frequencies lead to a reduction in the gap. The effect of the Cu^+ ions becomes dominant as the temperature increases, which in turn results in an increase of the band gap energy as a function of temperature. Similar results have been previously reported for both thin films and nanocrystals of CuCl [33, 34].

The PL measurements at 20 K using the 325 nm line of a continuous wave HeCd laser revealed three excitonic peaks: the bound bi-exciton, N_1; impurity bound exciton, I_1; and Z_3 free exciton, occurring at ~ 3.152, 3.181, and 3.204 eV, respectively, for all three structures (figure 4.10).
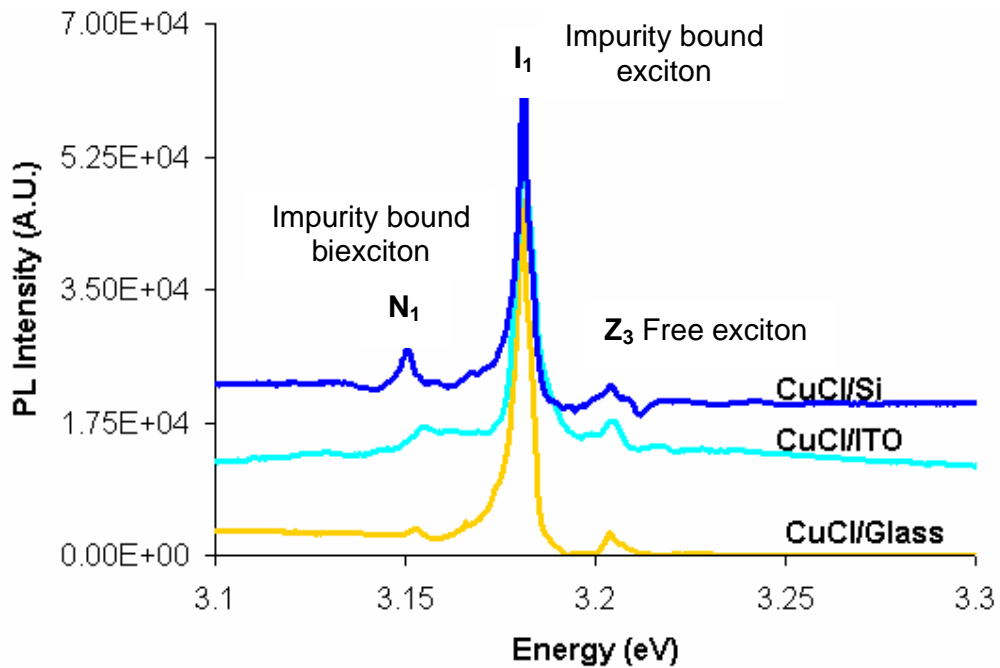
Figure 4.10: *PL spectrum of 500 nm thick CuCl films at 20 K.*

All three values of the peaks are in good agreement with results from the 244 nm excitation. The inability of this excitation to reveal four peaks as opposed to the 244 nm excitation is presumably due to a lower energy used in the excitation process. The temperature dependence of the PL spectra of the three structures was similar over the whole temperature range of 20 – 150 K. The N_1 peak disappears at temperatures below 20 K, as the intensity of I_1 decreases more rapidly in comparison to that of Z_3 as the temperature warms up. From 70 K to 150 K, all three spectra were dominated by the Z_3 free exciton.
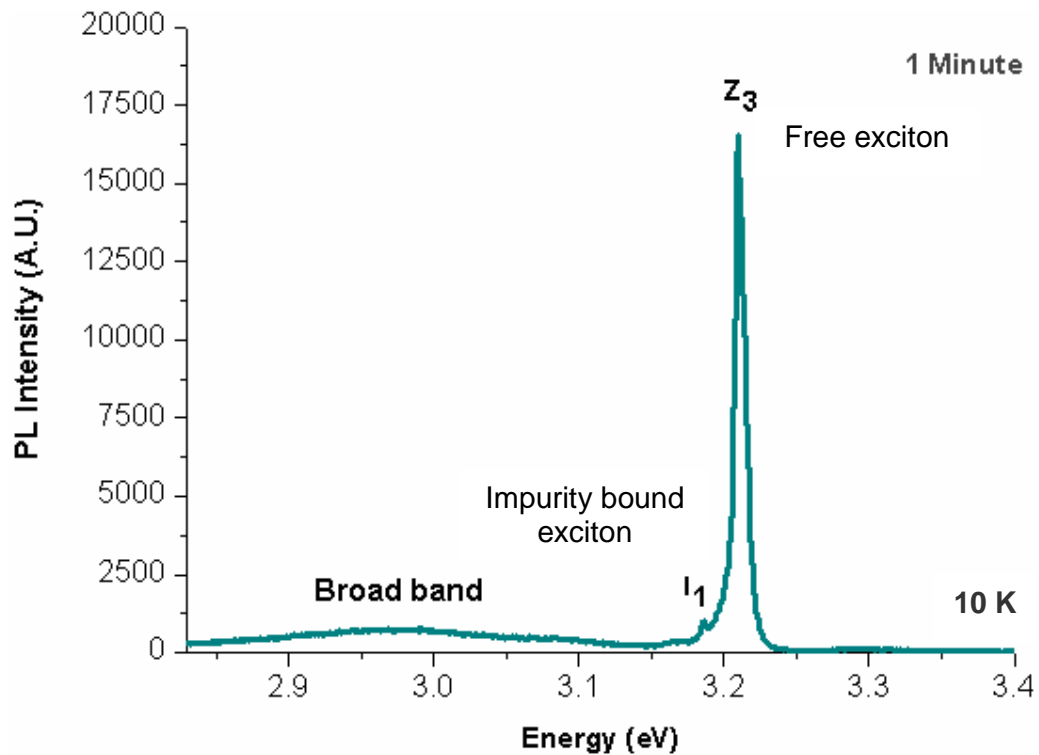
Figure 4.11: *10 K PL spectrum of CuCl/Si film plasma immersed for 1 minute.*

4.4.4   Photoluminescence Spectroscopy of O_2 Plasma Treated CuCl Films

The photoluminescence spectra of the CuCl films, which were plasma immersed for

up to 3 minutes are presented in figures 4.11 – 4.19. The introduction of an oxygen plasma to the CuCl films causes a slight shift of the excitonic peaks. At 10 K, the sample, which was plasma immersed for 1 minute reveals the Z_3 free excitonic peak occurring at 3.208 ± 0.003 eV, the I_1 impurity bound excitonic peak occurring at ~ 3.185 ± 0.003 eV and a small broad band emission occurring at ~ 3 eV (see figure 4.11). The disappearance of the two individual PL peaks as well as the presence of the broad band peak when compared to the untreated film is ascribed to the presence of oxygen, since it is believed that excitons are usually present in highly purified materials.
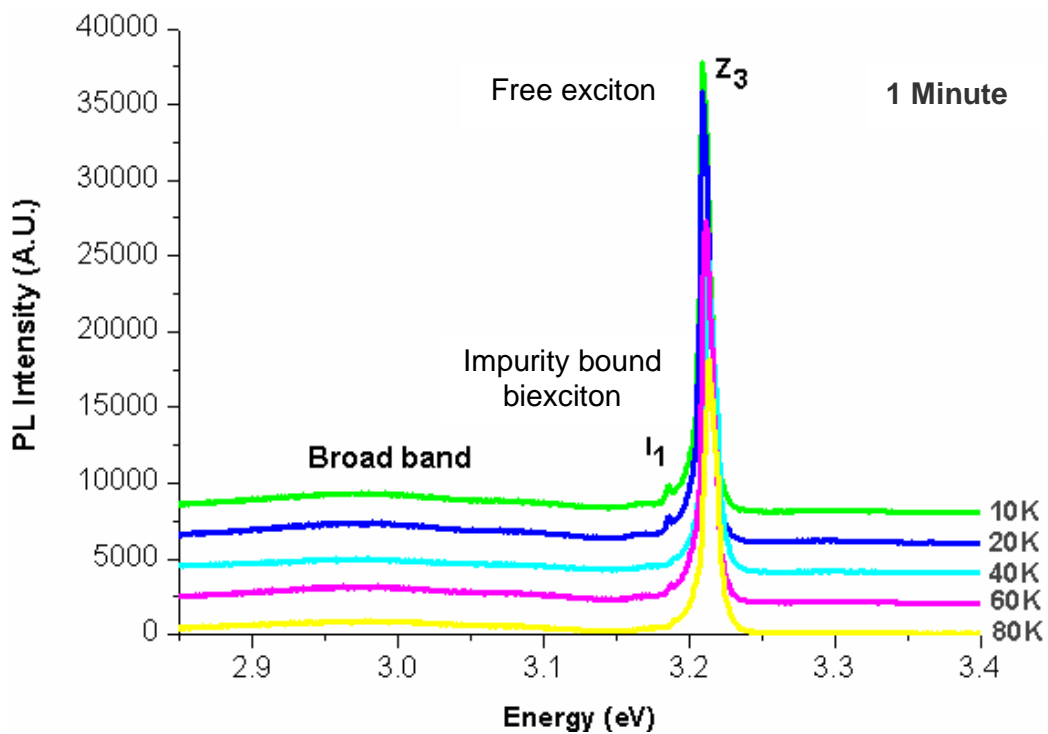
Figure 4.12: *Temperature dependence of the PL spectrum of the CuCl film shown in figure 4.11.*

The binding energy of the bound exciton (E_{bX}^{b}) was deduced to be about 23 meV, using equation 4.34. In this case E_X = 3.208 eV and E_{bX} = 3.185 eV. The value of the calculated binding energy of the bound exciton is in good agreement with the untreated films.

The temperature dependence of the PL spectra for the CuCl films which were plasma immersed for 1 minute is depicted in figure 4.12. The peak intensities of the impurity bound exciton I_1 and the broadband peak decreases more rapidly in comparison to the free exciton Z_3 as the temperature increases. At 80 K the impurity bound exciton I_1 disappears, while the spectra were dominated by the Z_3 free exciton peak.
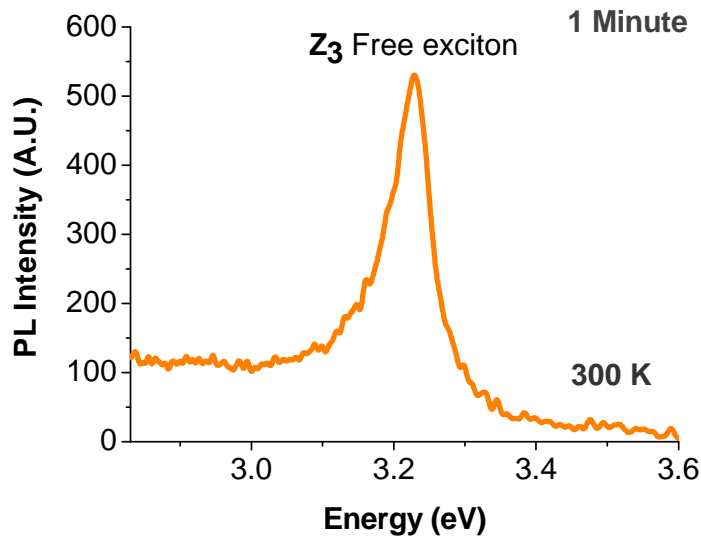
Figure 4.13: *Room temperature PL spectrum of the CuCl film shown in figure 4.11.*

On the other hand at 140 K the broad band emission disappears and the spectra were fully dominated by the Z_3 free exciton peak up to room temperature. The dominance and the stability of the Z_3 excitonic peak even up to room temperature is due to its large excitonic binding energy of the order of 190 meV as earlier indicated.

The temperature dependence of the Z_3 free exciton peak is seen in figures 4.12 and 4.13 as the peak energy increases from 3.208 eV at 10 K to 3.236 eV at room temperature, which in turn indicates an increase in the band gap as the CuCl film warms up. The increase of the band gap energy as a function of temperature is in line with the untreated films. However the anomalous behaviour in this case is slightly less temperature dependent, since there was only a change in the band gap energy of ~ 28 meV from 10 K to 300 K as compared to ~ 37 meV for the untreated films. Based on Garro and co-workers, analysis of electron-phonon renormalization of the electronic structure of CuCl, the presence of oxygen in copper chloride films slightly
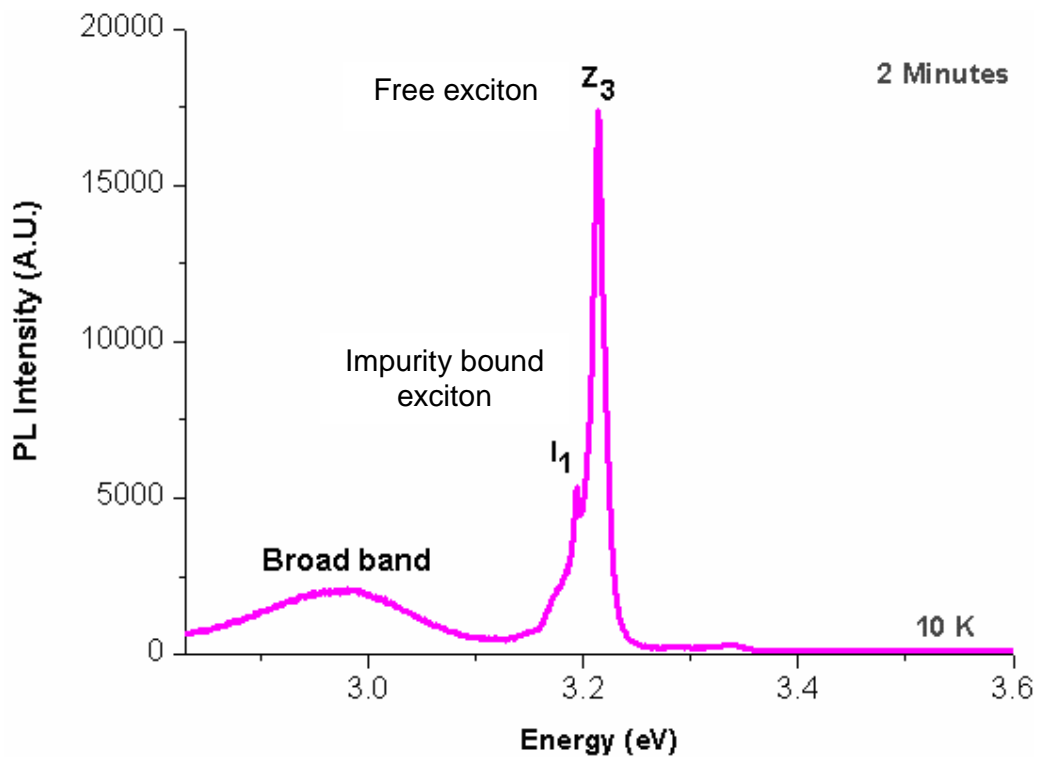
Figure 4.14: *10 K PL spectrum of CuCl/Si film plasma immersed for 2 minute.*

reduces the dominance of Cu^+ ions vibrating predominantly at low frequencies, thereby reducing the effect of the increase in the band gap with temperature.

The CuCl film, which were plasma immersed for 2 minutes, behaved very similar to the 1 minute plasma treated samples, revealing the Z_3 free excitonic peak occurring at 3.213 ± 0.003 eV, the I_1 impurity bound excitonic peak occurring at $\sim 3.190 \pm 0.003$ eV and broad band emission at ~ 3 eV at 10 K (see figure 4.14). The excitonic peaks in the 2 minute plasma-treated film are shifted to a higher energy value, and the broad band emission is more intense than for the 1 minute plasma treated film.
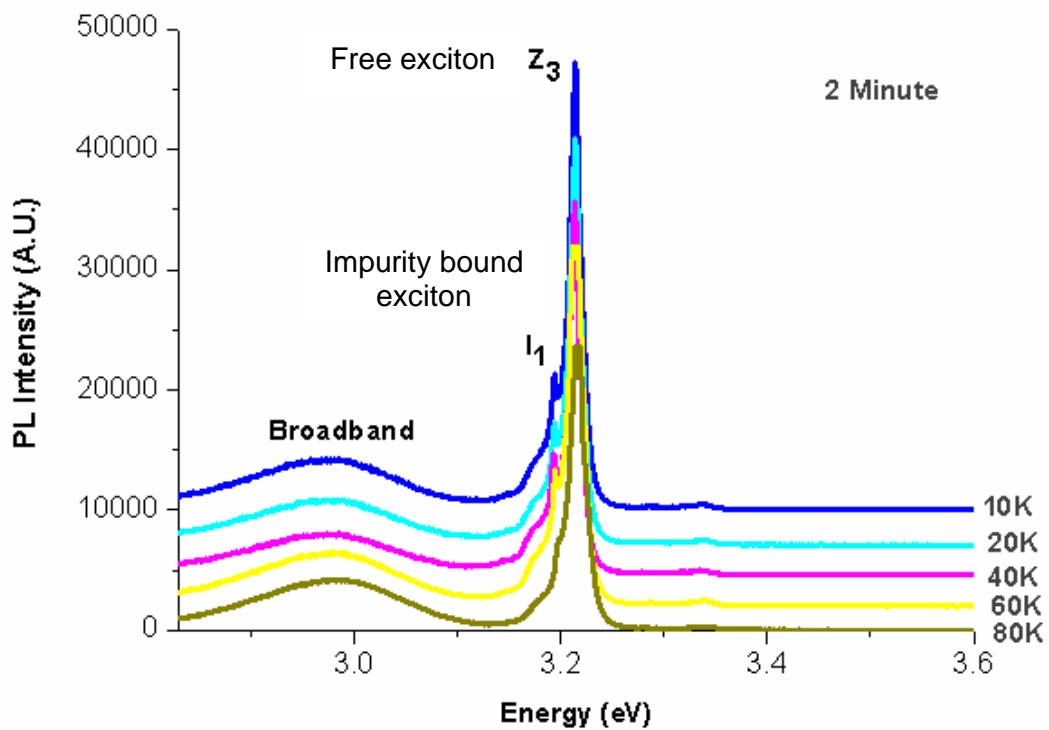
Figure 4.15: *Temperature dependence of the PL spectrum for the CuCl film shown in figure 4.14.*
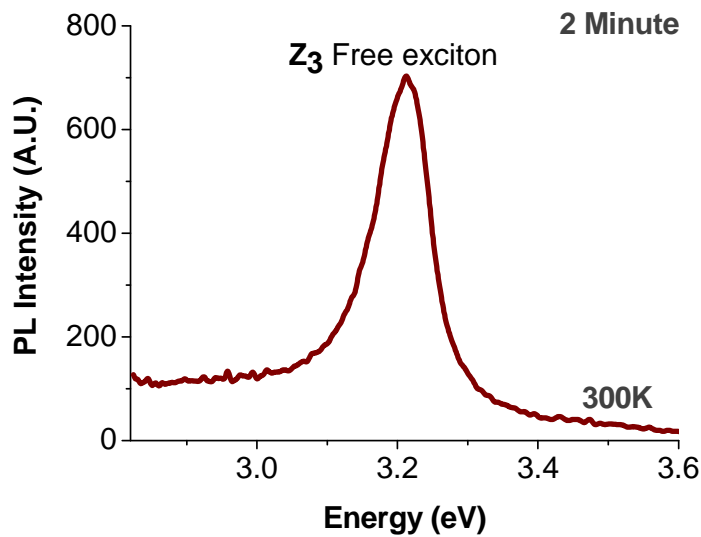
Figure 4.16: *Room temperature PL spectrum of the CuCl film shown in figure 4.14.*

This further confirms that oxygen is responsible for the shift in the energy level and the broad band emission around ~ 3 eV. The binding energy of the bound exciton (E_{bX}^{b}) was calculated to be about 23 meV, using equation 4.34. In this case E_X = 3.213 eV and E_{bX} = 3.190 eV. The calculated binding energy of the bound exciton is also in good agreement with the untreated films.

The temperature dependence of the PL spectra of the 2 minute plasma-treated films follow almost the same trend as per the 1 minute plasma-treated films (figure 4.15). The peak intensities of the impurity bound exciton I_1 and the broad band peak decrease more rapidly in comparison to the free exciton Z_3 as the temperature increases. At 80 K the impurity bound exciton I_1 disappears, while the spectra were again dominated by the Z_3 free exciton peak. At around 140 K the broad band disappears and the spectra were fully dominated by the Z_3 free exciton peak up to room temperature.

The temperature dependence of the Z_3 free exciton peak for the 2 minutes plasma-treated films is seen in figures 4.15 and 4.16 as the peak energy increases from 3.213 eV at 10 K to 3.233 eV at room temperature. The anomalous band gap behaviour in this case is slightly less temperature dependent than the 1 minute-plasma treated films, since only a change in band gap energy of ~ 20 meV from 10 K to 300 K was measured as compared to ~ 28 meV for the 1 minute plasma-treated films. The reduction in the change of the band gap of the film as a function of temperature is again ascribed to the effect of oxygen as previously explained.
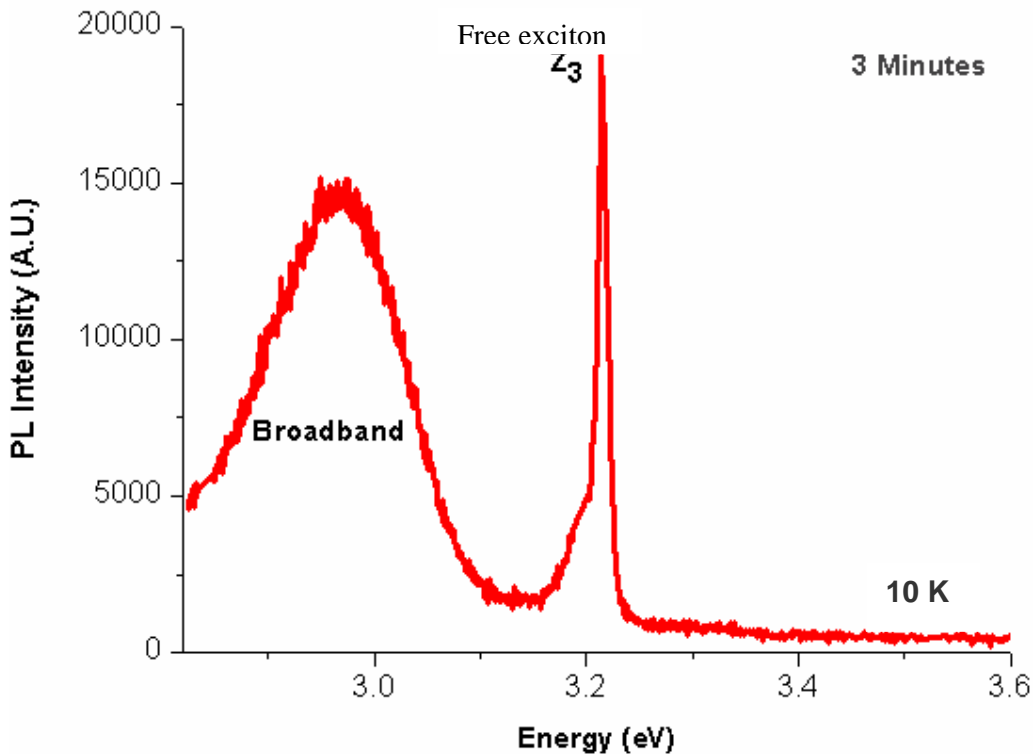
Figure 4.17: *PL spectra of 3 minutes plasma treated CuCl film at 10 K.*

At 10 K, the 3 minute plasma-treated CuCl films showed only revealed the Z_3 free excitonic peak occurring at 3.220 ± 0.003 eV and a much stronger broad band emission occurring at ~ 3 eV (see figure 4.17). The absence of the I_1 impurity bound

excitonic peak in the spectra may also be ascribed to the effect of oxygen plasma damage/alteration of the CuCl films as a result of the longer plasma treatment.

The temperature dependency of the PL spectra for the 3 minutes plasma treated films is depicted in figure 4.18. The peak intensity of the broad band decreases more rapidly in comparison to the free exciton Z_3 as the temperature increases. In the a similar manner to the 1 and 2 minute plasma-treated films, at around 140 K the broad band emission disappears and the spectra were fully dominated by the Z_3 free exciton peak up to room temperature.
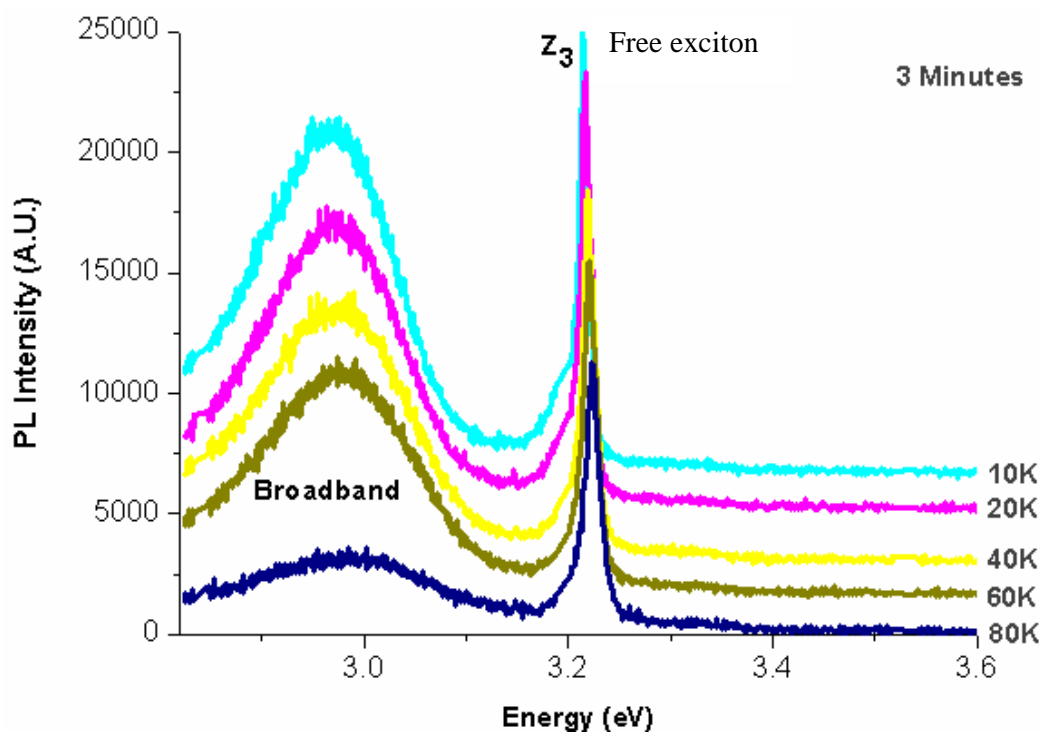
Figure 4.18: *Temperature dependence of the PL spectrum of the CuCl film shown in figure 4.17.*
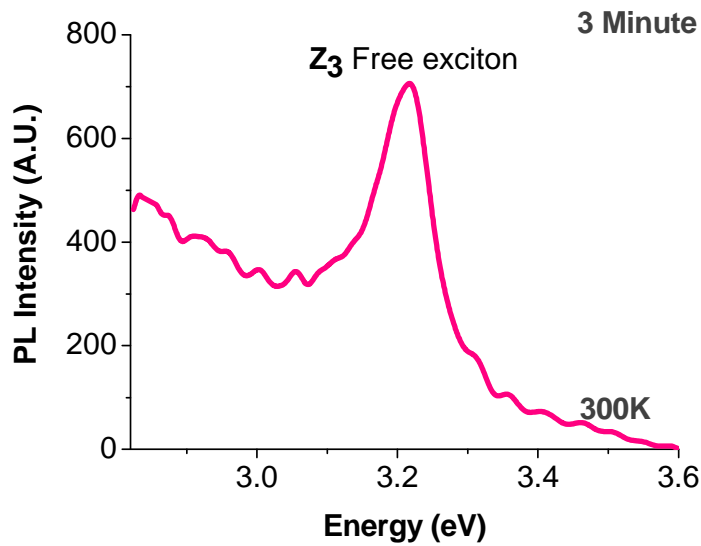
Figure 4.19: *Room temperature PL spectra of the CuCl film shown in figure 4.17.*

The temperature dependence of the Z_3 free exciton in this case increases from 3.22 eV at 10 K to 3.230 eV at room temperature. Again the anomalous temperature dependency of the band gap of the 3 minute plasma-treated films is more temperature independent than the earlier films, with only a change in band gap energy of ~ 10 meV from 10 K to 300 K.

By comparing the optical properties of the plasma treated films with the untreated films, one can easily see from table 4.1 that the optical properties of the plasma treated samples change monotonically with an increase in plasma immersion time. The FWHM of the Z_3 exciton PL of 88 meV deduced for the 1 minute plasma-treated films at room temperature is comparable to a value of 87 meV calculated for untreated films at room temperature. This indicates that the room temperature optical quality of CuCl film is almost the same as the untreated CuCl films.

O$_2$ Plasma Immersion Time (Mins)	**0**	**1**	**2**	**3**
Absorption (300 K)				
Z$_{12}$ (eV)	3.34	3.34	3.34	3.34
Z$_3$ (eV)	3.27	3.27	3.27	3.27
PL (10 K)				
Z$_3$ (eV)	3.20	3.21	3.21	3.22
I$_1$ (eV)	3.18	3.19	3.19	
M (eV)	3.16			
N$_1$ (eV)	3.14			
PL (300 K)				
Z$_3$ (eV)	3.24	3.24	3.23	3.23
Change in Bandgap From 10K to 300K (meV)	~ 37	~ 28	~ 20	~ 10
FWHM of Z$_3$ PL Peak @ 300 K (meV)	87	89	96	125

Table 4.1: Some optical properties of both the as deposited and plasma immersed CuCl films. For comparison the PL data is approximated only to 2 decimal places.

4.5   Conclusion

In summary, the optical properties of γ-cuprous chloride films deposited on glass, ITO coated on glass and silicon substrates have been investigated. Some of samples deposited on silicon and ITO substrates were O$_2$ plasma immersed and examined as well:

- Room temperature absorption spectra reveal the Z$_{12}$ and the Z$_3$ free excitonic absorption features, occurring at 3.34 eV and 3.27 eV, respectively, for both

untreated and plasma immersed films. However we have observed a reduction in the intensity of the excitonic peak intensities for films plasma treated for durations greater than 3 minutes. This suggests some sort of deterioration in the optical properties of cuprous chloride films.

- The 10 K PL spectrum of CuCl/Si using 244 nm excitation reveals the Z_3 free exciton occurring at 3.203 eV, the I_1 impurity bound exciton located at 3.181 eV, the M free biexciton occurring at 3.160 eV and N_1 impurity bound bi-exciton located at 3.135 eV. However, the 20 K PL spectra for the three structures using the 325 nm excitation revealed only the Z_3 free exciton, the I_1 impurity bound exciton and the N_1 impurity bound to biexciton at 3.204 eV, 3.18 eV and 3.152 eV respectively, for all three structures. The room temperature PL spectra of the films were dominated by the Z_3 free exciton. The temperature dependence of the band gap showed an increase of ~ 37 meV from 10 K to room temperature. This anomalous effect is believed to be related to electron-phonon renormalization or coupling of the electronic structure of the CuCl band gap as the temperature increases, which is opposite to most conventional semiconductor materials.

- For PL measurements at 10 K, the 1 minute and 2 minute plasma-treated samples reveal both the Z_3 free exciton, the I_1 impurity bound exciton, while the samples treated for 3 minutes only reveals the Z_3 free exciton. In addition a broad band emission ascribed to an oxygen related emission process is observed at ~ 3 eV between 10 and 140 K for all the plasma treated films. From 140 K to room temperature, the spectra of all the samples were dominated by the Z_3 free exciton. The optical quality of the plasma treated samples deteriorates with an increase in the plasma immersion duration.

- The band gap of all the plasma treated films follow the same anomalous temperature dependence in a similar manner to the untreated films, however the plasma treated films were less sensitive to temperature. A band gap change of as little as ~ 10 meV was observed for the 3 minute plasma-treated films from 10 K to room temperature.

References

[1]   J.I. Pankove, *Optical Processes in Semiconductors,* Dover Publication Inc: New York, (1971)

[2]   S.M. Sze, *Semiconductor Devices: Physics and Technology,* John Wiley & Sons Inc: New York, (2002)

[3]   J. Bardeen, F.J. Blatt and L.H. Hall, *Proceeding of Atlantic City Photoconductivity Conference*, (1954)

[4]   C. Kittel, *Introduction to Solid State Physics,* Wiley Publishing Inc (2004)

[5]   W. Wang, *Solid State Electronics,* McGraw-Hill (1966)

[6]   R.J. Elliot, *Physical Review* **108** (1957) 1384

[7]   W. van Roosbroeck and Shockley, *Physical Review* **94** (1954) 1558

[8]   A.A. Cofolla, S.E. Schnatterly and C. Tarrio, *Physical Review Letters* **55** (1985) 2818

[9]   E.I. Rashba and M.D. Sruge, *Excitons*, North-Holland Publishing Company: Amsterdam (1982)

[10]   A.L. Ivanov, H. Haug and L.V. Keldysh, *Physics Reports* **296** (1998) 237

[11]   B. Monemar, *Physical Review B* **10** (1974) 676

[12]   M.A. Gilleo, P.T. Bailey and D.E. Hill, *Physical Review* **174** (1968) 898

[13]   W.J. Turner and G.D. Pettit, *Applied Physics Letters* **3** (1963) 102

[14]   D.G. Thomas and J.J. Hopfield, *Journal of Applied Physics* **33** (1962) 3234

[15]   F.O. Lucas et al. *Journal of Physics D: Applied Physics* **40** (2007) 3461

[16]   M. Certier, C. Wecker and S. Nikitine, *Journal of Physics and Chemistry of Solids* **30** (1969) 2135

[17]   V. Kutzer, B. Lummer, R. Heitz, A. Hoffmann, I. Broser, *Journal of Crystal Growth* **159** (1996) 776

[18]   A. Yamamoto, K. Miyajima, T. Goto, H.J. Ko and T. Yao, *Physica Status Solidi B* **229** (2002) 871

[19]   A. Goldmann, *Physica Status Solidi* **B 81** (1997) 9

[20]   G. Suyal, M. Mening and H. Schmidt, *Journal of Materials chemistry* **10** (2002) 3136

[21]   T. Goto, T. Takahashi, and M. Ueta, *Journal of the Physical Society of Japan* **24** (1968) 314

[22]   M. Nakayama, H. Ichida and H. Nishimura, *Journal of Physics: Condensed Matter* **11** (1999) 7653

[23]   N. Nagasawa, N. Nakata, Y. Doi, and M. Ueta, *Journal of the Physical Society of Japan* **39** (1975) 987

[24]   H. Souma, T. Goto, T. Ohta and M. Ueta *Journal of the Physical Society of Japan* **29** (1970) 697

[25]   S. Yano, T. Goto, T. Itoh and A. Kasuya, *Physical Review B* **55** (1997) 1667

[26]   Y. Masumoto, T. Kawamura and K. Era, *Applied Physics Letters* **62** (1993) 225

[27]   Y. Masumoto, S. Okamoto and S. Katayangi, *Physical Review B* **50** (1994) 18658

[28]   M. Ueta, T. Gono, *Journal of the Physical Society of Japan* **20** (1965) 401

[29]   T.V. Zakharova and N.A. Zakhrov *Inorganic Materials* **38** (2002) 834

[30]   Y. P. Varshni, *Physica* **34** (1967) 149

[31]   X.T. Zhang, Y.C. Liu, Z.Z. Zhi, J. Y. Zhang, Y. M. Lu, D.Z. Shen, W. Xu, X.W. Fan and X.G. Kong, *Journal of Luminescence* **99** (2002) 149

[32] N. Garro, A. Cantarero, M. Cardona, T. Ruf, A. Göbel, C. Lin, K. Reimann, S. Rtibenacke and M. Steube, *Solid State Communications* **98** (1996) 27

[33] A. Göbel, T. Ruf, M. Cardona, C.T. Lin, J. Wrzesinski, M. Steube, K. Reimann, J-C Merle and M. Joucla, *Physical Review B* **57** (1998)15183

[34] O. Pagés, H. Erguig, A. Lazreg, A. Katty, A. Lusson and O. Gorochov, *Materials Science and Engineering B* **69–70** (2000)431

5

Electrical Properties

5.1 Introduction

Electrical characterization techniques are vital in the characterisation of semiconductor materials and devices. They reveal various properties including transport, defect and dielectric properties of semiconductor materials and devices. In this chapter we briefly review the basics of ionic and electronic conduction in solids. We also report on the results of the AC and DC electrical characterization of γ-CuCl films.

5.2 Literature Review

5.2.1 Ionic Conduction in Solids

Ionic conduction is caused by the movement of negatively (anions) or positively (cations) charged ions which hop from lattice site to lattice site under the influence of an electric field. According to the ideas developed mainly by Frenkel [1], Wagner and Schottky [2], and Jost [3], there are a number of lattice points in a crystal from each of which the corresponding atom or ion is missing. In addition to this, there are a number of ions in ionic crystals, or atoms in metals, which will be situated in what they

termed as "interlattice" (interstitial) positions. In general, the presence of imperfections results in ionic conduction in polar crystals. The various kinds of point imperfections possible in an ionic crystal MX, (where M and X are the monovalent metal and non-metal constituents of the ionic compound, respectively, e.g. CuCl) taking into account the requirement of charge neutrality are as follows [4]:

(1) *Vacancies:* The schematic representation of vacancies is illustrated in figure 5.1. A cation vacancy is depicted as V'_M and it occurs when metal ion M^+ is missing from its normal position. An anion vacancy is formed in a similar fashion and it is usually represented by V'_X.

(2) *Interstitials:* This type of defect occurs, if in a volume element of lattice, an atom is missing (or contains an excess atom) with respect to the ideal lattice as shown in figure 5.2. Any such defect is expected to cause a certain distortion of the lattice in the neighbourhood. Interstitials are denoted by M_i° and X'_I for cation and anion interstitials respectively.

(3) *Misplaced atoms:* An atom M occupying a normal X site or vice versa.

(4) *Schottky defect:* This type of defect is formed when an anion as well as a cation of the same absolute valency is missing in the crystal. In order words, Schottky defects contain a combination of a cation, an anion and vacancies ($V'_M V_i^\circ$) and it has been predominantly found in alkali halides.

(5) *Frenkel defect:* In this case, an atom or ion in a crystal leaves its normal position and travels to an interstitial position as illustrated in figure 5.3. Thus the Frenkel defect is a combination of a vacancy and an interstitial cation ($V'_M M_i^\circ$) and has been found in silver halide materials. On the other hand an anti-Frenkel defect comprises of an anion vacancy and an interstitial anion ($V^\circ_X X'_i$) and has been found in CaF_2.

(6) *Impurities:* This type of defect occurs when an impurity is introduced into the crystal. It may be situated either on an interstitial site or a normal site (substitutional impurity) as shown in figure 5.4.
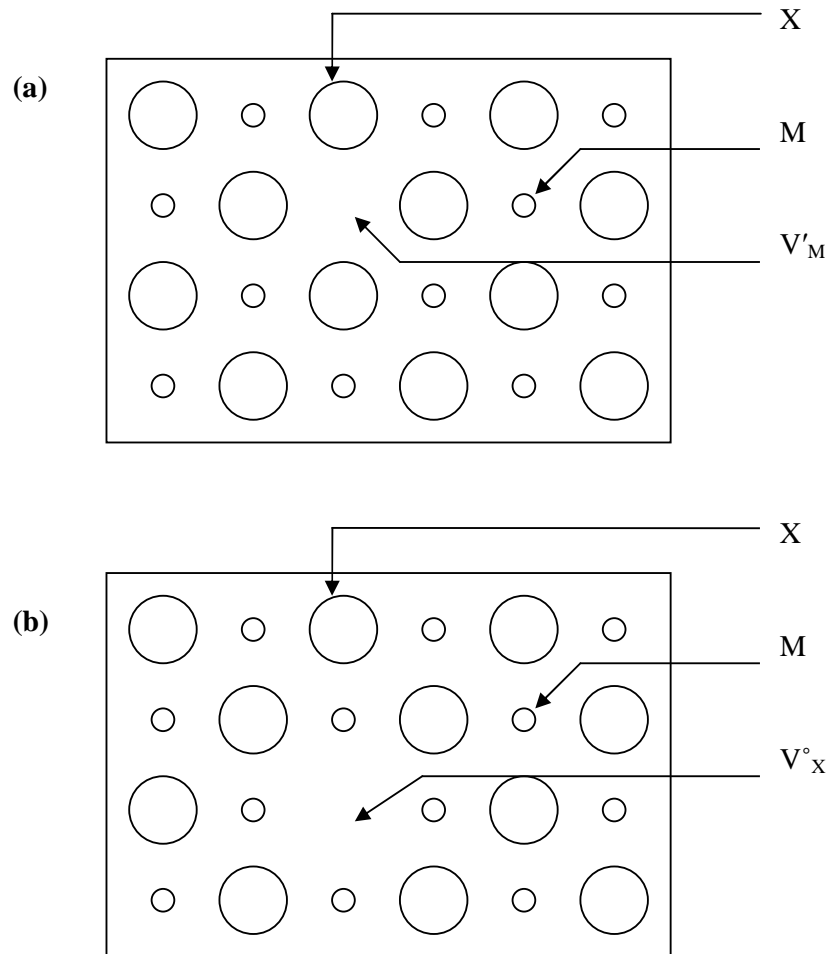

Figure 5.1: *Schematic representation of vacancies in an ionic crystal MX; (a): Cation vacancy* V'_M, (b): *Anion vacancy* V°_X *[4]. The combination of a cation and an anion vacancy results in a Schottky defect* [$V'_M V^{\circ}_X$]*.
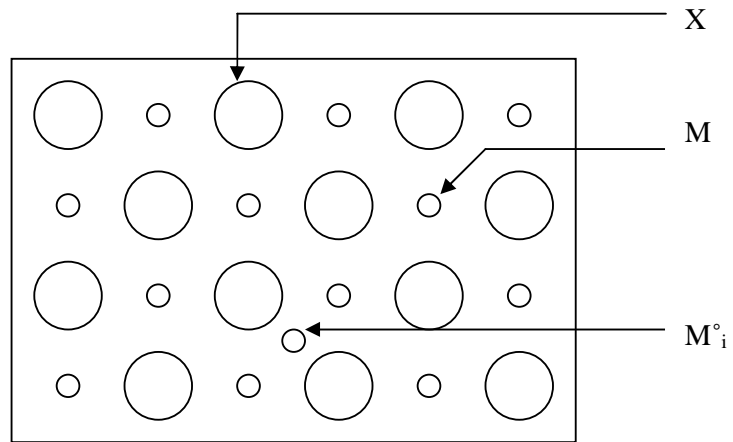
Figure 5.2: *Schematic representation of a cation interstitial* M_i° *in an ionic crystal MX [4].*
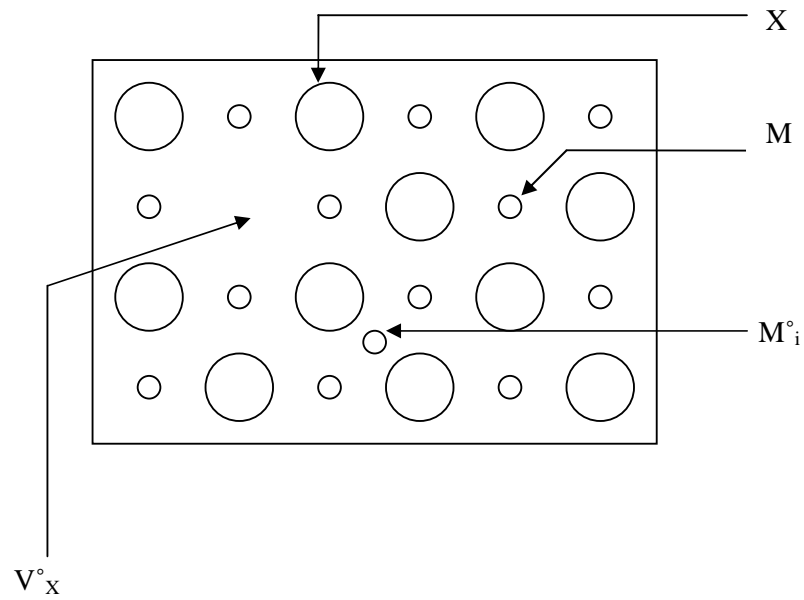
Figure 5.3: *Schematic representation of a Frenkel defect in an ionic crystal MX [4].*
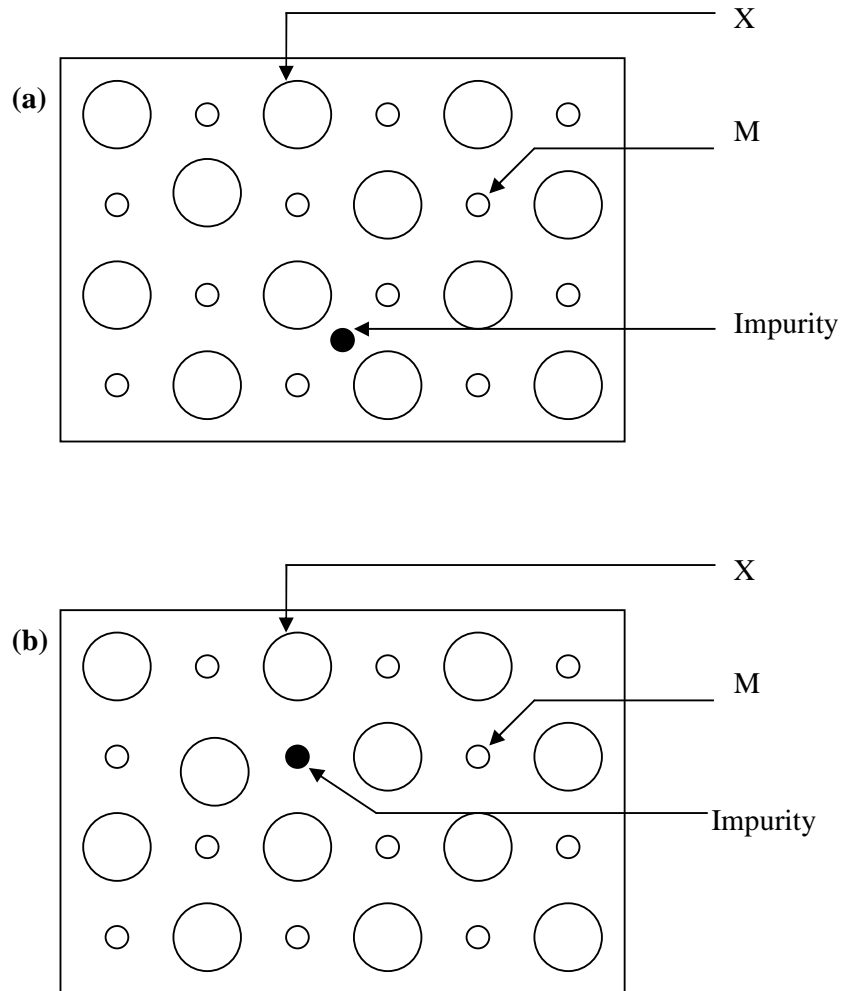
Figure 5.4: *Schematic representation of an impurity defect in an ionic crystal MX;*

(a): interstitial impurity, (b): substitutional impurity [4].

A summary of the types of defects established in different ionic crystals is given in table 1.1. In general, a defect type based on interstitial anions is less likely than its cation counterpart, due to the relatively closer packing of anions in most ionic solids.

Type of Substance and Examples	Structure	Defect structure and Transport Mechanism
Alkali Halides LiF, NaCl, KI etc.	fcc	Schottky defects. Cation vacancies more mobile
Cesium halides CsI, TICl, etc.	CsCl	Schottky defects. Anion vacancies more mobile
Silver halides AgCl, AgBr, etc.	NaCl fcc	Cation Frenkel defects. Cation motion by both vacancy and insterstialcy
Alkaline earth halides CaF_2, $SrCl_2$ etc.	Fluorite & others	Anion Frenkel defect. Anion vacancy and interstitial both mobile
Other halide $PbBr_2$, $LaCl_3$ etc.	various	Schottky defects
Alkaline earth oxide	Wurtzite & NaCl	Schottky defects. Cation concentration controlled by impurities
Fluorite structure UO_2, ZrO_2, CaO	Fluorite	Anion Frenkel defects
Transition metal oxide FeO, Cr_2O_3	Various	Cation diffusion by vacancies Oxygen diffusion by dislocations
Divalent Chalcogenides ZnS, PbTe	NaCl & others	Neutral Frenkel defects, both cation and anion
Small cations and large anions. AgI, $RbAg_4I_5$ etc	Mostly cubic	Cation disorder

Table 1.1: *Some properties of popular ionic materials [4], fcc = face centred cubic.*

As we have indicated earlier, the main source of ionic conduction in solids is through imperfections in the crystals. Following [5], the ionic conductivity of a solid is given by:

$$\sigma_{ion} = N_{ion} e \mu_{ion}$$ (5.1)

where N_{ion} is the number of ions per unit volume that can change their position under the influence of an electric field and μ_{ion} is the mobility of these ions. For ions to be able to move in the crystal they must posses sufficient energy to overcome the energy barrier and also there must be a vacant position where the ion will have to move to, as illustrated in figure 5.5. Thus the ionic conduction mechanism operates through diffusion and the relationship that governs the diffusion coefficient D, and the mobility of ions is given by the well known Einstein relation [11]:

$$\frac{D}{\mu_{ion}} = \frac{\kappa T}{e}$$ (5.2)

[Assuming that one charge per unit atom is transported]

The temperature dependency of the diffusion coefficient is usually expressed using the Arrhenius equation:

$$D = D_o \exp\left(-\frac{E_a}{\kappa T}\right)$$ (5.3)

In this case E_a is the activation energy as shown in figure 5.5 and D_o is a pre-exponential factor that depends on the vibrational frequency of the atoms and
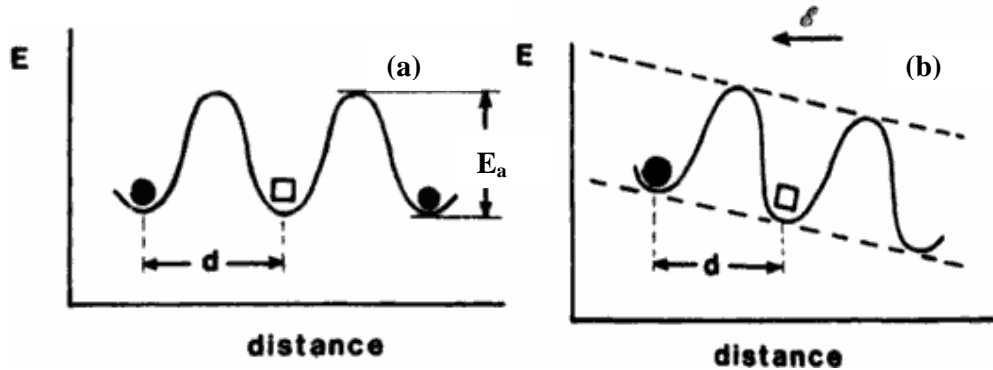
Figure 5.5: Schematic representation of potential barrier, which an ion ⬤ has to overcome to exchange its positional site with a vacancy ☐ (a): Without an external electric field, (b): With electric field, where d is the distance between adjacent equivalent lattice sites, E_a is the activation energy and ℰ is the electric field [5].

a number of structural parameters [5]. By substituting equations (5.2) and (5.3) in (5.1) one gets:

$$\sigma_{ion} = \frac{N_{ion} e^2 D_o}{\kappa T} \exp\left(-\frac{E_a}{K_B T}\right) \tag{5.4}$$

By comparing equation (5.3) to (5.4), one can represent the conductivity pre-exponential constant with σ_o and the equation becomes:

$$\sigma_{ion} = \sigma_o \exp\left(-\frac{E_a}{\kappa T}\right) \tag{5.5}$$

The activation energy of the process can be calculated from the slope of the plot of lnσ versus 1/T of equation 5.2. The Arrhenius plot of ionic conducting materials usually shows two regions within the ionic range known as the extrinsic and intrinsic regions. Figure 5.6 illustrates the temperature dependence of the conductivity due to
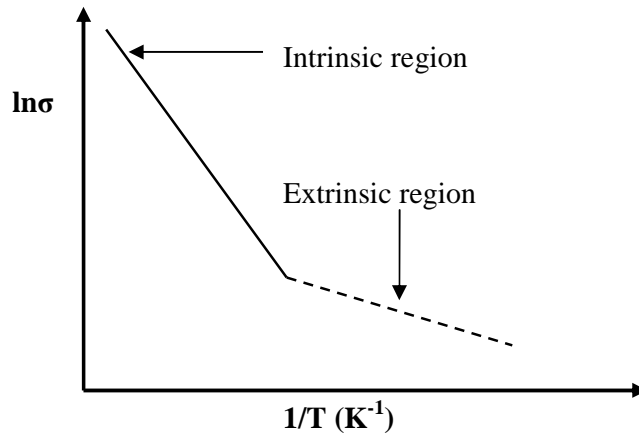
Figure 5.6: *Arrhenius plot of the conductivity of NaCl salt in the ionic regimes [5].*

the Na^+ ion in NaCl operating within the ionic range [5]. One could notice two distinctive regions representing two different activation energies occurring within the low and high temperature ranges respectively. The low temperature regime is known as the extrinsic region. In this region the activation energy is small and thermal energy is just sufficient to allow hopping of ions into already existing vacancy sites. On the other hand, the high temperature region is called the intrinsic region and in this region the thermal energy is large enough to create additional vacancies. Thus the activation energy is the sum of the activation energies for vacancy creation and ion movement.

Some ionic crystals show both ionic conduction and electronic conduction mechanisms. These materials are called mixed conduction. Pohl, [6] demonstrated

that alkali halides of ideal stoichometric composition are ionic conductors but electronic conduction in addition to ionic conduction occurs when there is an excess of halogen present. Other examples of mixed conducting materials include silver sulphide, cuprous sulphide and the cuprous halides. Further to this the ratio of the electronic to ionic conductivity of mixed conducting materials depends greatly on small deviations from ideal stoichiometry ratio [7]. In addition, the dominance of either electronic or ionic conductivity depends on the temperature [8], since at sufficiently low temperatures ions which are well known to be heavier than electrons and holes are frozen out and the conduction mechanism will usually be dominated by electronic processes. In the next section we shall present the electronic conduction process in terms of band gap theory.

5.2.2   Electronic Conduction in Solids

The origin of electronic conduction in solids can be understood by the application of the Schrödinger equation to the atoms in a solid. Several band theories including the tight binding model [9], Kronig-Pennel model [10] and density functional theory [9] predict that the allowed electron energies fall into a series of two bands called the conduction and the valence bands separated by a forbidden gap known as the band gap. The band theory partially explains the distinction between the conductivity of a metal, insulator and a semiconductor, since conduction could also be explained based on hopping of carriers. Also conduction could also take place via hopping. Figures 5.7 – 5.9 illustrate the band structures of these three types of materials.

Metal

The conduction band of a metal is believed to be either partially filled (such as Cu) or overlaps with the valence band (Zn) as shown in figure 5.7. Upon the application of a small electric field to a metal, electrons move to unoccupied states close to the occupied states, since there is no band gap separating the conduction and the valence bands. As a result metals have high electronic conductivity and high carrier mobility.
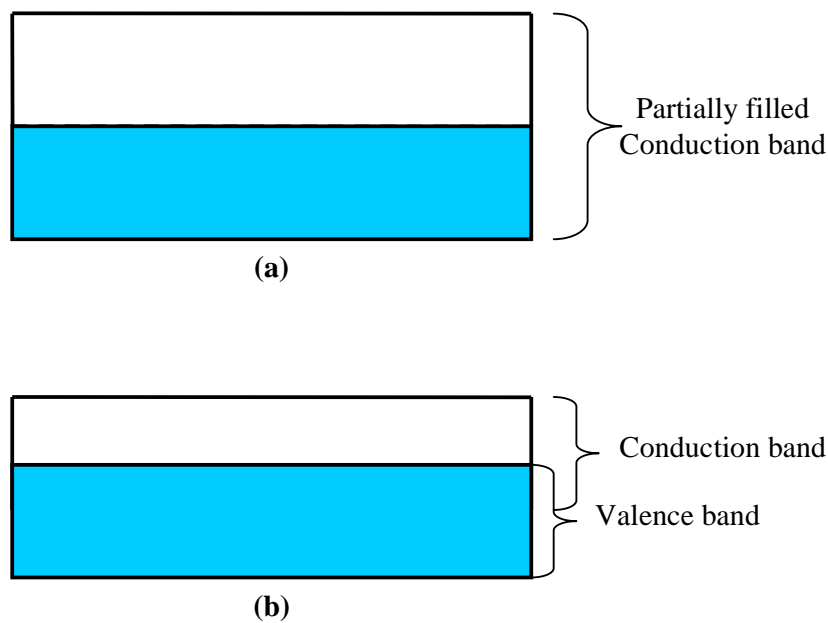

Figure 5.7: *Schematic energy band representation of a metal; (a): Partially filled conduction band (e.g. Cu), (b): Overlapping bands (e.g. Zn or Pb) [12].*

Insulator

The band structure of an insulator is depicted in figure 5.8. In the ideal situation, the valence band of the insulator is completely filled and the conduction band is completely empty. However, in a real sense, there are a few empty levels in the valence band and some electrons in the conduction band. Upon the application of an

electric field, very few electrons are able to cross over the large forbidden gap to the conduction band.
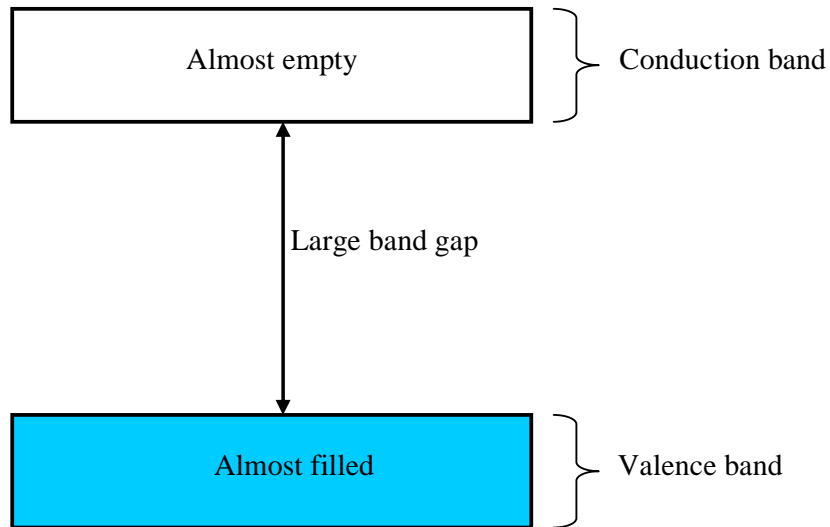
Figure 5.8: *Schematic energy band representation of an insulator [12].*

Owing to the strong bonding between the atoms and the large band gap between the conduction and the valence bands of insulators, they are characterised by very low electronic conductivity and mobility. Examples of this type of material include diamond, SiO_2, Al_2O_3, S_3N_4 etc.

Semiconductors

Semiconductors are materials with electronic properties intermediate between those of metals and insulators. The theory of electronic conduction in semiconductors may be traced to several published works by A.H. Wilson [13,14,15]. He proposed that

semiconductors are insulators at 0 Kelvin and that at this temperature the valence band is completely filled while the conduction band is empty.
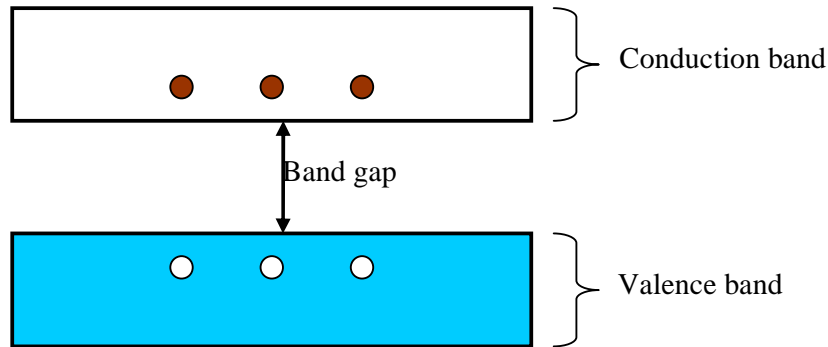
Figure 5.9: *Schematic energy band representation of a semiconductor [12].*

However as the temperature is raised, some electrons are raised to the conduction band thereby giving rise to electronic conduction. At room temperature, the energy band gap of the semiconductor is smaller, so also the valence band is less populated and the conduction band is more populated with electrons than for the case of an insulator. A typical schematic diagram of the band structure of a semiconductor is shown in figure 5.9. When an electron is raised into the conduction band, this leads to a missing electron or an empty state in the valence band. This empty state may be filled by neighbouring electrons in the valence band which in turn results in a shift in the location of the empty state. The empty state in the valence band is considered to be a quasi-particle called a hole. It carries a positive charge and moves in the opposite direction to the electron.

5.2.3   Intrinsic and Extrinsic Semiconductors

In his publications [13,14,15], A.H. Wilson distinguished between intrinsic and extrinsic semiconductors. An intrinsic semiconductor conducts in its pure state. In this case, electron-hole pairs are equally thermally generated and the concentration of the electrons equals that of the holes. According to [16], the generation of intrinsic carriers is determined by the thermal excitation and recombination of electron holes. Under steady state conditions, the generation rate of electron-hole pairs must be equal to the recombination rate of electrons and holes.

The carrier concentration of electrons in the conduction band under steady state conditions is given by the product of the density of states N(E) (density of allowed states per unit volume) and the probability of occupation of the energy level F(E), and taking the integral boundaries between zero (bottom of the conduction band) and the top of the conduction band [12]:

$$n = \int_0^{Etop} n(E)dE = \int_0^{Etop} N(E)F(E)dE \tag{5.6}$$

The probability of occupation of an electron in an electronic state with energy E is given by the Fermi-Dirac distribution function [17]:

$$F(E) = \frac{1}{1 + \exp[(E - E_F)/\kappa T]} \tag{5.7}$$

where E_F is the Fermi energy, κ is the Boltzmann constant and T is the absolute temperature. The temperature dependency of the Fermi-Dirac distribution is

illustrated in figure 5.10 [12]. One can observe that when an energy level E is occupied by an electron, F(E) = 1. Also F(E) = 0 for an empty level at absolute zero. Further to this, at temperatures above 0 K the F(E) is symmetrical around the Fermi energy E_F. For energies that are ~ 3κT above the Fermi energy equation (5.7) can be approximated [12] by:

$$F(E) \cong \exp\left[-\left(E - E_F/\kappa T\right)\right]$$ (5.8)

$$[\because \exp[E - E_F / \kappa T \gg 1]$$

and for energies that are ~ 3κT below the Fermi energy the equation (5.7) can be approximated by:

$$F(E) \cong 1 - \exp\left[-\left(E - E_F\right)/\kappa T\right]$$ (5.9)

The equation (5.9) can be regarded as defining the probability that a hole occupies a state located at energy E, since the probability of occupation of holes is given by:

$$F(E)_h = 1 - F(E)$$ (5.10)

For intrinsic semiconductor materials, one would expect that there would be a large number of empty allowed states and a few electrons in the conduction band. On the other hand there are large numbers of allowed states of which most are occupied by the electrons in the valence band.
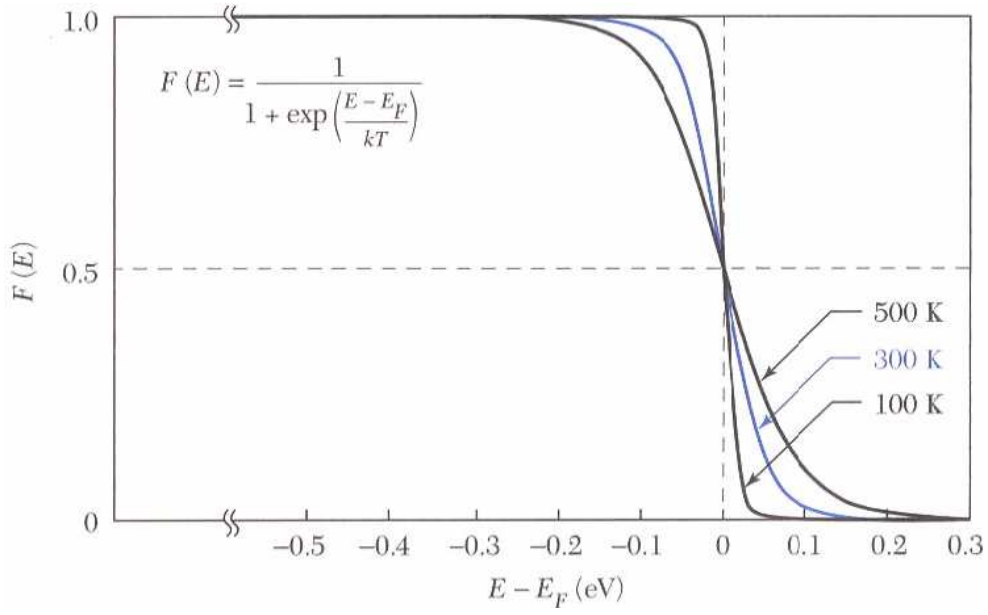
Figure 5.10: Temperature dependency of the Fermi-Dirac distribution [12].

Thus the probability that an electron will occupy one of the allowed states in the conduction band is very small when compared to the probability that an electron will occupy an allowed state in the valence band. By substituting equation (5.8) into (5.6) and noting that

$$N(E) = 4\pi\left(\frac{2m_n}{h^2}\right)^{\frac{3}{2}} E^{\frac{1}{2}} \tag{5.11}$$

then, the intrinsic electron concentration n becomes [12]:

$$n = \frac{2}{\sqrt{\pi}} N_C (\kappa T)^{-3/2} \int_0^\infty E^{1/2} \exp\left[-\left(E - E_F / \kappa T\right) dE\right] \tag{5.12}$$

$$[\because F(E) \to 0, \text{ when } (E - E_C >> \kappa T]$$

135

In this case m_n is the effective mass of the electron, h is the Planck constant and N_C is the effective density of states in the conduction band. By letting $x = E/\kappa T$ in equation (5.12) results in:

$$n = \frac{2}{\sqrt{\pi}} N_C \exp(E_F / \kappa T) \int_0^\infty x^{1/2} e^{-x} dx \qquad (5.13)$$

According to [18], the integral of equation (5.13) is of a standard form whose solution is $\sqrt{\pi}/2$. Thus the intrinsic electron concentration is given by:

$$n = N_C \exp[-(E_C - E_F)/\kappa T] \qquad (5.14)$$

The intrinsic hole concentration can be deduced in an analogous fashion to the electron and noting that the probability of occupation of holes in the valence band is given by equation (5.9):

$$p = N_V \exp[-(E_F - Ev)/\kappa T] \qquad (5.15)$$

where N_V is the effective density of states of holes in the valence band. Since the electron and holes are generated at equal rates in an intrinsic semiconductor, by equating equations (5.14) and (5.15) we can estimate the intrinsic Fermi level as:

$$E_F = E_i = (E_C + E_V)/2 + (\kappa T/2)\ln(N_V / N_C) \qquad (5.16)$$

At room temperature the term $(\kappa T/2)\ln(N_V/N_C)$ is very small compared to

$E_F = E_i = (E_C + E_V)/2$ and thus the intrinsic Fermi level lies closely to the middle

of the band gap of the semiconductor.

An extrinsic semiconductor is formed when small quantity of foreign atoms known as

dopant is introduced to the crystal of an intrinsic semiconductor in order to increase

its electrical conductivity. Dopants introduce energy levels from which free carriers

can move into the bands. Either extra electrons or holes can be introduced into the

crystal by doping. The respective dopants are known as donors for semiconductors

that have excess electrons (n-type) and acceptors for semiconductors that have excess
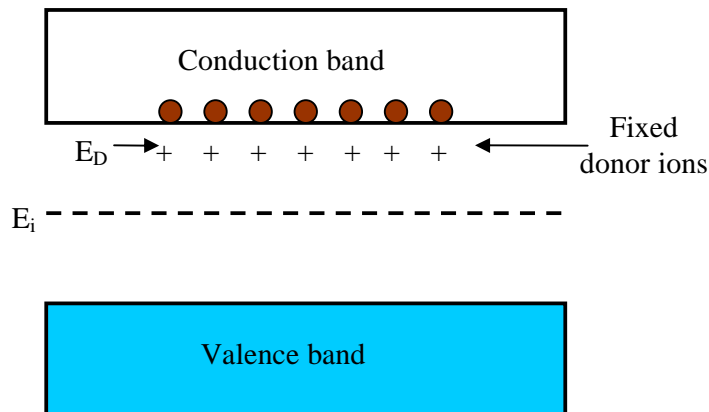
Figure 5.11: *Schematic energy band representation of n-type extrinsic semiconductor*
[12].

holes (p-type) as carriers. The band diagrams of both n and p-type semiconductors are

shown in figure 5.11 and 5.12, respectively. The donor impurity level is normally

situated near the conduction band and when the thermal energy exceeds the small

ionisation energy of the donor atoms, electrons will be raised into the conduction band

as shown in figure 5.11, resulting in electrical conduction. Under complete ionization conditions, the electron density, n, in the conduction band equals to the donor concentration, N_D, therefore we can write:

$$n = N_D \qquad (5.17)$$

Combining equations (5.14) and (5.17) gives the Fermi level for an n-type semiconductor material (E_{Fn}) in terms of the effective density of states N_C and donor concentration N_D as:

$$E_{Fn} = E_C - \kappa T \ln(N_C/N_D) \qquad (5.18)$$
$$[\text{Assuming } E_C - E_F \gg \kappa T]$$

In a similar a manner to the donor levels, at sufficient thermal energy, electrons are raised from the valence band to the acceptor level leading to the formation of holes in the valence band as illustrated in figure 5.12. Similarly for complete ionization, the hole concentration, p, equals the acceptor concentration N_A:

$$p = N_A \qquad (5.19)$$
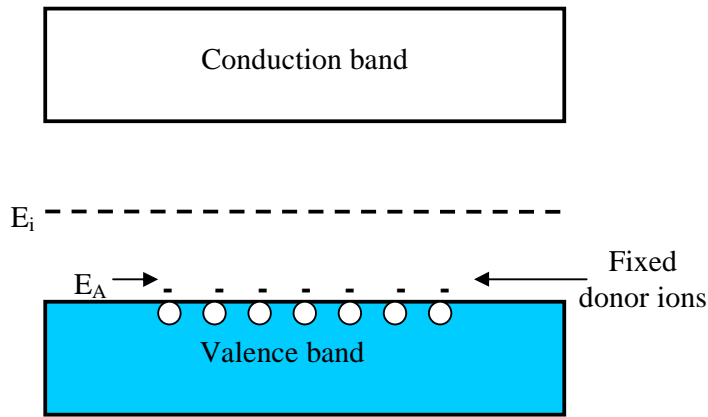
Figure 5.12: Schematic energy band representation of p-type extrinsic semiconductor [12].

and combining equations (5.15) and (5.19) gives the Fermi level for a p-type semiconductor material (E_{Fp}) in terms of the effective density of states N_V and acceptor concentration N_A as:

$$E_{Fp} = E_V + \kappa T \ln(N_V / N_A) \tag{5.20}$$

The electronic conductivity σ_{ele}, of an extrinsic semiconductor material under full ionisation of impurities is given by an expression similar to the ionic conductivity [19]:

$$\sigma_{ele} = Ne\mu_{ele} \tag{5.21}$$

where N is the effective donor or acceptor concentration and μ_{ele} is the mobility of the electronic carrier.

5.3 Experimental

5.3.1   Film Deposition

The detailed procedure for the substrate preparation and CuCl film deposition has been given in sections 2.2 and 2.3.1, so only a brief re-cap of the process is given here. Thin films of CuCl were deposited on cleaned square cut soda lime glass, indium tin oxide (ITO) and silicon substrates using an Edwards Auto 306 vacuum evaporation system at a base pressure of the order of 1×10^{-6} mbar. The thickness of films was between 100 – 500 nm at a constant growth rate of ~ 0.5 nms^{-1} as indicated by the thickness monitor.

Some of the deposited CuCl films were plasma immersed using an Oxford Instruments Plasma Lab Plus 80 reactive ion etcher (RIE) in order to introduce oxygen atoms into the CuCl crystals to improve of the electronic conductivity. Oxygen and argon were entered via dedicated channels at flow rates of 80 sccs for oxygen and 20 sccs for argon, the RF power was 300 W, while the chamber pressure was held at 50 mTorr. The duration of the plasma immersion was for 1, 2, and 3 minutes for the different samples.

5.3.2   Characterisation Techniques

Electrical characteristics were measured using both reversible and irreversible electrodes (copper and gold) in two configurations: Cu/CuCl/Cu and Au/CuCl/Au. Several structures were investigated including point planar, rectangular planar and sandwich electrode structures as shown in figure 5.13. Both point planar and rectangular planar electrode structures are robust and very easy to fabricate but have the disadvantage of presenting high resistance due to the large distances between electrodes. On the other hand, sandwich structures are more difficult to fabricate but have the advantage presenting lower resistance at low temperatures when compared to planar structures. Conventional mask lithography was used in defining these structures. Parasitic effects were excluded from the active area by the use of protective guards around the active region in a similar fashion to Meijer *et al*. [20].

Temperature dependent AC measurements were examined using electro-impedance spectroscopy from 160 K up to 400 K. Impedance spectra were recorded with a frequency network analyser (Solatron 1260) in a frequency range between 10 mHz and 1.5 MHz with a signal amplitude of 20 mV.

Two point steady state room temperature current-voltage characteristics were obtained by utilizing an HP 4140B pA meter/DC voltage source as the source while the current was monitored. Electrical contacts were made to the electrodes by using a
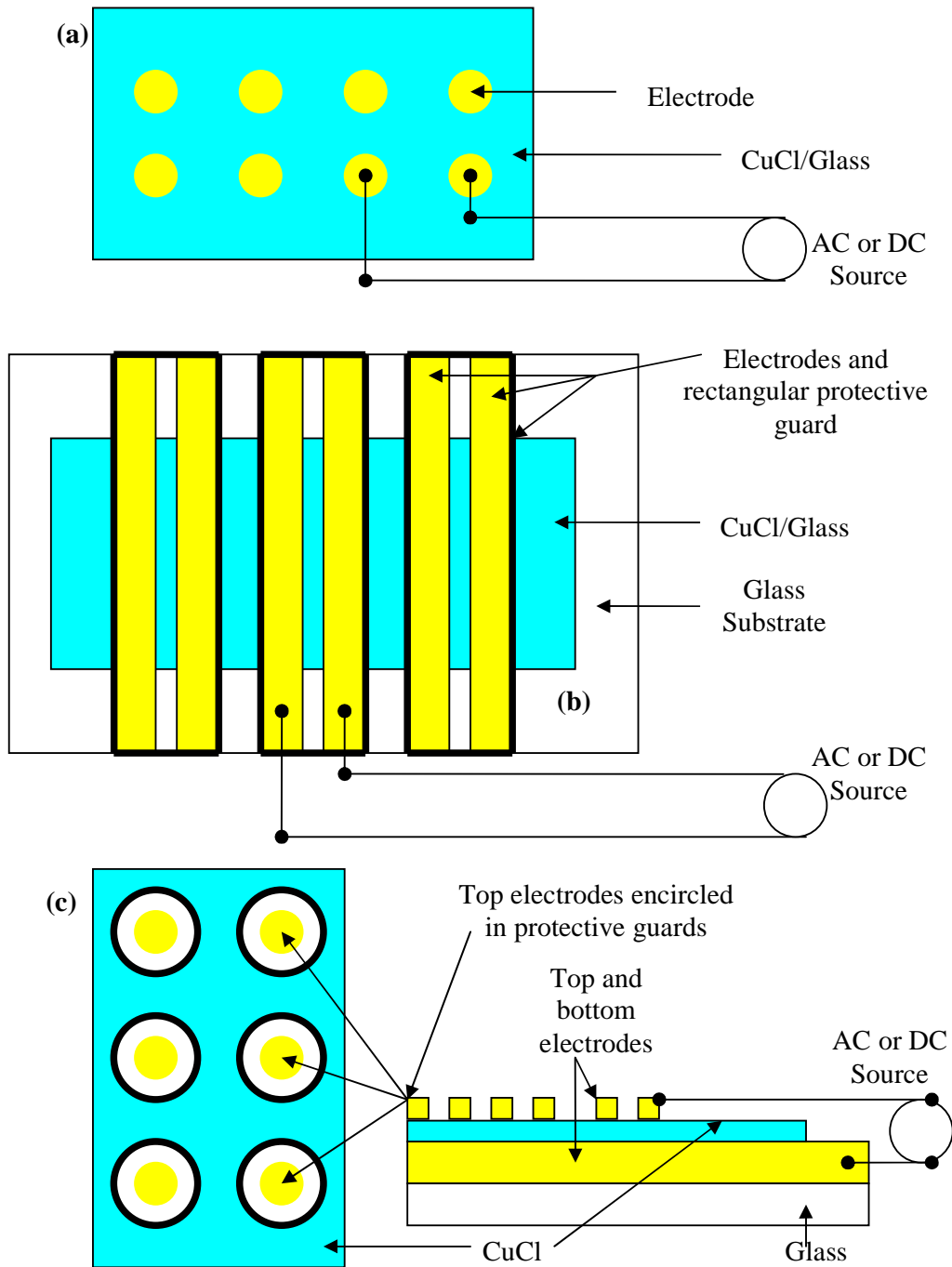
Figure 5.13: *Metal–CuCl–Metal structures; (a): Point planar, (b): Rectangular planar, (c): Sandwich structures. For (a) and (c) the radius of the top electrodes were between 1 – 3 mm while the dimensions of the rectangular electrode is 5mm x 15mm with inter-electrode spacings of 0.1 – 0.5 mm*

Cu or Au jumper wire of 0.025 mm diameter (Advent Research Materials Ltd) and quick drying silver paint (Agar Scientific). The samples were mounted in a light-tight, earthed, steel vacuum chamber, allowing electrical characterisation at a base pressure of the order of 10^{-3} mbar.

5.4   Results

5.4.1   DC Measurements of the As Deposited CuCl Films

The current – voltage (I–V) characteristics of mixed conducting semiconductor materials can be greatly dependent on the type of electrode used [21]. In this study both reversible (Cu) and irreversible electrodes (Au) were employed, the difference being that Cu^+ ions can swiftly be replaced with Cu, but Au (a blocking electrode) on the other hand, will block the injection of Cu into the films. A typical I–V characteristic of a Au/CuCl/Au structure at room temperature is shown in figure 5.14. The non–ohmic response of the electrical characteristic is considered to be due to the bulk properties of CuCl and not interfacial effects. CuCl is a well known mixed ionic – electronic semiconductor with p-type conductivity [22,23]. Following from general suggestions by Hebb [24], theoretical analysis [21] and experimental verification by Wagner and Wagner [23], an exponential current – voltage relation can be expected for a p-type mixed conduction material if the ionic current is suppressed by using blocking electrode(s) (Au).

Upon application of a DC voltage below the decomposition potential to a Au/CuCl/Au structure, interstitial copper ions migrate initially from the positive
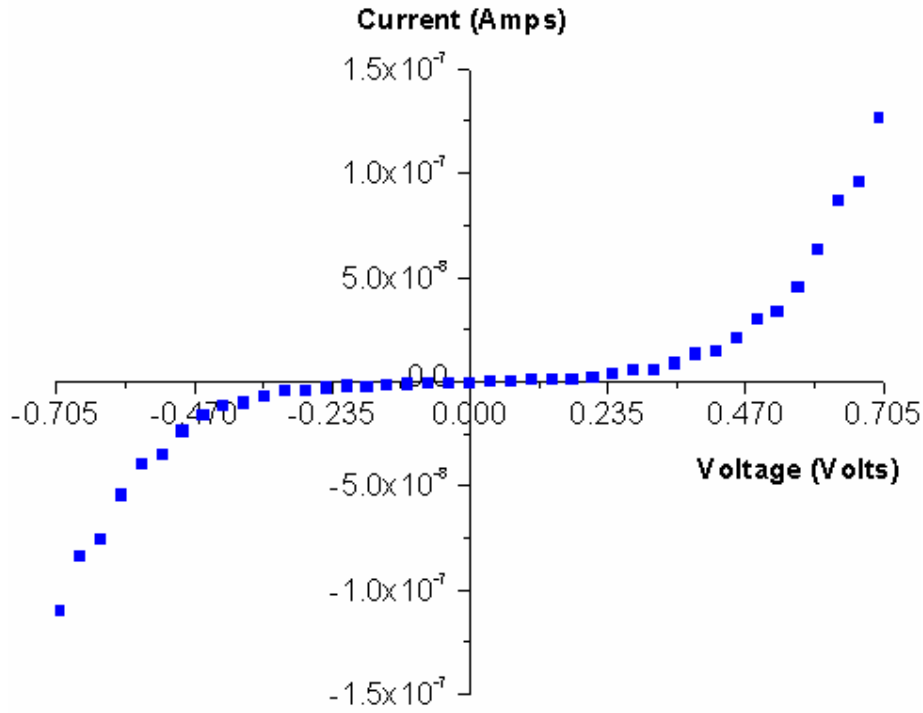
Figure 5.14: *Room temperature I–V plot for a typical Au/CuCl/Au structure.*

terminal towards the negative terminal, while electrons move in the opposite direction. Since there is no supply of copper ions from the positive electrodes, a copper deficit originates at the positive electrode. At steady state conditions, the migration of copper ions due to electric field is balanced by diffusion due to the carrier gradient [21,23]. Thus the current will be mainly carried via an electronic conduction mechanism. Using this analogy Wagner [21,23] deduced the total current density flowing through a mixed ionic semiconductor to be:

$$J = \frac{I}{A} = \frac{RT}{dF}\left\{\sigma^-\left[1-\exp\left(\frac{VF}{RT}\right)\right]+\sigma^+\exp\left(\frac{VF}{RT}-1\right)\right\} \qquad (5.22)$$

where V is the applied voltage which must be below the decomposition voltage of film, I is the current, A is the cross-sectional area, d is the film thickness, F is the Faraday constant, R is the gas constant, T is the absolute temperature in Kelvin, σ^- and σ^+ are electron and electron hole conductivities coexisting with the metallic ionic conductivity in a mixed ionic – electronic material, respectively. By assuming that the excess electron density is negligible and that holes dominate the electronic conductivity, equation (5.22) resolves into:

$$J = \frac{I}{A} = \frac{RT}{dF}\left\{\sigma^+ \exp\left(\frac{VF}{RT}-1\right)\right\} \qquad (5.23)$$

This equation captures the exponential nature of the I–V characteristics of figure 5.14, indicating the dominance of hole conduction mechanism. On taking the natural logarithm of equation (5.23) we get:

$$\ln I = \ln\left(\frac{\sigma^+ ART}{dF}\right) + \left(\frac{VF}{RT}-1\right) \qquad (5.24)$$

The hole conductivity σ^+, in co-existence with the ionic conductivity in a mixed ionic semiconductor material can in principle be estimated from the analysis of equation (5.24) [21,23]. We have observed variations in the value of the hole conductivity of several samples fabricated under the same experimental conditions. An average hole conductivity of $\sim 2.3 \times 10^{-7}$ S/cm was deduced to be in co-existence with Cu^+ ionic conductivity using equation (5.24). This value could be compared to a value of the order of 10^{-5} S/cm calculated for RF sputtered CuBr films confined between gold

145

electrodes [25]. The tendency corresponds to the increasing ionicity of bonds in the series: CuI < CuBr < CuCl.
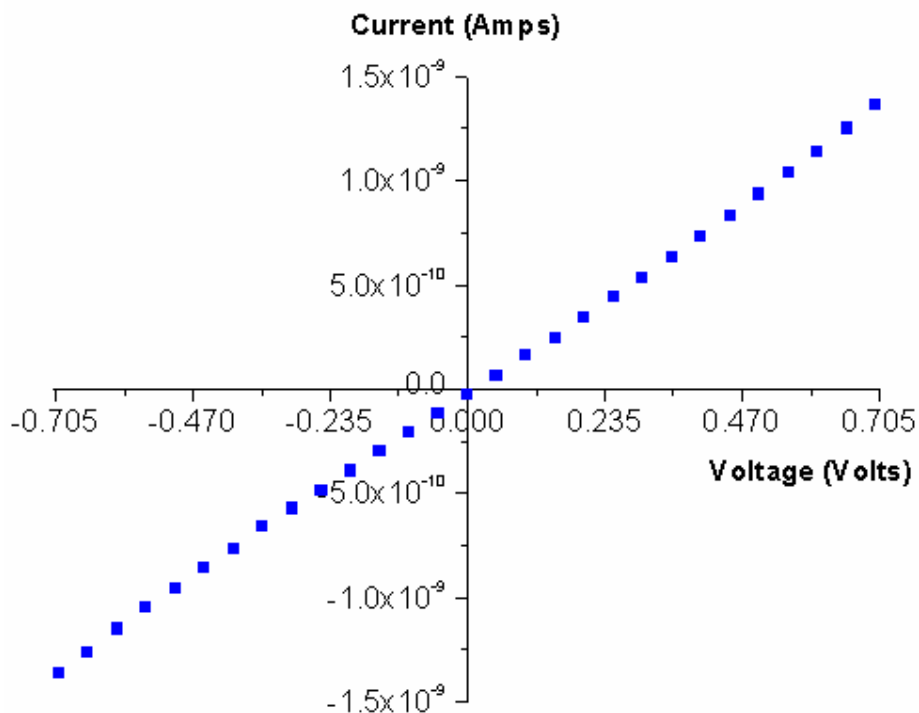
Figure 5.15: *Room temperature I–V plot for a Cu/CuCl/Cu structure.*

According to Tubandt [7], both the electronic and ionic conductivities of mixed conducting materials depend greatly on small deviations from the ideal stoichiometric ratio. Also Wagner [21] and other workers [26,27,28] demonstrated that a very small trace of excess halogen or oxygen could significantly change the electrical conductivity of the cuprous halide materials. Therefore variations up to a factor of 7 in the value of the conductivity of samples fabricated under the same experimental conditions is ascribed to the inability of the vacuum evaporation method to precisely deposit films with the same stoichiometry consistently. A similar variation of

electronic parameters was reported by Brinkman [29] for vacuum evaporated $NiMn_2O_{4+\delta}$ films.

With the films confined between Cu electrodes (figure 5.15), the same experiment gave an Ohmic relation with a maximum current density of about 100 times lower than for the film with Au electrodes (figure 5.14). This is not due to a contact limiting mechanism such as the well known Schottky emission, but rather is in agreement with Wagner's defect chemistry analysis of mixed semiconducting materials [21]. Thus when a mixed ionic – electronic material is equilibrated with its parental metal, it tends to become a nearly ideal stoichometric material. This is due to the fact that excess Cu^+ interstitial ions and Cu vacancies are being consumed by the reversible nature of the Cu electrodes. A total conductivity of 6.5×10^{-7} S/cm was obtained from the slope of the I–V data of figure 5.15, which is comparable to a value of the order of 10^{-8} S/cm obtained for bulk CuCl samples [30,31].

5.4.2   AC Measurements of the As Deposited CuCl Films

Impedance spectroscopy is a well known powerful AC technique used in separating the bulk and interfacial phenomena in various materials [32]. The most commonly assumed equivalent circuit for impedance spectroscopy of a sample under test consists of a series of RC components. The real (Z') and the imaginary (Z'') parts of the complex impedance are given by [33]:

$$Z' = R_B / [1 + (\omega/\omega_B)^2] + R_{gb} / [1 + (\omega/\omega_{gb})^2] +$$

$$R_{el} / [1 + (\omega/\omega_{el})^2] \qquad (5.25)$$

and

$$Z'' = -[R_B(\omega/\omega_B)/[1 + (\omega/\omega_B)^2] + R_{gb}(\omega/\omega_{gb})/[1 + (\omega/\omega_{gb}) +$$

$$R_{el}(\omega/\omega_{el})/[1 + (\omega/\omega_{el})^2]] \qquad (5.26)$$

where subscripts B, gb and el denote the bulk, grain boundaries and electrode processes, respectively, and

$$\omega_i = 2\pi f_i = 1/(R_i C_i) \qquad (5.27)$$

is the angular frequency of the term i. The high frequency component usually corresponds to the bulk properties as measured for single crystals [34], while the intermediate frequency term is ascribed to the grain boundary and the low frequency term corresponds to electrode processes. Analysis of impedance data is usually carried out on a Cole–Cole plot (Nyquist plot) ($-Z''$ vs Z') and equations (5.25 – 5.26) give rise to semi-circles in the complex plane. In a situation where the grain boundaries and the electrode effects of the polycrystalline material are very small with respect to the bulk effect, equations (5.25) and (5.26) reduce to:

$$Z' = R_B / [1 + (\omega/\omega_B)^2] = (R / [+(\omega RC)^2]) \qquad (5.28)$$

$$Z'' = -R_B(\omega/\omega_B)/[1+(\omega/\omega_B)^2] = -(\omega R^2 C/[1+(\omega RC)]^2) \qquad (5.29)$$

Under this situation the Nyquist plot of a polycrystalline material gives a single nearly ideal semi-circle. A typical example of such plots is shown in figure 5.16. By examining figure 5.16, one can observe that the Nyquist plot has two solutions for the real impedance axis (Z′) occurring at R_∞, as $\omega \to \infty$ and R_0, as $\omega \to 0$ and further to this, the quantity $|R_0 - R_\infty|$ is the resistance of the material. Using this simple analogy, the conductance of a material can be obtained across the temperature range and fitted to the Arrhenius equation.
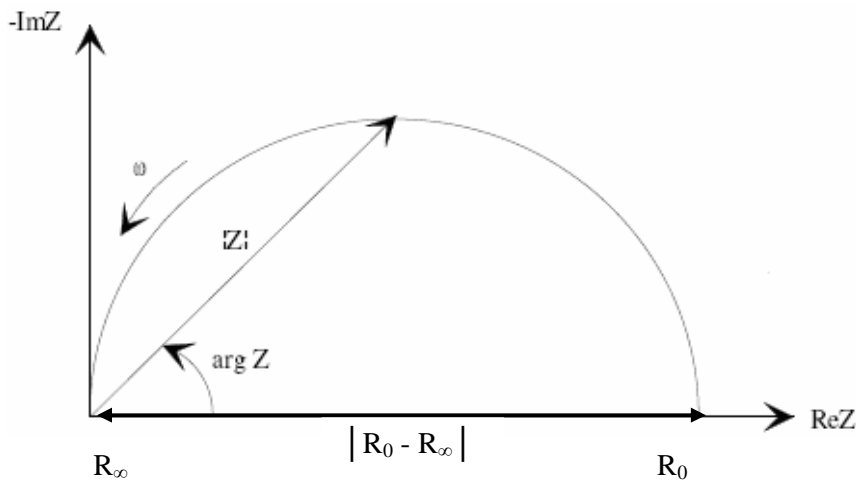
Figure 5.16: Cole–Cole plot (*Nyquist plot) of a single crystal film or a polycrystalline film for which the grain boundaries and electrode effects are very small as compared to the bulk effect.*

In our experiments, the Nyquist plots reveal well defined nearly ideal semi-circles across the temperature range of 160 K – 400 K using Au electrodes. An example of
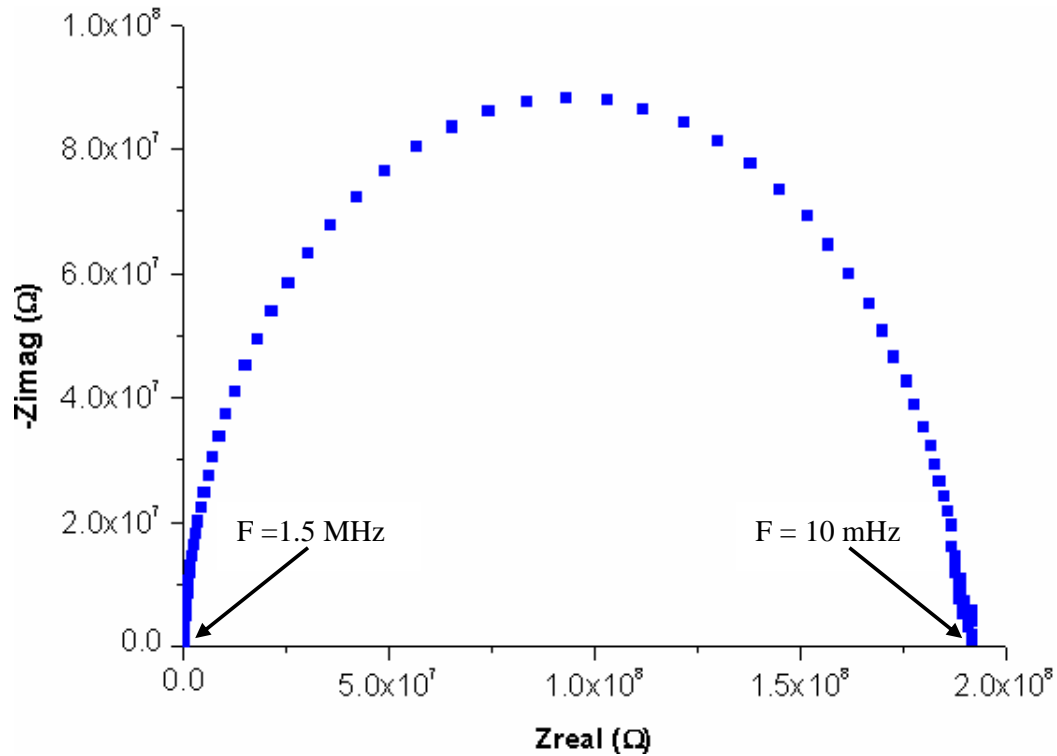
Figure 5.17: *A Cole–Cole plot (Nyquist plot) for the as deposited CuCl film at 300 K.*

such plots at 300 K is shown in figure 5.17 and thus the bulk resistance and the conductance of the CuCl films were deduced via the intersections of the semicircle on the real impedance axis in the complex plane as previously explained. The temperature dependency of the electrical characteristics as seen on the Arrhenius plot of figure 5.18 shows that the conductance of the CuCl films increases as the temperature increases. Further to this one can observe two distinct lines which are attributed to two different processes across the temperature range. The activation energy above ~ 270 K was deduced to be 0.43 ± 0.01 eV, which is attributed to extrinsic Cu^+ ionic conduction by a vacancy mechanism and is in excellent agreement with previous work on compressed polycrystalline materials, (0.44 eV) [31] and (0.45 eV) [35]. The second process occurs below ~ 265 K whose activation energy varies
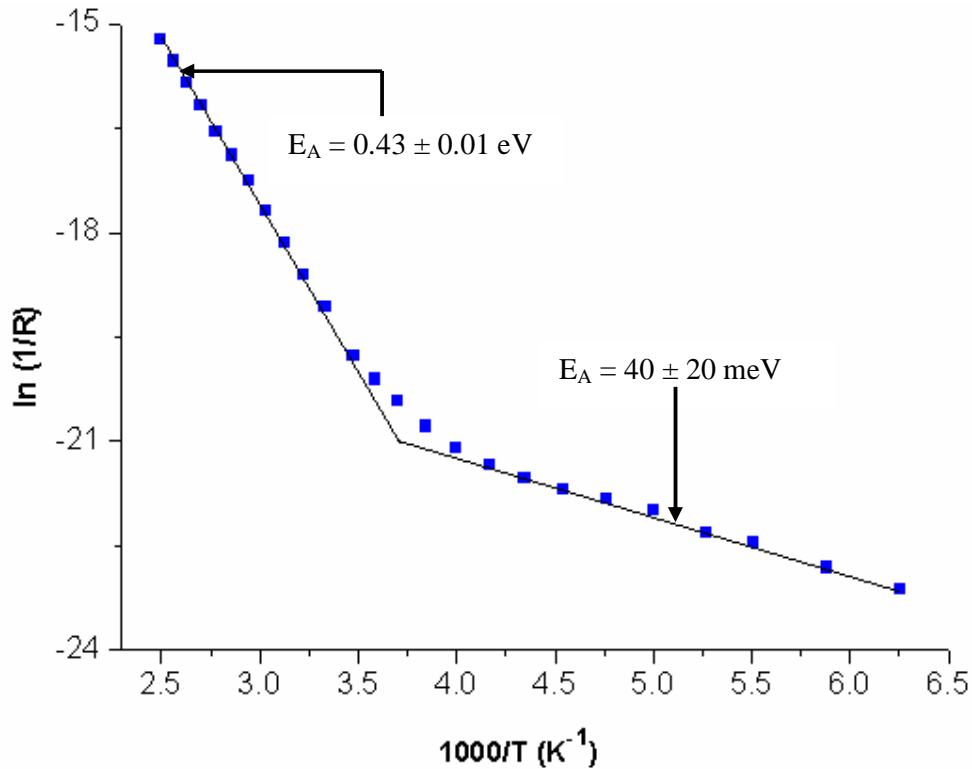
Figure 5.18: *Arrhenius plot for the AC conductance of the as deposited CuCl films.*

slightly with different samples grown under the same experimental conditions in a similar manner to the DC measurements. In all cases, the activation energy of the samples were within a range of 40 ± 20 meV. At this temperature, the thermal activation energy is too low to maintain substantial ionic motion and thus the mode of conduction is ascribed to a dominant hole conduction mechanism. Similar activation energies for both Cu^+ ionic and hole conduction mechanisms have been demonstrated for CuBr, a closely related material [36,37]. The slight difference in the values of the activation energy and conductance for different samples may be again ascribed to the inability of the vacuum evaporation method to precisely deposit films with the same stoichiometry consistently as previously explained.

## 5.4.3 DC Measurements of the O$_2$ Plasma Treated CuCl Films

The DC measurements of the plasma immersed films were investigated using Au electrodes. The Au electrodes have the advantage of not been able to fix the stoichometry and thereby increasing the electronic conductivity of the CuCl film. Figure 5.19 – 5.21 depict the DC measurements of the plasma immersed CuCl films, which were tested for durations of 1, 2 and 3 minutes, respectively.
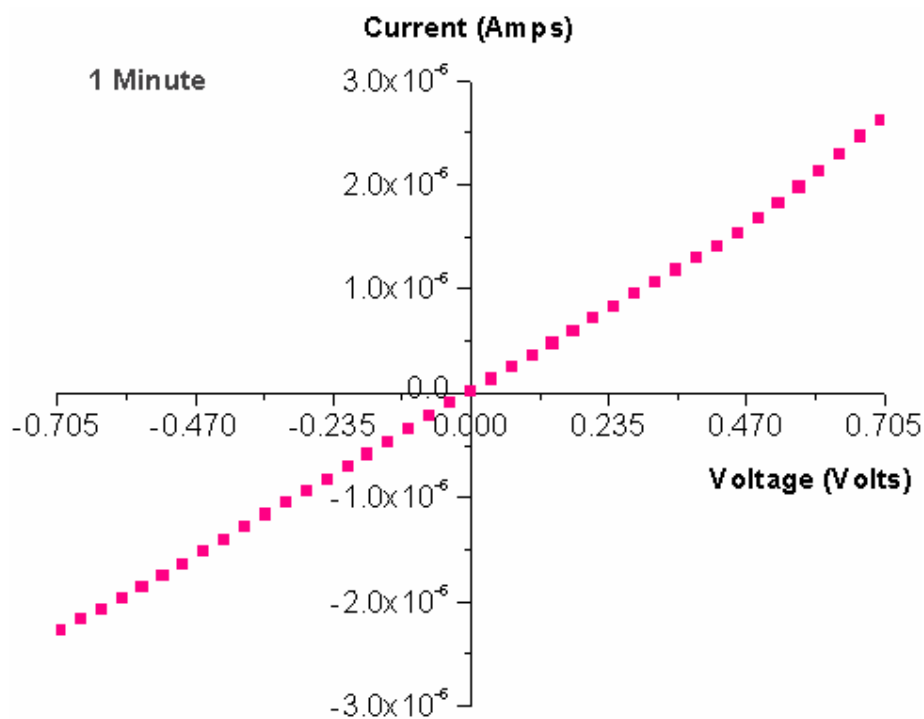
Figure 5.19: *Room temperature I–V plot for the 1 minute plasma immersed CuCl film.*

By comparing the I–V characteristics of the untreated films to the plasma immersed films of figures 5.19 – 5.21, one can observe that the electrical characteristics are
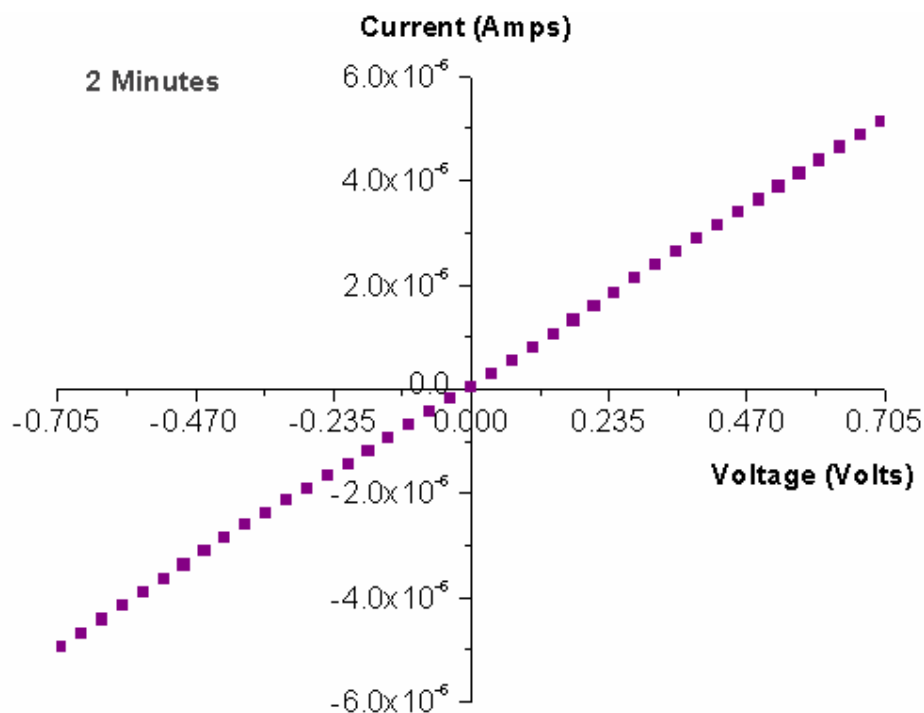
Figure 5.20: *Room temperature I–V plot for the 2 minutes plasma immersed CuCl film.*

almost Ohmic similar to the situation of using Cu electrodes but with a higher current density. If substantial Au ions were diffusing into the CuCl crystals, then the current density in the films should be significantly lower than for the untreated film (figure 5.14). But in this case the current density increases with oxygen plasma treatment duration. Therefore the large increase in the conductivity of the treated CuCl films (~ 100 fold higher than the untreated films) is ascribed to effect of O_2 introducing acceptor states in CuCl films. This is due to the fact that O_2 dissolves in cuprous halides on substitutional anionic sites [23,38] according to the doping reaction:

$$(1/2)O_2 + V_{Cl}^{o} \rightarrow O'_{Cl} + 2h^{o} \tag{5.30}$$
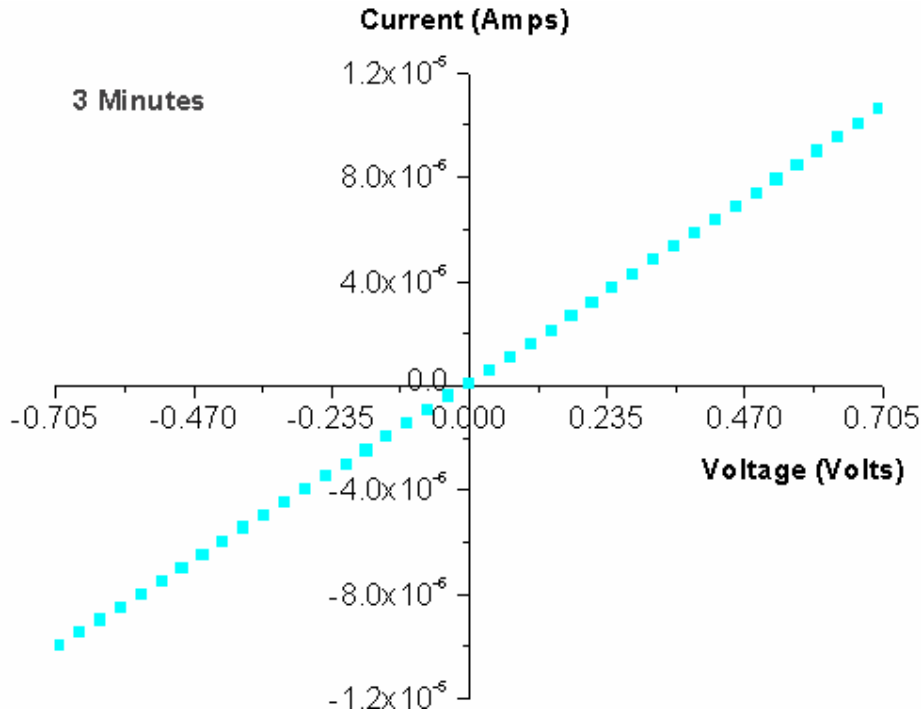
Figure 5.21: *Room temperature I–V plot for the 3 minutes plasma immersed CuCl film.*

where V_{Cl}^{o} is a chlorine vacancy, O'_{Cl} is an oxygen on chlorine site and h^{o} represents a hole. In a related development, Knauth and co workers [38,39] investigated the electrical properties of as deposited compressed and oxygen aerated CuBr films by performing four-point Hall effect measurements and Mott-Schottky analysis on semiconductor (CuBr) electrolyte (aqueous $CuSO_4$) contacts. They concluded that both the as deposited and aerated films were p-type semiconductors and the electronic hole conductivity could be substantially increased through oxygen aeration.

Preliminary secondary ion mass spectroscopy (SIMS) measurements revealed that oxygen penetration depth was ~ 75 nm, ~ 103 nm and ~ 300 nm for plasma immersion durations of 1, 2, and 3 minutes, respectively and more SIMS experiments

are currently ongoing. Several sets of samples were fabricated and it was observed that they all followed the same trend but with variations in the exact value of conductivity due to stoichiometry problems as earlier discussed. An average conductivity value of the order of 5.0×10^{-4} S/cm, 9.7×10^{-4} S/cm and 2.03×10^{-3} S/cm was deduced for the 1 minute, 2 minutes and 3 minutes plasma immersed films, respectively.
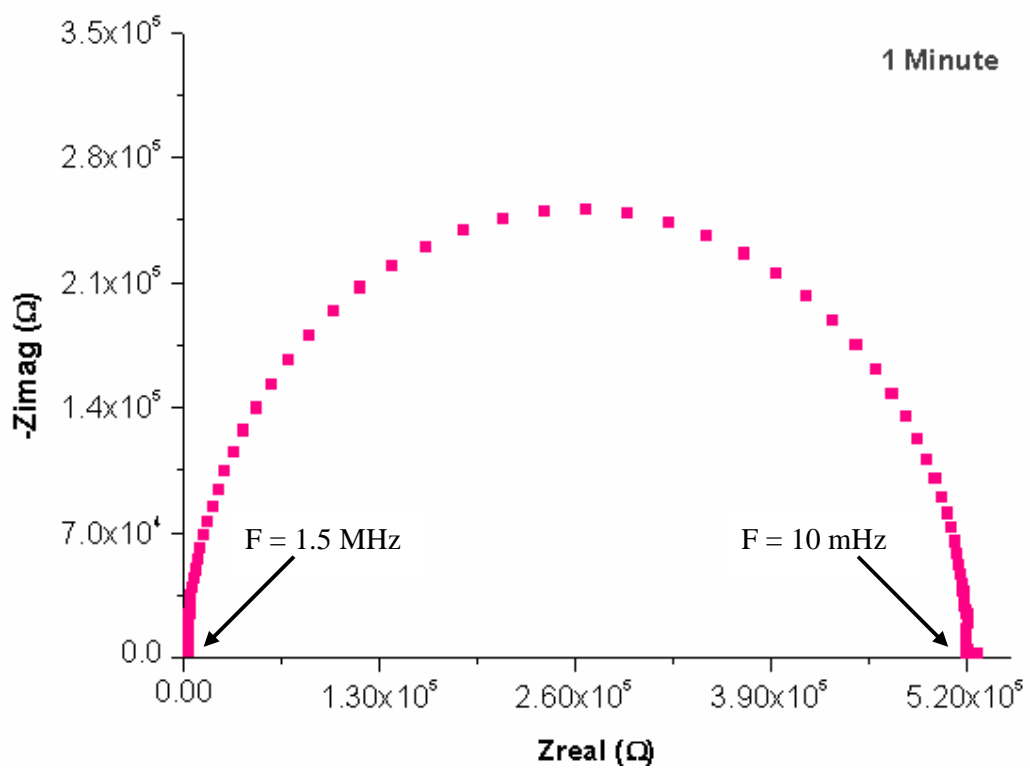

Figure 5.22: *A Cole–Cole plot (Nyquist plot) for the 1 minute plasma immersed CuCl film at 300 K.*

5.4.4   AC Measurements of the O$_2$ Plasma Treated CuCl Films

The AC electrical characteristics of the oxygen plasma immersed CuCl films were investigated using impedance spectroscopy and the data were represented on Nyquist plots as per the as deposited films. Well defined nearly ideal semi-circles were obtained across the temperature range of 160 K – 400 K using Au electrodes for all three plasma immersed samples. Figures 5.22 – 5.24 illustrate the Nyquist plots for the 1, 2 and 3 minutes immersed films at 300 K. The bulk resistance and the conductance of the films were deduced in a similar fashion to the untreated films via the intersections of the semi-circle on the real impedance axis.
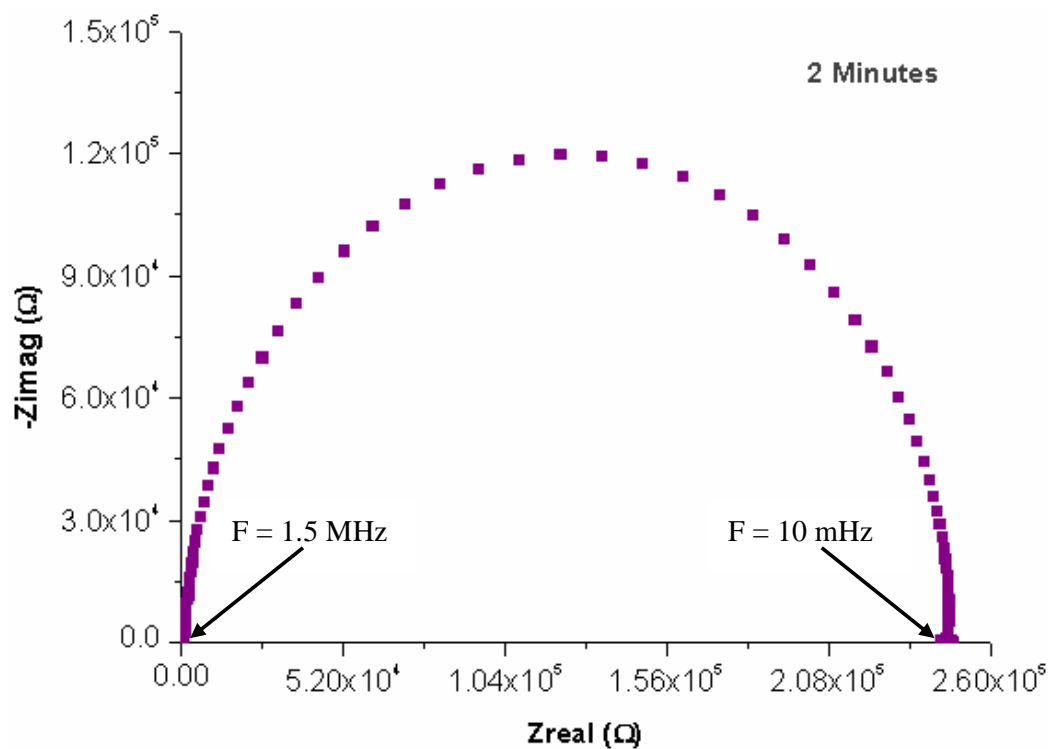
Figure 5.23: *A Cole–Cole plot (Nyquist plot) for the 2 minutes plasma immersed CuCl film at 300 K.*
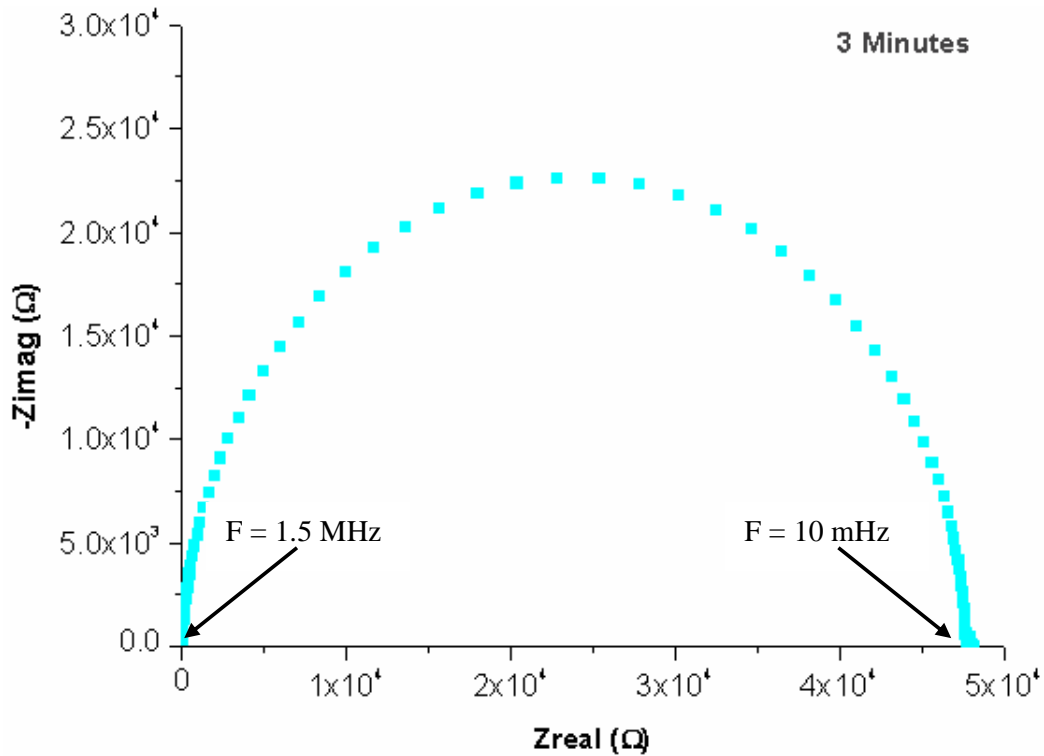
Figure 5.24: A Cole–Cole plot (Nyquist plot) for the 3 minutes plasma immersed CuCl film at 300 K.

By comparing the bulk resistance of the plasma immersed films, one can observe that the resistance reduces with an increase in plasma treatment duration, which is in excellent agreement with DC measurements.

The temperature dependence of the electrical characteristics as seen on the Arrhenius plot the of the untreated films reveals two distinct lines (Figure 5.18), corresponding to electronic conduction below ~ 265 K and Cu extrinsic ionic conduction mechanism as previously explained. While on the other hand the Arrhenius plots for the plasma treated films showed only a single line starting from low temperature extending across most of the temperature range. One can also see that the conductance of the plasma

treated films is much higher than that of the untreated films. This large increase in the conductance of the plasma immersed films is attributed to the dominance of the electronic conduction mechanism due to the fact that O_2 introduces acceptor states in CuCl films resulting in the liberation of excess holes as explained for the DC measurements.
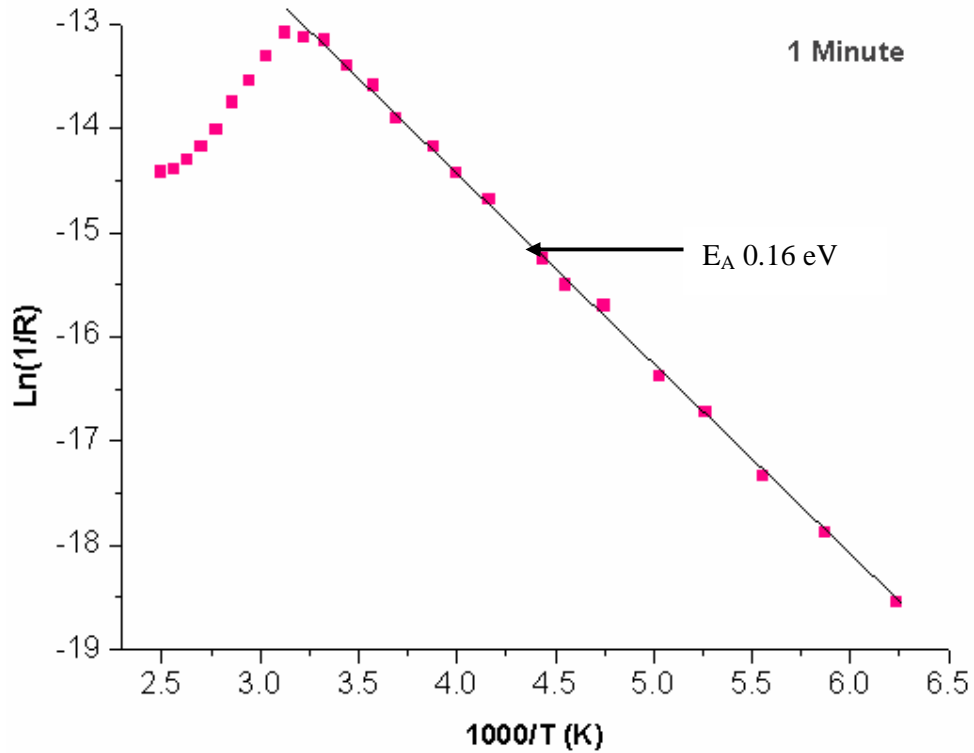
Figure 5.25: *Arrhenius plot for the conductance of the 1 minute plasma immersed CuCl film.*

The conductance as seen from the Arrhenius plot of the 1 minute and 2 minute oxygen plasma immersed films (figures 5.25 and 5.26) increases up to ~ 313 K and ~ 323 K respectively before declining. The reduction in the conductance of the films is ascribed to the escape of oxygen from the films, since the oxygen penetration depths were only 75 and 103 nm from the surface for the 1 minute and 2 minute oxygen

plasma immersed films, respectively. Thus it is expected that the conductance would reduce at substantial elevated temperatures. On the other hand the temperature dependency of the 3 minutes oxygen plasma immersed films (figures 5.27) shows that the conductance increases up to ~ 348 K before declining. The better stability of the conductance of the 3 minute immersed films as compared to previous two is attributed to the deeper penetration depth of oxygen (~ 300 nm) in these films.
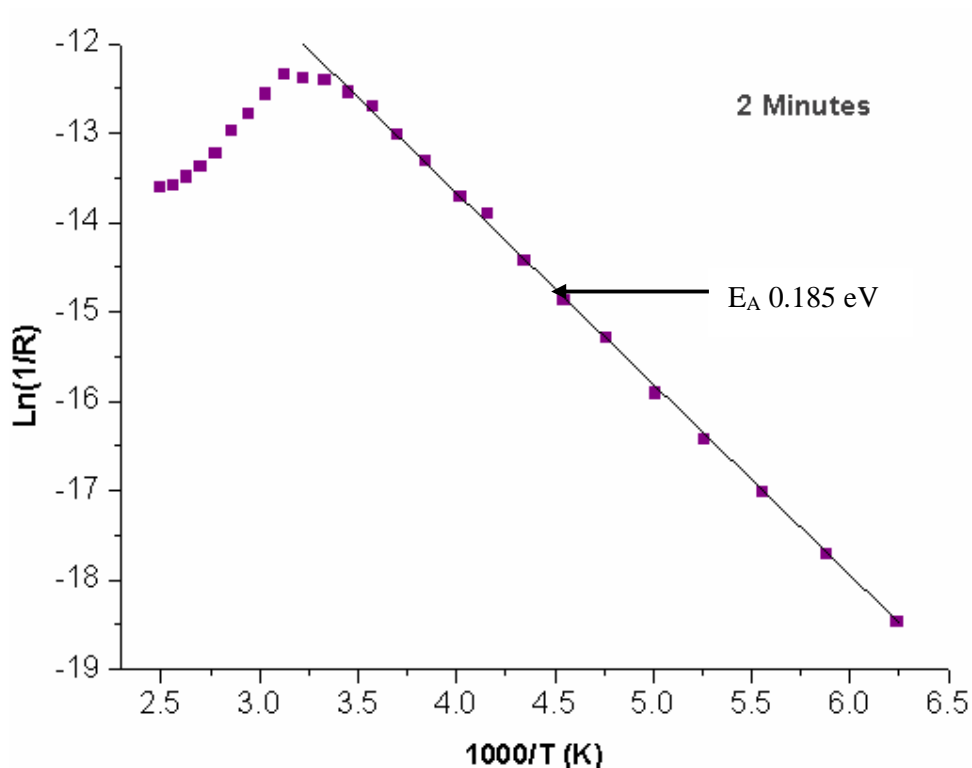
Figure 5.26: *Arrhenius plot for the conductance of the 2 minutes plasma immersed CuCl film.*

After the short decline in the conductance of the films, on further heating, all three samples showed the tendency of increasing conductance again. At this point, ionic conduction becomes significant due to high thermal energy. Several sets of samples

were fabricated and it was observed that they all followed the same trend but with variation in the exact value of conductance due to stoichiometry problems as earlier discussed. An average activation value of the order of 0.16 eV, 0.185 eV and 0.23 eV was deduced for the 1 minute, 2 minutes and 3 minutes plasma immersed films, respectively.
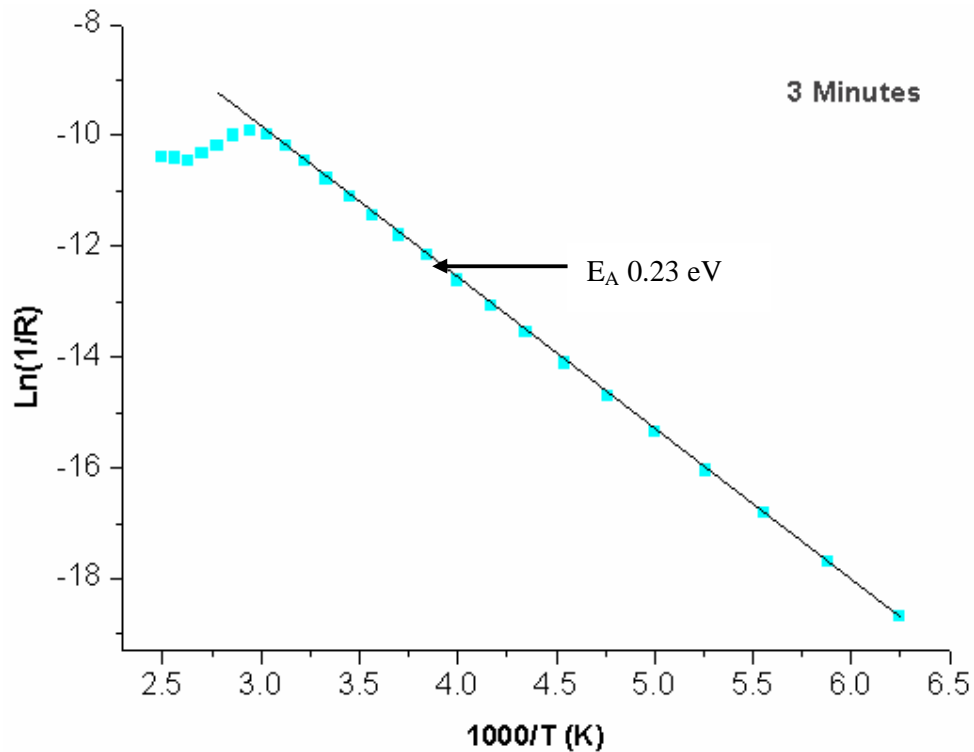

Figure 5.27: *Arrhenius plot for the conductance of the 3 minutes plasma immersed CuCl film.*

## 5.4.5   Electrolytic Decomposition of CuCl Films

Electrolytic decomposition, otherwise known as electrolytic conduction, is a well known property of polar crystals, which has been observed as far back as the 1920s. Tubandt and Eggert [40] in 1920 successfully demonstrated the transfer of Ag in

silver iodide via an electrolytic conduction mechanism under the influence of a steady state source. Molten polar salts are known to be among the best electrolytic conductors [8]. Electrolytic decomposition is quite different from dielectric breakdown and occurs when a polar material is subjected to a steady state source greater than its decomposition threshold. According to [37], the threshold voltage is a function of the combination of the thermodynamic decomposition voltage, which could be deduced from the Gibbs free energy of formation of CuCl ($2CuCl \rightarrow Cu + CuCl_2$; 0.77 V and $2CuCl \rightarrow 2Cu + Cl_2$; 1.22 V at 298 K [42]), over voltages for different processes, including ohmic drop, charge transfer at the electrodes (given by the Butler – Volmer equation [43]) and the nucleation of the electrodeposits.
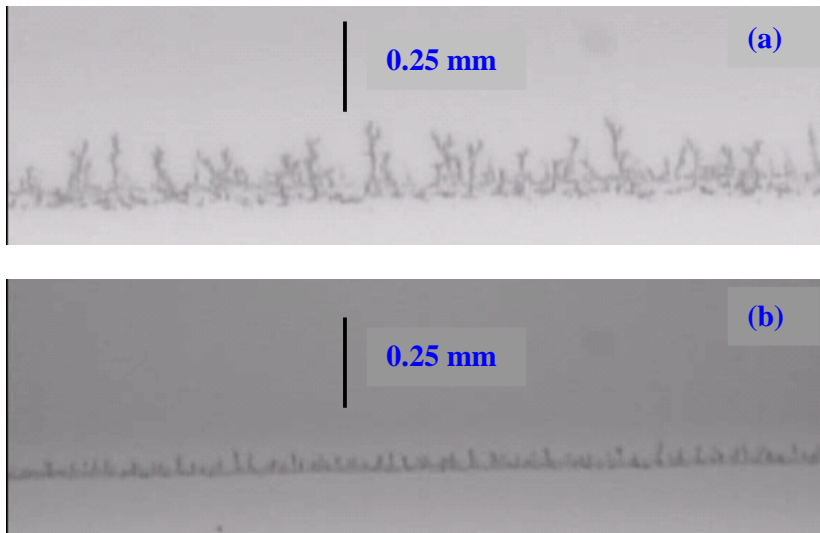
Figure 5.28: *Optical micrograph of the electrolytic decomposition pattern of CuCl films; (a): as deposited CuCl films, (b): 3 minutes plasma immersed CuCl films.*

161
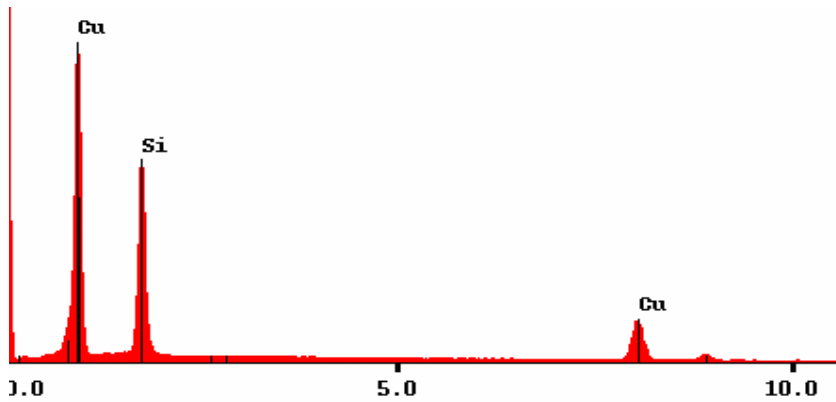
***Figure 5.29*:** *EDX spectrum of the cathodic decomposition of as deposited CuCl film on Si substrate.*

For most substances, electrolytic decomposition appears at the cathode in the form of tree-like threads called dendrites and the electrolytic conductivity may vary from one specimen to another by a factor greater than 100 at low temperatures [8].

In our experiments, we have observed the onset of cathodic decomposition for both as deposited and plasma immersed films when a steady state voltage of more than 5 V was applied to CuCl films between a pair of rectangular planar Au electrodes with an inter-electrode spacing of 0.25 mm. Figure 5.28 shows the optical micrographs of the as deposited and 3 minutes plasma immersed CuCl films confined between Au electrodes and subjected to a steady state DC bias of 10 V for 1 hour. An EDX microanalysis on the fractal growth (figure 5.29) confirmed that the dendrites are metallic copper. Also, we have observed what appeared to be lesser dendrite formation for the plasma immersed films. This could be easily seen especially for the 3 minutes plasma immersed films as illustrated in figure 5.28. However according to

162

Mott and Gurney [8], the rate of cathodic decomposition depends on each individual sample and it preparation, and may vary over by a factor of 100 at low temperatures. Therefore at this stage, we cannot explicitly confirm that influence of oxygen reduces the electrolytic decomposition of CuCl films.

5.5 Conclusion

In summary, the electrical properties of γ-cuprous chloride films confined between both reversible (Cu) and irreversible (Au) electrodes have been investigated. The effect of oxygen plasma treatment on the electrical characteristics was also examined:

- Room temperature DC measurements on the as deposited films, using irreversible electrodes (Au) gave an exponential response while using reversible electrodes (Cu) presented an Ohmic response with a maximum current density ~ 100 fold lower than the situation for the irreversible electrodes. This was interpreted to be the property of a p-type mixed ion – electronic semiconductor material with copper deficiency as explained by Wagner. The exact value of the electrical conductivity was found to vary from sample to sample due to the inability of vacuum evaporation to precisely deposit films of the same stochiometry under the same experimental conditions. An average hole conductivity of ~ 2.3×10^{-7} S/cm was deduced to be in coexistence with Cu^+ ionic conductivity using Au electrodes while a total conductivity of 6.5×10^{-7} S/cm was calculated using Cu electrodes.

- The temperature dependence of the conductance of the as deposited CuCl films were interpreted to be due to a predominantly Cu^+ extrinsic ionic conduction mechanism at temperatures above ~ 270 K and electronic hole

conduction dominant at temperatures below that, where the thermal energy is inadequate to sustain significant ionic motion.

- On the other hand the room temperature DC characteristics of the oxygen immersed films using Au electrodes all gave an Ohmic response with conductivity over 100 times higher than the untreated films. The large increase in the conductivity is ascribed to O_2 introducing acceptor states in CuCl films.

- The temperature dependence of the conductance of the oxygen immersed CuCl films was found to be dominated mainly by an electronic conduction mechanism up to a temperature where oxygen escapes from the films due to the heat treatment. Preliminary SIMS measurements revealed that the oxygen penetration was as deep as 300 nm for films immersed for a duration of 3 minutes.

- Both the as deposited and plasma immersed CuCl films showed evidence of cathodic decomposition when a voltage of more than 5 V was applied for periods of the order of 1 hour.

References

[1] J. Frenkel, *Zeits. f. Physik* **35** (1926) 652

[2] C. Wagner and W. Schottky, *Zeits f. Physical Chemistry* B **11** (1930) 163

[3] W. Jost, *Journal of Chemical Physics* **1** (1933) 466

[4] M.Z.A Munshi and P.S.S. Prasad, *Handbook of Solid State Batteries and Capacitors,* World Scientific Publishing, (1994)

[5] R.E. Hummel, *Electronic Properties of Materials,* Springer-Verlag New York Inc. (2001)

[6] Pohl, *Phys. Z.* **35** (1934) 107; **39** (1938) 36

[7] Tubandt, *Handbunch der Experimental Physik,* (ed. Wien and Harms), **12**:1 (1933) 412

[8] N.F. Mott and R.W. Gurney, *Electronic Processes in Ionic Crystals*, Oxford Press (1940)

[9] J. Singh, *Electronic and Optoelectronic Properties of Semiconductor Structure,* Cambridge University Press (2007)

[10] D.L Kronig and W.G. Penney, *Proceeding s of the Royal Society of London* **130** (1931) 499

[11] S.E. Guidoni and C.M Aldao, *European Journal of Physics* **23** (2002) 395

[12] S. M. Sze, *Semiconductor Dvices: Physics and Technology,* John Willey and Sons Inc (2002)

[13] A.H. Wilson, *Proceeding s of the Royal Society of London* A **133** (1931) 458

[14] A.H. Wilson, *Semiconductors and Metals,* Cambridge (1939)

[15] A.H. Wilson, *Proceeding s of the Royal Society of London* A **134** (1932) 277

[16] S. Mahajan and K.S. Sree Harsha, *Principles of Growth and Processing of Semiconductors,* WCB/McGraw-Hill (1999)

[17] T. Ihn, *Electronic Quantum Transport in Mesoscopic Semiconductor Structures* (Springer Tracts in Modern Physics), Sringer-Verlag (2004)

[18] K.A. Stroud, *Further Engineering Mathematics: Programs and Problems,* Springer-Verlag (1992)

[19] S.O. Kasap, *Principles of Electronic Materials and Devices,* McGraw Hill (2002)

[20] *E.J. Meijer et al.*, *Journal of Applied Physics* **93** (2003) 4831

[21] C. Wagner, *Z. Elektrochem* **60** (1956) 4

[22] A.V. Joshi and J.B. Wagner Jr, *Journal of the Electrochemical Society* **122** (1975) 1071

[23] J.B. Wagner and C. Wagner, *Journal of Chemical Physics* **26** (1957) 1597

[24] M. Hebb, *Journal of Chemical Physics* **20** (1952) 185

[25] P. Lauque, M. Bendahan, J –L Seguin, M. Pasquineli and P. Knauth, *Journal of the European Ceramic Society* **19** (1999) 823

[26] K. Bädecker, *Ann. Physik* **22** (1907) 749

[27] Okada, Kone and Uno, *Chemical Abstract* **44** (1950) 10421

[28] G. Rudert, *Ann. Physik* **31** (1910) 559

[29] R. Schmidt, A. Basu and A.W. Brinkman, *Journal of the European Ceramic Society* **24** (2004) 1233

[30] J. Rivera, L.A. Murray, and P.A. Moss, *Journal of Crystal Growth* **1** (1967) 171

[31] T.H. Ida, H. Saeki, H. Hamada and K. Kimura, *Surface Review Letters* **3** (1996) 41

[32]   J.R. McDonald, *Impedance Spectroscopy* John Wiley, N.Y. (1987)

[33]   J.C.C. Abrantes, J.A. Labrincha and J.R. Frade, *Materials Research Bulletin* **35** (2000) 727

[34]   I. Denk, J. Claus and J. Maiser, *Journal of the Electrochemical Society* **144** (1997) 3526

[35]   A. Brune and J.B. Wagner Jr, *Materials Research Bulletin.* **30** (1995) 573

[36]   M. Bendahan, J –L Seguin, P. Lauque, K. Aguir and P. Knauth, *Sensors and Actuators* B **95** (2003) 170

[37]   M. Bendahan, C. Jacolin, P. Lauque, J –L Seguin, and P. Knauth, *Journal of Physical Chemmistry* B **105** (2001) 8327

[38]   P. Knauth, Y. Massiani, M. Pasquinelli, *Physica Status Solidi* A **165** (1998) 461

[39]   P. Knauth and Y. Massiani, *Journal of Electroanalytical Chemistry* **442** (1998) 229

[40]   C. Tubandt and S. Eggert, *Zeits. f. anorg. Chem.* **110** (1920) 196

[41]   L.G. Harrison and M. Prasad, *Journal of the Chemical Society, Faraday Transactions* **70** (1974) 471

[42]   A.Bard and L. Faulkner, *Electrochemical Methods – Fundamentals and Applications* J. Wiley: New York (1980)

6

Encapsulation

6.1 Introduction

In the previous chapters, we highlighted the prime properties, which make CuCl attractive for optoelectronic applications. These include an excitonic binding energy of the order of 190 meV, which guarantees excitonic recombination [1], lattice mismatch of less then 0.4% when deposited on silicon substrates (a_{CuCl} = 0.541 nm and a_{Si} = 0.543 nm) [2], availability of bulk single crystal and the ease of deposition of CuCl thin films. Despite these outstanding features and the potential applications of CuCl, its stability to moisture in ambient air is a major problem. Thin films of CuCl oxidise completely into oxyhalides of Cu II within a few days of exposure to the ambient. In order to realise the practical use of this material an encapsulation layer is required.

Conventional encapsulation of CuCl thin films by solid sealed glass at curing/deposition temperatures greater than 250°C cannot be used because CuCl interacts chemically with Si at a temperature greater than 250°C [3]. Thus a low curing/deposition temperature, UV transparent and non-reactive protective layer is required to increase the longevity of this CuCl films. In this chapter, we present the

results for three candidate dielectrics used as protective layers for thin films of CuCl:

1. **SiO₂ deposited by plasma enhanced chemical vapour deposition (PECVD).** The PECVD grown SiO_2 has the advantage of low deposition temperature, which favours low defect formation in the underlying substrate, low dopant diffusion and little degradation of any adjacent metal layers [4]. The SiO_2 deposited using this method has found applications in film passivation, intermetal dielectric layers, in memory devices and in metal–insulator–semiconductor (MIS) devices.

2. **Organic polysilsesquioxane (PSSQ) spin-on glass based dielectric.** PSSQ has been identified and recognised as a potential candidate for the next generation of low dielectric constant materials [5] in Si integrated circuit technologies.

3. **Cyclo olefin copolymer (COC) based dielectric.** COCs are thermoplastic polymers. Popular commercial producers of this material include Mitsui Chemical Company, Ticona (formerly Hoechst Celanese), Japan Synthetic Rubber and Zeon Chemicals Company. There are several types of commercial cyclo olefin copolymers based on different monomers and polymerisation methods. COCs are produced by chain copolymerisation of cyclic monomers such as 8,9,10–trinorborn–2–ene (norbornene) or 1,2,3,4,4a,5,8,8a–octahydro–1,4:5,8-dimethanonaphthalene (tetracylododecene) with ethene, or by the ring-opening metathesis polymerisation of various cyclic monomers followed by hydrogenation [6]. Owing to their rigid monomer units, COCs have low dielectric loss, low dielectric constant, low moisture absorption, good chemical resistance to polar solvents, low shrinkage, excellent transmittance in

the visible and near-ultraviolet wavelengths and low birefringence [7]. Since the first report of the synthesis of COC in 1991 [8], it has found applications in optical, medical, electrical packaging and diagnostic containers.

This list is no means exhaustive, but these choices should help point the way for future encapsulation research. The optical properties (Ultra Violet/Visible and Infra Red) of the capped luminescent CuCl films were studied as a function of time and compared with bare uncapped CuCl films in order to test the efficiency of the protective layers.

6.2   Experimental

6.2.1   Film Deposition

The details of the procedure for the substrate preparation and CuCl film deposition has be given extensively in sections 2.2 and 2.7.5, so only a brief recap is given here. CuCl thin film samples with typical thicknesses of 100 – 500 nm were grown on Si (100) and quartz substrates using the vacuum deposition method at a base pressure of $\sim 1 \times 10^{-6}$ mbar. Immediately after the evaporation of CuCl, the protective layers were then deposited on the films. PECVD SiO_2 layer deposition was carried out using an oxygen/hexamethyldysiloxane (O_2/HMDSO) mixture in a parallel plate RF reactor at a frequency of 13.56 MHz. The O_2/HMDSO ratio was 10:1, while the RF power that determines the degree of excitation and fragmentation was kept constant at 350 W. The operating pressure was 10 Pa and the deposition time was 8 minutes. For the deposition of the organic PSSQ based layer, the CuCl films were spun or dipped in

Emulsitone glass forming solution (Emulsitone Inc, USA). The resulting film was annealed under nitrogen ambient at 160°C for a duration of 1 hour. The cyclo olefin polymer (COC) layer was deposited by dipping or spin coating COC solution (Brewer Science) on CuCl samples. The resulting film was annealed in nitrogen ambient at 175°C for 15 minutes. Using a stylus profilometer the thickness of the protective layers was estimated to be 300 nm for the PSSQ layer and 400 nm for both the PECVD SiO_2 layer and the COC layers.

Some of the deposited CuCl films were plasma treated using an Oxford Instruments Plasma Lab Plus 80 reactive ion etcher (RIE) in order to introduce oxygen atoms in the CuCl. The plasma immersion process described in section 2.7.6 was used, but the duration of the plasma immersion was mainly for only 1 minute. The oxygen plasma immersed films were encapsulated using both PSSQ and COC in the same manner as for the as deposited films. However in this case the films were not annealed in order to avoid the evolution of oxygen in the CuCl films as explained in section 5.4.4. During all the experiments, the samples were stored in individual transparent containers and exposed to air.

## 6.2.2   Characterisation Techniques

Absorption and IR measurements were carried out on the samples using a Perkin Elmer Lamda 40 UV/Vis spectrometer and a Perkin Elmer GX FTIR system. The spectra were taken immediately after the deposition of the samples and then after 7, 14, 21, and 28 days. For reference, the spectra of uncapped CuCl samples were studied along side the capped samples.

For the electrical measurements, the protective layers were sandwiched between indium tin oxide (ITO) and Aluminium electrodes, resulting in metal–insulator–metal (MIM) structures. In all situations parasitic effects were eliminated by the used of guard rings. Contacts were made to the electrodes by using an aluminium jumper wire of 0.025 mm diameter (Advent Research Materials Ltd) and quick drying silver paint (Agar Scientific). The samples were mounted in a light-tight, earthed, steel vacuum chamber, allowing electrical characterisation at a base pressure of 10^{-3} Torr. AC electrical characterisation was performed with a Hewlett Packard 4284A 20Hz – 1MHz precision LCR meter. Capacitance was measured as a function of frequency from 20 Hz to 1MHz. All measurements (optical & electrical) were carried out at room temperature.

6.3   Results

6.3.1   UV/Vis Spectra of the As Deposited CuCl Films

The absorption spectrum for the uncapped film taken immediately after deposition is shown in figure 6.1, plot (a). This shows clearly the Z_{12} and the Z_3 excitonic absorption features, which are as a result of the valence band being split into two bands by the spin orbit interactions [9].
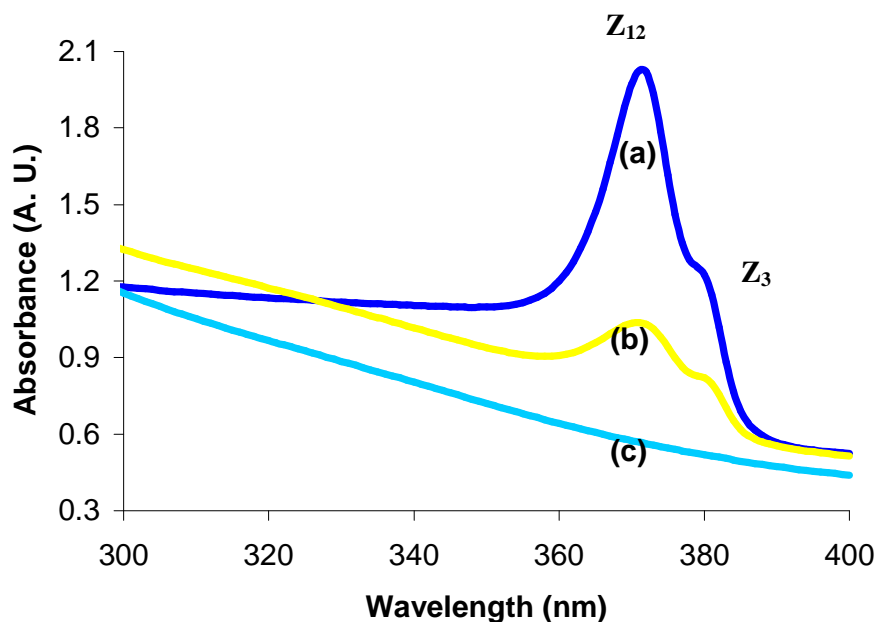
Figure 6.1: *Absorbance spectra of unprotected CuCl film: (a): Immediately after deposition, (b): After 7 days, (c): After 14 days.*

The degradation of the film is detected by the large reduction and broadening of the excitonic peaks as can be seen in figure 6.1, plots (b), and (c). After 14 days the excitonic peaks disappeared, indicating a total oxidation of the CuCl film. By examining the absorption spectra of figures 6.2, 6.3 and 6.4, one can still notice the effect of oxidation on the CuCl film capped with PECVD SiO_2 while those encapsulated with PSSQ and COC are stable in the ambient. We can conclude from the absorption measurements that the PECVD SiO_2 layer somewhat reduced the kinetics of the CuCl deterioration process while organic PSSQ and COC layers prevented it.
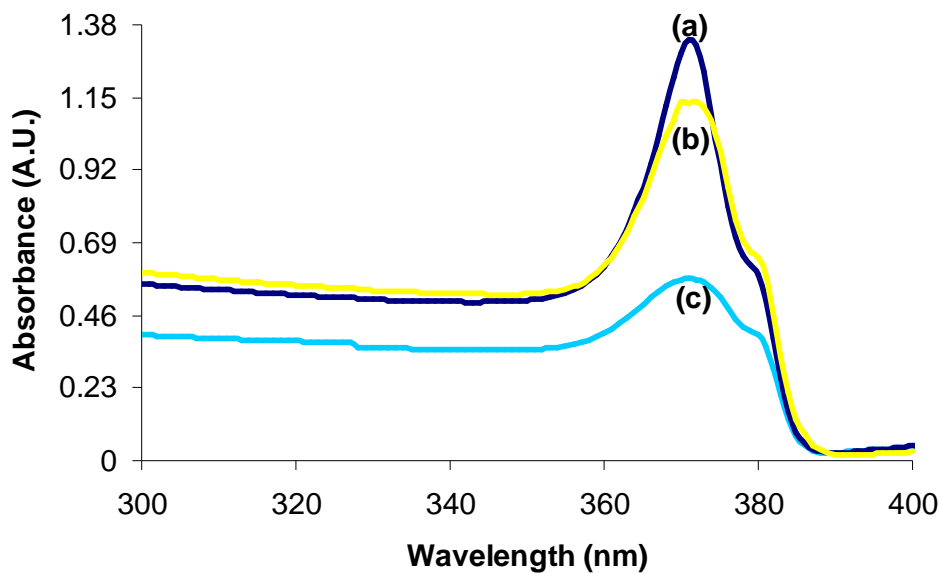
Figure 6.2: *Absorbance spectra of CuCl film protected with SiO₂; (a): Immediately*

after deposition, (b): After 7 days, (c): After 28 days in order to aid viewing.
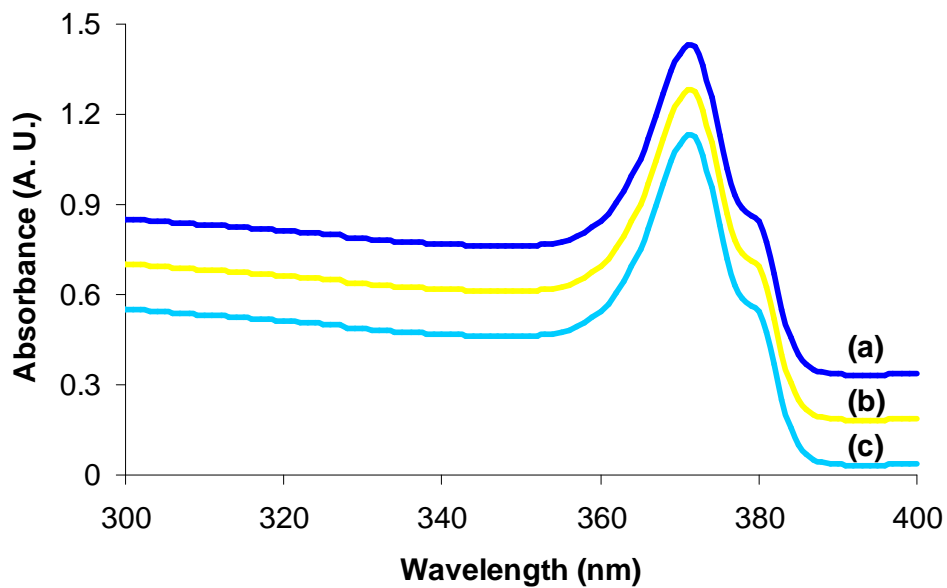

Figure 6.3: *Absorbance spectra of CuCl film protected with PSSQ; (a): Immediately*

after deposition, (b): After 7 days, (c): After 28 days. The plots (a) through (c) are

shifted with respect to each other.
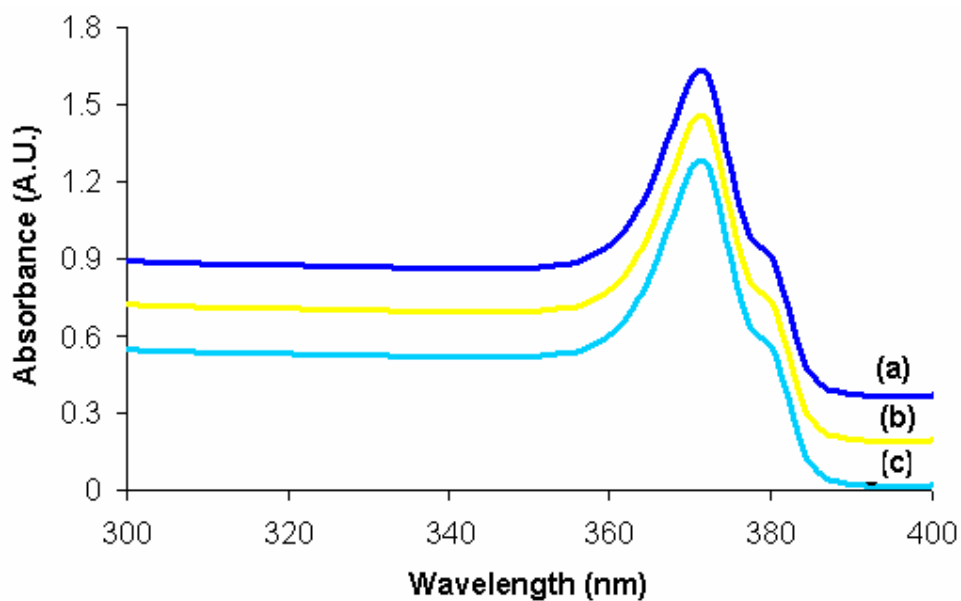
Figure 6.4: *Absorbance spectra of CuCl film protected with COC; (a): Immediately after deposition, (b): After 7 days, (c): After 28 days. The plots (a) through (c) are shifted with respect to each other.*

The structure and properties of PSSQ depends strongly on the thermal curing conditions [16]. In an ideal situation the PSSQ films should be cured at a temperature of ~ 350°C while the COC should be cured at 230°C for complete polymerisation of their network structures. However in our situation we could not reach these upper thermal limits because CuCl chemically reacts with Si at elevated temperatures [3].
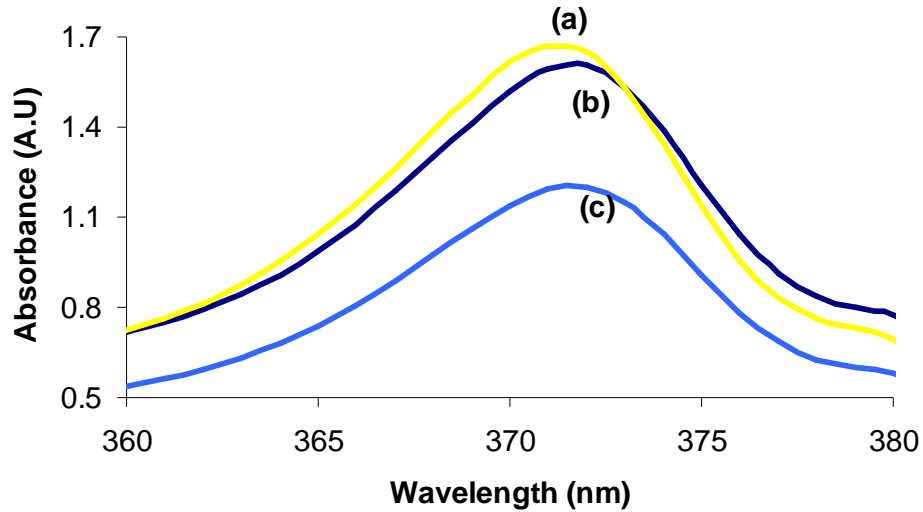
Figure 6.5: *Effect of thermal treatment on CuCl films in vacuum under N_2 ambient; (a): As deposited film (b): Film subjected to thermal treatment for 1 hour at 200˚C, (c): Film subjected to thermal treatment for 1 hour at 230˚C.*

Further to this, we have observed a slight red shift in the excitonic peak for the absorption spectra of CuCl films heated at 200˚C. For films heated above this temperature, we have also observed a reduction of the intensity of the excitonic peaks, coinciding with a degradation of the optical quality of CuCl films as a result of chemical reactions as explained by [3]. Typical UV/Vis spectra of the as deposited CuCl film, and CuCl films heated at 200 and 230˚C is depicted on figure 6.5. This clearly illustrates the effect of thermal treatment on the optical properties of CuCl films as explained. In a related development, very recently, Kondo [15] reported similar red shift and optical degradation in the photoluminescence and absorption spectra of heated CuCl films and suggested that the shift in the excitonic peaks is probably due to the relaxation of the exciton confinement effect.

## 6.3.2   IR Spectra of the As Deposited CuCl Films

Figure 6.6 shows the IR spectra of the uncapped CuCl. The heteroepitaxially grown CuCl/Si structure was used for the background scanning, thus the as deposited film gave a straight line spectrum. The major differences observed between the spectrum
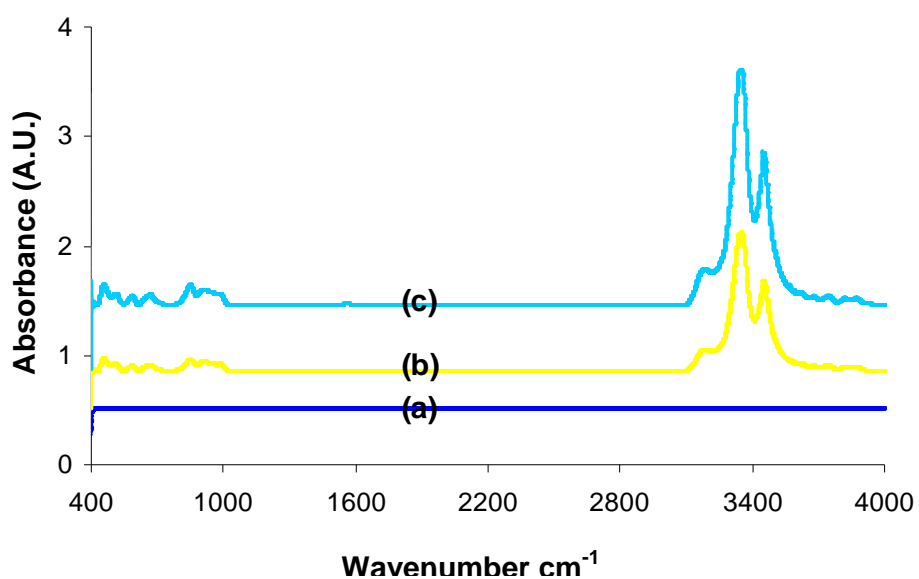
Figure 6.6: IR spectra of unprotected CuCl film; (a): Immediately after deposition, (b): After 7 days, (c): After 28 days. The plots (a) through (c) are shifted with respect to each other for clarity.

of the as deposited CuCl film and after 7 days of exposure to the ambient are the intense double peaks centred around ~ 3336 cm^{-1} and ~ 3444 cm^{-1}. This indicates the oxidation of CuCl to an oxyhalide of Cu II, which is as a result of CuCl reacting with moisture in ambient air [10]. The most likely reason behind the oxidation is due to the

weak bonds that exist in monovalent cuprous halide compounds. The oxidation increases as a function of time, which is consistent with the UV/Vis data. Similar to the uncapped film, oxidation does take place in films capped with SiO_2 deposited by PECVD as can be seen in figure 6.7.
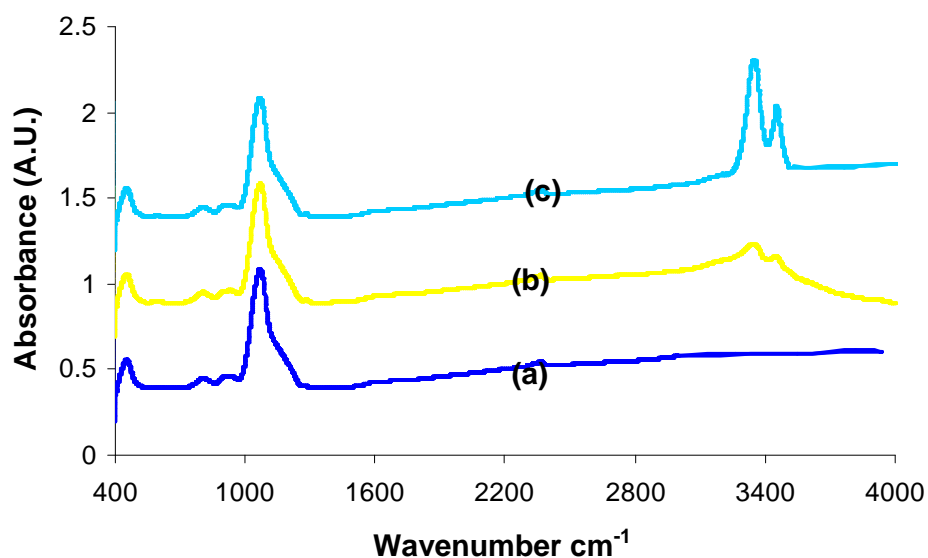
Figure 6.7: *IR spectra of CuCl film protected with SiO_2; (a): Immediately after deposition, (b): After 7 days, (c): After 28 days. The plots (a) through (c) are shifted with respect to each other in order to aid viewing.*

The only difference between the SiO_2 encapsulated films and the unprotected film is that the oxidation rate has been reduced in the SiO_2 protected films. Other major peaks in the SiO_2 spectra are related to Si–O–Si bonds occurring at 450 cm^{-1} and 1070 cm^{-1} [11]. Similar to the UV/Vis measurements, the IR results show no evidence of oxidation in the films capped by PSSQ and COC, which is confirmed by the absence

of the double peaks at ~ 3336 cm^{-1} and ~ 3444 cm^{-1} in figures 6.8 and 6.9. The major

absorption peaks in the PSSQ capping film spectra include Si–C at 608 cm^{-1} [12],

Si–O–Si occurring at ~1090 cm^{-1} [4] and the broad band around 3200 – 3600 cm^{-1} is

attributed to OH due to incomplete curing of the film. For COC, the several peaks

occurring between 950–1225 cm^{-1} and the double peaks centered around 2917 cm^{-1}

and 2847 cm^{-1} are attributed to C–H absorption, the peak at 1459 cm^{-1} is the C=C–C

aromatic stretch while the peak at 1729 cm^{-1} is due to the carbonyl C=O bond [13].
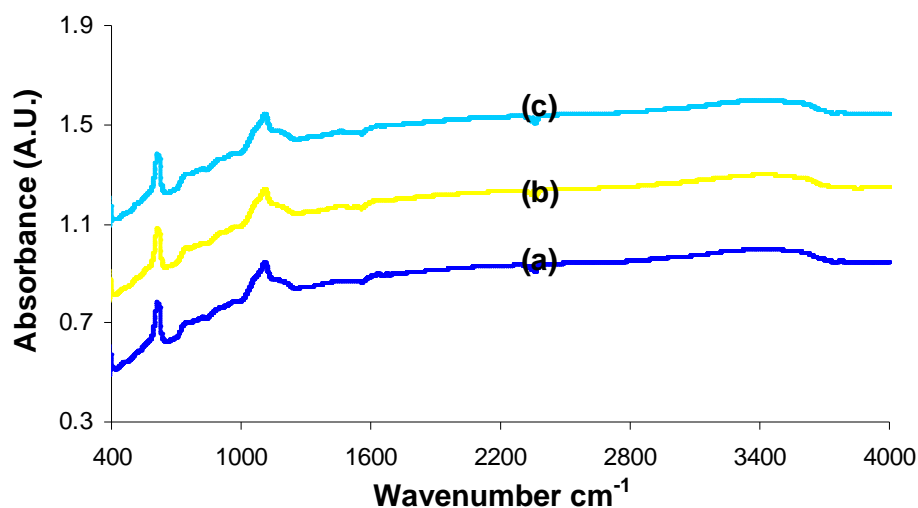
Figure 6.8: IR spectra of CuCl film protected with PSSQ; (a): Immediately after deposition, (b): After 7 days, (c): After 28 days. The plots (a) through (c) are shifted with respect to each other for clarity.

We have observed from our experimental results that the degradation process of

deposited CuCl films depends greatly on the purity of the source CuCl powder used

for the evaporation and also the cleanliness of the substrate. PSSQ and COC

encapsulated films deposited from high purity freshly prepared CuCl powder on to clean substrates have been found to be still chemically stable for a period of over a year.
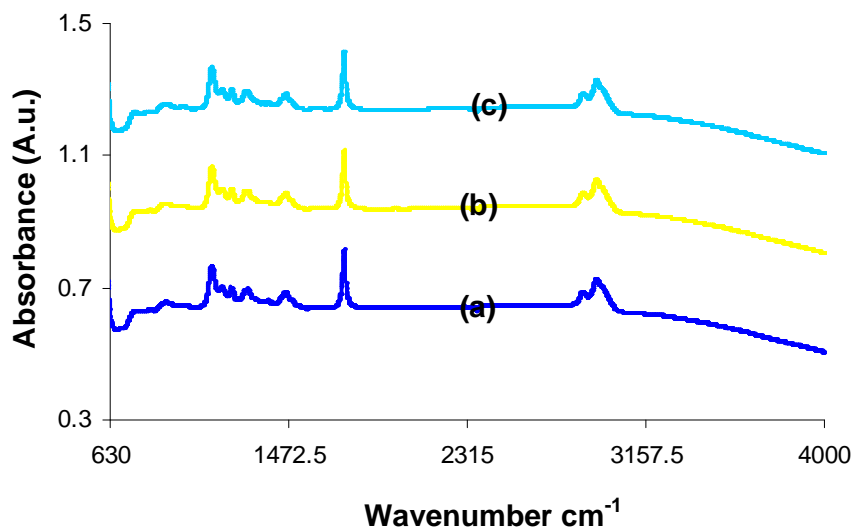

Figure 6.9: IR spectra of CuCl film protected with COC; (a): Immediately after deposition, (b): After 7 days, (c): After 28 days. The plots (a) through (c) are shifted with respect to each other for clarity.

6.3.3   UV/Vis and IR Spectra of the O_2 Plasma Immersed CuCl Films

Unlike the as deposited films, preliminary results showed that both PSSQ and COC encapsulants failed to prevent the oxidation of CuCl films. Figure 6.10 shows the UV/Vis spectra of the 1 minute oxygen plasma immersed CuCl film encapsulated with COC. By examining these spectra, one can observe the presence of oxidation by a reduction of the excitonic peak intensity (372 nm) even after a week. The reduction

in the excitonic peak intensities increases as a function of time in a similar way to the SiO$_2$ protected films of figure 6.2. A similar reduction of excitonic peak intensities as a function of time was observed for the UV/Vis spectra of the PSSQ encapsulated CuCl films.
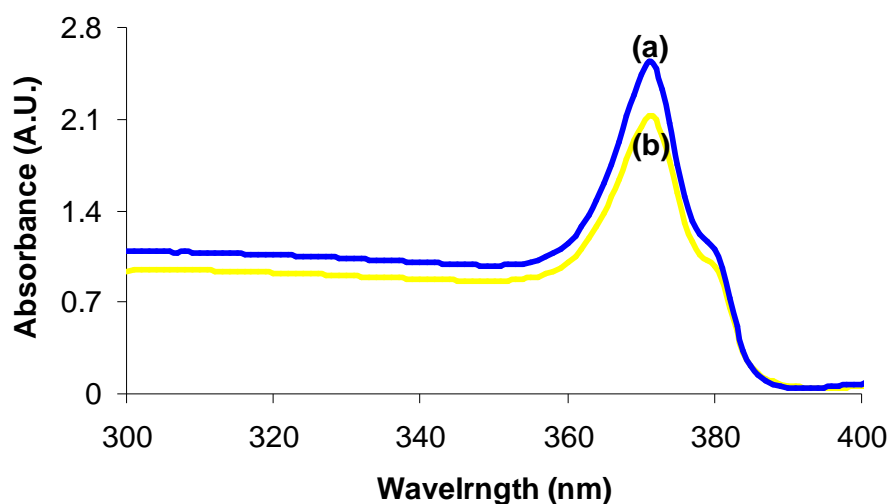
Figure 6.10: *Absorbance spectra of 1 minute O$_2$ plasma immersed CuCl film protected with COC; (a): Immediately after deposition, (b): After 7 days.*

The IR spectra of the encapsulated films also confirmed the presence of oxidation in the CuCl films protected with both PSSQ and COC. Figure 6.11 shows the spectra of the 1 minute oxygen plasma immersed CuCl film encapsulated with PSSQ. By examining these spectra, one can observe the presence of oxidation confirmed by the double peaks centred around ~ 3336 cm^{-1} and ~ 3444 cm^{-1} even after a week of exposure to ambient. The oxidation of the CuCl films increases as a function of time in a similar way to the unprotected film of figure 6.6. A similar oxidation process was observed for films encapsulated with COC.

The inability of both encapsulants (COC and PSSQ) to prevent the oxidation of the oxygen plasma immersed CuCl films may be ascribed to the incomplete polymerisation of both encapsulants due to lower curing temperature, since films were cured at room temperature in order to avoid the escape of oxygen from CuCl crystals.
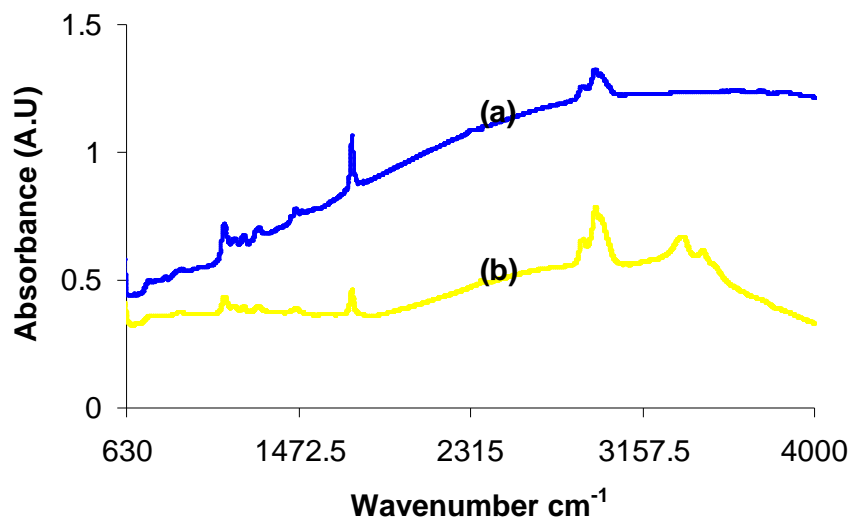
Figure 6.11: *IR spectra of O_2 plasma immersed CuCl film protected with COC; (a): Immediately after deposition, (b): After 7 days.*

We recall the results of the temperature dependency of the conductance of the O_2 plasma immersed films of section 5.4.4, where it was demonstrated that the electronic conductivity of the oxygen plasma immersed films decreases at sufficiently elevated temperature due to the outward diffusion of oxygen dopant that act as acceptors in the CuCl crystals. Thus it was anticipated that by not annealing the films we will reduce the likeliness of oxygen dopant escaping from the CuCl films.

However, both the unprotected as deposited samples and unprotected O_2 plasma immersed samples stored in a desiccator or under constant dynamic vacuum have been found to be free from oxidation for several weeks. This represents an area where more research will be undertaken in future.

6.3.4   Dielectric Constant

Figure 6.12 shows the capacitance as a function of frequency for the three metal–insulator–metal structures, with a bias of 0.5 V (AC) superimposed on 10 V (DC). Analysing the capacitances of the protective layers, we have observed that the COC based dielectric displayed an almost frequency independent capacitance. Similar to COC film, the PECVD SiO_2 film showed a fairly constant capacitance throughout the frequency range while the PSSQ layer showed a highly frequency dependent capacitance at low frequencies.

The electrical stability of the COC film may be attributed to the rigid olefin units randomly or alternatively attached to the polymer backbone [7], while the variation of the capacitance of the PSSQ film may be linked to incomplete polymerisation and interfacial capacitance effects. In an ideal situation, the PSSQ and the COC films should be cured at 350°C and 230°C respectively. However, we could not reach these upper temperature limits in order to avoid the degradation of the optical quality of the CuCl films as explained in section 6.3.1.
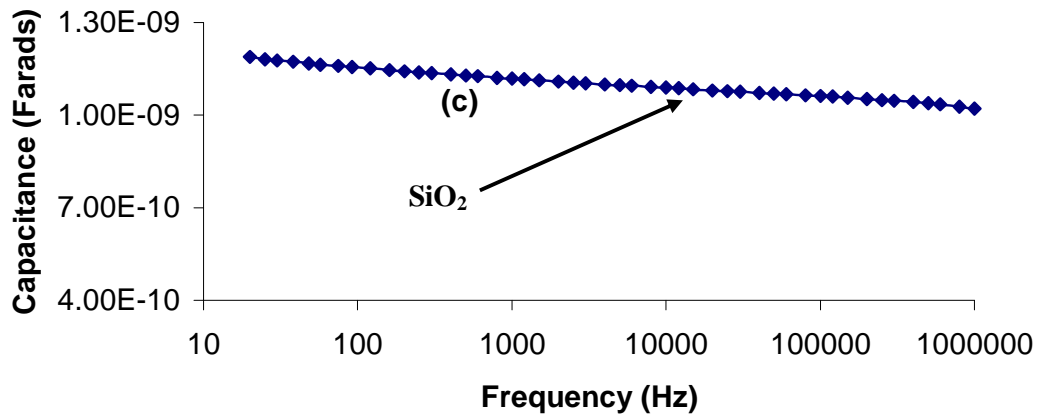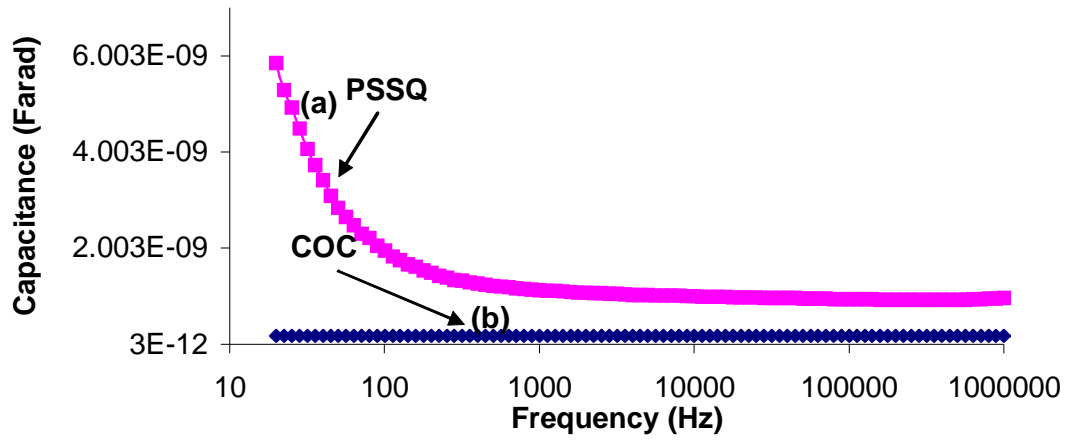
Fig. 4.3: *Capacitance – Frequency plot for the protective layers; (a): PSSQ film, (b): COC film and (c): SiO₂ film.*

The relative permittivities (dielectric constants) of the protective layers were determined from the capacitance – frequency plot at 1 MHz using the relation:

$$C = \varepsilon_0 \varepsilon_r \, A/d \qquad\qquad (6.1)$$

to be 2.3, 3.6 and 6.9 for COC, PECVD SiO_2 and PSSQ, respectively. In equation (6.1) ε_0 is the permittivity of free space, ε_r is the relative permittivity or dielectric constant, d is the thickness of the film and A is the active area of the film. The high value of the dielectric constant of the PSSQ may be linked to the presence of water (OH) in the insulator, whose dielectric constant is ~ 80 [14], due to incomplete polymerization of PSSQ as a result of curing at a lower temperature.

The ultimate goal of this research will be to fabricate an optoelectronic device from CuCl films. From the view of a laser diode, the dielectric constant of the cladding layers must be less than that of the active semiconductor material in order to achieve optical confinement. In our case, all three dielectrics have relative permittivities lower than that of CuCl ($\varepsilon_r = 10$) and therefore any of them will be suitable as the cladding layers for the CuCl based laser diode device. However, COC with the smallest dielectric constant should be the best candidate out of the three dielectrics studied.

6.4   Conclusion

In summary, thin film, luminescent, heteroepitaxial CuCl on Si oxidises into oxyhalides of Cu II on exposure to ambient air. This can be prevented by using protective layers that will insulate them against moisture and air:

- The UV/Vis and IR absorption measurements showed that both cyclo olefin copolymer (COC) and polysilsesquioxane (PSSQ) layers successfully encapsulated the as deposited CuCl films for lengthy periods of at least 28

days while PECVD deposited SiO_2 slowed the rate but did not eliminate the oxidation.

- Thin films of highly purified CuCl deposited on clean substrates and encapsulated with either COC or PSSQ have been found to be chemically stable for more than one year.

- Both COC and PSSQ based encapsulants failed to prevent the oxidation of O_2 immersed CuCl films, probably due to incomplete polymerisation of the network structures of the encapsulants.

- The high frequency dielectric constants of the protective layers were estimated at 1MHz to be 2.3, 3.6 and 6.9 for COC, SiO_2 and PSSQ, respectively.

References

[1]   M. Nakayama, H. Ichida, & H. Nishimura, *Journal of Physics: Condensed Matter* **11** (1999) 7653

[2]   H.G. Grahn, *Introduction to Semiconductor Physics*, World Scientific (1999)

[3]   L. O'Reilly, G. Natarajan, P. J. McNally, D. Cameron, O. F. Lucas, M. Martinez-Rosas, L. Bradley, & A. Reader, *Journal of Materials Science: Electronic Materials* **16** (2005) 415

[4]   S. Murarka, P. Eizenberg, M and A. Sinha, *Interlayer dielectrics for semiconductor technologies*, Academic Press (2003)

[5]   Wei-Chih Liu, Chang-Chung Yang, Wen-Chang Chen, Bao-Tong Dai and Ming-Shih Tsai, *Journal of Non-Crystalline Solids,* **311** (2002) 233

[6]   Ju Young Shin, Ji Young Park, C. Liu, J. He and S. Kim, *Pure and Applied Chemistry,* **77**:5 (2005) 801

[7]   G. Khanarian, *Optical Engineering,* **40** (2001) 1024

[8]   W. Kaminsky, A. Bark, M. Arndt, *Macromol. Chem. Macromol. Symposium* **47** (1991) 83

[9]   M. Cardona, *Physical Review* **129** (1963) 6

[10]   C. Schwab and A. Goltzene, *Progress in Crystal Growth and Characterisation* **5** (1982) 233

[11]   K. Aumaille, C. Vallee, A. Grainer, A, Goullet, F. Gaboriau, & G. Turban, *Thin Solid Films* **359** (2000) 188

[12] Y. Zhou, D. Probbst, A. Thissen, E. Kroke, R. Riedel, R. Hauser. H. Hoche, E. Broziet, P. Kroll, H. Stafast, *Journal of the European Ceramic Society* **26** (2006) 1325

[13] J. Coates, *Interpretation of Infrared Spectra: A practical approach, Encyclopedia of Analytical Chemistry,* R. A Meyers (Ed.), (2000) 10815

[14] J.M. Albella- Martin, and J. M Martinez-Duart., *Fisica de Dielectricos, Aplicacion a los materials y Didpositivos,* Bioxareu Editores (1984)

[15] S. Kondo, Y. Hata and T. Saito, *"Extremely-high-intensity photoluminescence from CuBr films fabricated by film-substrate chemical reaction of CuCl on KBr-crystal substrate",* Accepted by *Materials Letters* 19 April 2007

7

Conclusions and Further work

7.1 Conclusions

CuCl is a direct wide bandgap material with attractive properties for optoelectronic applications. The aim of the research described herein was to deposit, encapsulate and evaluate γ–CuCl films for their microstructural, electronic and optoelectronic properties. Thin films of CuCl (100 – 500 nm) were successfully deposited on amorphous glass, ITO coated glass and single crystal silicon substrates using vacuum evaporation. Some of the CuCl samples were oxygen plasma treated for 1, 2 and 3 minutes to improve the electronic conductivity via p-type doping.

X-ray diffraction (XRD) measurements confirmed that the as deposited and oxygen immersed films were zincblende in structure and preferentially oriented in the (111) direction irrespective of the underlying substrates. The microstructural properties (grain size and AFM root mean square roughness) of the as deposited films were almost the same irrespective of the underlying substrate. On the other hand the microstructural properties of the oxygen plasma immersed films vary as a function of plasma treatment duration.

The room temperature absorption spectra reveal the Z_{12} and the Z_3 free excitonic absorption features, occurring at 3.34 eV and 3.27, eV respectively, for both untreated and plasma treated films deposited on glass and ITO substrates. At 10 K, the PL spectrum of the CuCl/Si structure using 244 nm excitation reveals the Z_3 free exciton occurring at 3.203 ± 0.003 eV, the I_1 impurity bound exciton located at 3.181 ± 0.003 eV, the M free biexciton occurring at 3.160 ± 0.003 eV and N_1 impurity bound to bi-exciton located at 3.135 ± 0.003 eV. However, the 20 K PL spectra for the three structures using a 325 nm excitation revealed only the Z_3 free exciton, the I_1 impurity bound exciton and the N_1 impurity bound biexciton occurring at 3.204 eV, 3.18 eV and 3.152 eV respectively, for all three structures. The room temperature PL spectrum of the films was dominated by the Z_3 free exciton. The bandgap displayed a temperature dependence increasing by $\sim$ 37 meV from 10 K to room temperature. This anomalous effect is believed to be related to electron-phonon renormalization of the electronic structure of CuCl band gap as the temperature increases.

At 10 K the 1 minute and 2 minute O_2 plasma treated samples reveal both the Z_3 free exciton and the I_1 impurity bound exciton, while the 3 minute O_2 treated samples only reveal the Z_3 free exciton. In addition to this, a broad band ascribed to an oxygen related emission process is observed at $\sim$ 3 eV between 10 and 140 K for all the plasma immersed films. Thereafter up to room temperatures the PL spectra of all samples were dominated by the Z_3 free exciton. The temperature dependency of the band gap for all the oxygen plasma immersed films was found to follow the same anomalous temperature dependence as for the untreated films; however the oxygen plasma treated films were less sensitive to temperature. The optical properties of the oxygen plasma immersed samples were found to differ from the as deposited film as

the plasma duration increases with respect to the number of exciton peaks and the broad band observed at low temperatures.

The electrical properties of the CuCl films was found to depend strongly on the nature of the electrodes used. An exponential I-V characteristic was observed for the as deposited CuCl films using irreversible electrodes (Au/CuCl/Au), which was interpreted to be a characteristic of p-type mixed ionic – electronic material. The Ohmic behaviour and a lower current density observed for samples confined between reversible electrodes (Cu/CuCl/Cu) is consistent with the theory of a defect chemistry effect for a mixed ionic – electronic material equilibrated with its parental electrode. The exact value of the electrical conductivity was found to vary from sample to sample due to the inability of the vacuum evaporation to repeatedly and precisely deposit films of the same stochiometry. An average hole conductivity of $\sim 2.3 \times 10^{-7}$ S/cm was deduced to be in coexistence with Cu^+ ionic conductivity using Au electrodes while a total conductivity of 6.5×10^{-7} S/cm was calculated using Cu electrodes.

An analysis of the Arrhenius plot for the as deposited films confirmed that CuCl films are of the mixed ionic – electronic type with predominantly extrinsic Cu^+ cationic conduction by a vacancy mechanism at temperatures above ~ 270 K and predominantly electronic hole conduction dominant at temperatures below ~ 265 K, where the thermal activation energy is believed to be insufficient to sustain substantial ionic motion.

Unlike the as deposited films, room temperature DC characteristics of the oxygen immersed films using Au electrodes all gave an Ohmic response with conductivities as high as 100 times those of the untreated films. The large increase in the conductivity is ascribed to O_2 introducing acceptor states in CuCl films.

The Arrhenius plot of the oxygen plasma immersed CuCl films was found to be dominated mainly by a hole conduction mechanism up to temperatures above room temperature, at which point oxygen starts escaping from the CuCl crystals. Preliminary SIMS measurements revealed that the oxygen penetration was as deep as 300 nm for films plasma immersed for a duration of 3 minutes. Cathodic decomposition via an electrolytic conduction mechanism has been observed in both the as deposited and plasma immersed CuCl films when a voltage of more than 5 V was applied.

Thin luminescent, as deposited and oxygen immersed CuCl films have been observed to oxidise into oxyhalides of Cu II on exposure to ambient. The oxidation process can be prevented for the as deposited films using protective layers that will insulate them against moisture and air. UV/Vis and IR absorption measurements showed that both organic cyclo olefin copolymer (COC) and polysilsesquioxane (PSSQ) layers successfully encapsulated CuCl for lengthy periods greater than 28 days. Further to this, the deterioration of CuCl films was found to depend strongly on the purity of the source CuCl powder and the cleanliness of the substrates used for the deposition. Thin films of highly purified CuCl deposited on to clean substrates and encapsulated with either COC or PSSQ have been found to be chemically stable for more than one year.

On the other hand, both COC and PSSQ based encapsulants failed to prevent the oxidation of O_2 immersed CuCl films, probably due to incomplete polymerisation of the network structures of the encapsulants, since the films were cured at room temperature. The high frequency dielectric constants of the protective layers were estimated at 1MHz to be 2.3, 3.6 and 6.9 for COC, SiO_2 and PSSQ, respectively. The relative permittivities of the three dielectrics are smaller than the relative permittivity of CuCl, which indicates that any of them could be used as the cladding layer to fabricate a CuCl ($\varepsilon_r = 10$) based laser diode device.

7.2 Further Work

Following from the studies reported here, several lines of research suggest themselves. The following are pointers to further work that would extend the findings of the present investigations:

- Electrical properties: Further work on the depth of penetration of oxygen atoms using plasma immersion will be required since the results reported here are only preliminary. Also additional electrical characterization of the as deposited and the oxygen plasma immersed films, including carrier concentration and carrier mobility using Hall effect measurements and Mott-Schottky analysis will be required to produce a better insight into the electrical properties of CuCl films.

- Encapsulation: One will need to fully encapsulate the oxygen immersed films in order have a practical use of this material. Owing to the thermal processing constraints for this material, there will be a need to protect the oxygen immersed films using a low temperature deposition dielectric. It will be

interesting to test the effectiveness of silicon nitride, a well known moisture barrier dielectric in the semiconductor industry, which can easily be deposited at low temperatures, e.g. using R.F sputtering techniques, on the oxygen plasma immersed CuCl films. In principle one could use the same plasma system for the O_2 treatment and silicon nitride capping.

- <u>Growth technique</u>: The vacuum evaporation method was used extensively in the deposition of the CuCl films studied herein. One of the main disadvantages of this technique in depositing compound materials is the inability to deposit films with the same stoichometry repeatedly. In fact we suspect that this is the main reason why the electrical properties of the CuCl films varied from sample to sample. Therefore it will be important to use more advance techniques like liquid phase epitaxy (LPE), molecular beam epitaxy (MBE) or atomic layer deposition (ALD), which are well known for depositing compound semiconductor materials with repeatable stoichometry. A further advantage of these methods is that dopants could easily be introduced during deposition, resulting in a better uniformity of dopants across the films.

- <u>Device fabrication</u>: It will be interesting to fabricate an excitonic based light emitting device from CuCl. This may begin by fabricating an excitonic based electroluminescent device from CuCl, based on the growth of adjacent n- and p-layers of CuCl sandwiched between appropriate electrodes. A useful start in this direction has been reported by our research team [A. Mitra, F.O. Lucas, L. O'Reilly P.J. McNally, S. Daniels and G. Natarajan, *J. Mater. Sci.: Mater. Electron, DOI* 10.1007/s10854-007-9178-8 (2007)].